INTERNATIONAL SCHOOL FOR ADVANCED STUDIES

CONDENSED MATTER THEORY SECTOR

Toward Realistic DFT Description of Complex Systems: Ethylene Epoxidation on Ag-Cu Alloys and RPA Correlation in van der Waals Molecules

Thesis submmitted for the degree of Doctor Philosophiæ
Academic Year 2011/2012

CANDIDATE
Ngoc Linh Nguyen

SUPERVISOR
Prof. Stefano de Gironcoli
Dr. Simone Piccinin

March 2012

SISSA - Via Bonomea 265, 34136 Trieste - ITALY

Contents

Introduction

Catalysis, the acceleration of reaction rate (activity) and/or the enhancement of product selectivity in a chemical reaction due to the participation of a substance called a catalyst, is one of the fundamental subjects in modern chemistry. Catalysis plays an important role in many aspects of daily life. Today, more than 90% of the chemical products produced in industry are facilitated by catalysts, providing to human life a wide range of applications such as fuels, plastics, drugs, fertilizers, etc. [1]. Catalysts have many different forms, varying from molecules to large structures such as zeolites or enzymes. Preparing the catalyst in the optimal form and studying its precise composition and shape are an important topic. In addition, catalysts may be used in various environments: in liquids, gases or at the surface of solids. Catalysis is therefore usually classified into three sub-disciplines: (i) homogeneous catalysis where both the catalyst and the reactants are in the same phase, (ii) biocatalysis where an enzyme considered as a large protein catalyzes biological reactions, and (iii) heterogeneous catalysis where the reactions of molecules in gas or solution are catalyzed by solid catalysts [1]. In particular, in this thesis, we will study one of the most important heterogeneous catalytic reactions, ethylene epoxidation, creating ethylene oxide (EO). This reaction has attracted considerable interest due to the variety of applications of EO product in chemical industry, such as synthesis of ethylene glycol, polyester fabrics, surfactants and detergents [2].

The use of heterogeneous catalysts in industrial production has been realized for several decades. In the early days of catalysis history, the applications were mostly concentrated on improvement of the activity of catalysts and the efficiency of the production processes using catalysts. This was done by employing trial-and-error techniques, without an understanding of catalytic mechanisms at the microscopic level [1]. Later, the accumulated information from experiments, including studies about using promoters as alkali metals, halides,.., did help to improve activity, selectivity, and enhanced the stability of catalysts. Fundamental understanding of catalysis starts to grow considerably with the introduction of spectroscopy, first with infrared spectroscopy in the 1950's and followed by a range of surface science techniques such as X-ray photoelectron spectroscopy (XPS), low-energy electron diffraction (LEED), high resolution electron energy loss spectroscopy (HREELS), transmission electron microscopy (TEM), and by the late 20^{th} century, scanning tunneling microscopy (STM) [3]. These sophisticated techniques allow for catalyst characterization, including structure and composition, as well as for the identification of intermediate species and adsorbed molecule structures on the catalyst surfaces. However, they are usually carried out in ultra high vacuum (UHV) conditions, and the knowledge thus obtained has been applied to "real life" catalytic processes that often take place at high temperature and high pressure. In some cases, this approach has been extremely useful [4], while the pressure gap between surface science experiments and realistic applications inhibits, in several cases, a direct transfer: this is because the

structure and composition of the surface can drastically change when going from UHV to realistic conditions, a problem known as material gap [5, 6]. Recently, new surface science techniques, including high-pressure STM, environmental scanning/transmission electron microscopy (SEM/TEM), ambient-pressure photoelectron spectroscopy, and in situ scanning transmission x-ray microscopy, have been developed further, allowing to probe the catalyzed reactions under realistic high-pressure and -temperature conditions [7]. This development rapidly closes the gaps between surface science and real catalysis studies. Simultaneously, these techniques also establish a relationship between surface structure and composition of materials during operation, and the chemical properties needed to enable the design of new and better catalysts.

On the other hand, the study of structural properties and of processes on the surfaces frequently depends on understanding phenomena which originate at the atomic level. In such cases, an accurate description of interactions between large numbers of atoms is critical and in turn needs an accurate description of the electronic properties, which play a crucial role in the bonding of atoms into molecules or surfaces. Equations for the interactions are too complicated to be solved exactly; however their solutions can be addressed by computational techniques. The most accurate and also most computationally demanding are *ab initio* methods which do not use any empirical adjustable parameters. Amongst them, the Density Functional Theory (DFT) approach for quantum mechanical problems stands out as an excellent compromise between accuracy and computational efficiency. DFT provides a framework to evaluate the ground state electron density and total energy through solutions of single-electron Schrödinger-like equations (Kohn-Sham orbitals), and an approximation for the so-called exchange-correlation energy [8, 9]. Finding the accurate formalism for this energy is understood as one of the most difficult tasks, and can limit the applicability of DFT in certain classes of materials. For a couple of decades, while many different forms of exchange-correlation functional have been proposed, the Local Density Approximation (LDA) and Generalized Gradient Approximation (GGA) have been widely used in many studies. In particular, these approximations have shown to be remarkably successful in describing heterogeneous catalysis systems. The local LDA and semi-local GGA density functionals can give accurate description for strong covalent or metallic bonds that are the most important ones on the catalyst surfaces, including the interactions between metal atoms or chemisorption of adsorbates at the surfaces. Currently, DFT studies are widely used to generate and rationalize various kinds of observables characterizing complicated systems of importance for heterogeneous catalysis. These data successfully complement the experimental results and some of them would otherwise be very difficult (or even impossible) to obtain or hard to interpret. Therefore, the extraordinary progress in DFT calculations for surface processes is a key development that has created the possibility of computer-based catalyst design [10].

Besides the successful description of chemisorption, DFT usually gives a poor description of physisorption bonds compared to experiments. Indeed, DFT calculations with LDA and GGA functional are poor or even wrong in estimating the

non-local correlation effects that are involved in the long-range dispersion interactions, also known as van der Waals (vdW) interactions [11]. In nature, vdW interaction plays a major role in defining the structure, stability, and function for a wide variety of molecules and materials. An accurate *ab initio* evaluation of vdW interactions is an extremely difficult task, since the vdW dispersion energy originates from the non-local correlated fluctuation of electrons and, in principle, must be computed by many-body quantum mechanics [11]. While accurate calculations using quantum chemistry methods are not efficient for big systems, finding a new method to improve the ability in evaluating vdW interaction is one of the challenges for DFT, and this has been attempted for many years.

One of the simplest ways to include this interaction is to add an empirical pairwise correction, with form of dispersion function C_6/R^6, into the exchange and correlation functional. This empirical dispersion correction is quite popular and reasonably successful for intermolecular interactions, but is not consistent in DFT calculation since there is no unique way to compute the C_6 coefficients for different atoms [12]. Recently, DFT calculations of weakly bonded systems have seen a renewed interest in using the adiabatic connection fluctuation-dissipation theorem (ACFDT), proposed in the 1970's by Langreth *et al.* [13], to compute the exchange-correlation energy. Beyond standard DFT, in ACFDT the exchange energy is treated at the exact-exchange (EXX) level given by the Hatree Fock (HF) expression for the exchange energy but evaluated with Kohn-Sham orbitals. The correlation energy, on the other hand, is expressed in an exact formula through a relation between the dynamic response functions of fully interacting and non-interacting systems. In practice, the evaluation of the correlation energy will be performed based on the framework of perturbation theory, and usually the calculation is simplified by the Random Phase Approximation (RPA) for the exchange-correlation kernel. There are several DFT-implementations for the calculation of the total energy within the EXX and RPA-correlation formalism that is denoted as EXX/RPA-correlation energy. In particular, recently an efficient implementation for the evaluation of RPA-correlation using a plane wave basis set representation and the pseudopotential method has been developed. Such approach has greatly improved the computational speed and memory consumption compared to the existing implementations, by exploiting iterative algorithms to diagonalize the RPA dielectric matrices [14]. Unfortunately, since the EXX/RPA-correlation energy is only calculated in a post-DFT procedure (one-shot) with the KS orbitals taken from DFT within LDA or GGA functional, it has been found, for several systems, that EXX/RPA correlation energies may significantly depend on the choice of input single particle wavefunctions [15, 16]. In this work, we derive an approach allowing to perform a self-consistent field (scf) procedure that can minimize EXX/RPA energy with respect to the one-shot calculations. The local EXX/RPA-scf potential will be estimated in each iterative scf step, using Optimize Effective Potential (OEP) method [17] combined with Density Functional Perturbation theory [18].

The accurate calculations of the vdW interaction in heterogeneous catalysis with EXX/RPA have been addressed recently in many aspects of physisorption of simple

molecules on the catalyst surfaces [19, 20]. The calculations, however, were performed without the scf procedure. Although, in this thesis, EXX/RPA and its scf schemes are employed to study only simple molecules, the results show that implementing the scf procedure of EXX/RPA-correlation energy is very important, and thus our work opens a promising approach for treating fully the long-range interactions between reactants and surfaces. This allows us to look forward in this direction for future developments.

In light of the above circumstances, the thesis is devoted to two different aspects, one is an application of DFT in heterogeneous catalysis study, and the second aspect is the theoretical development of self-consistent potential in the ACFDT method. It is organized as follows:

In Chapter 1, we will review the basic concept of electronic structure theory with the emphasis on DFT implemented in the Plane-Wave Pseudopotential approach. In particular, a brief review of the history of the development of exchange-correlation functionals in DFT will be introduced.

In Chapter 2, by means of DFT calculations, we will study the role of heterogeneous catalysts, such as silver-copper alloys, in the ethylene epoxidation reaction to improve the selectivity toward formation of the desired product EO. The catalyst models will be considered as the thermodynamically stable structures under the temperature and pressure conditions relevant for experiments.

Chapter 3 will be devoted for the calculations of EXX/RPA-correlation energy within ACFDT. It starts with the general introduction of ACFDT formalisms, and the new approach of RPA calculations based on the framework of dielectric matrix and iterative methods for its diagonalization. We will derive a new method to deal with the scf procedure for minimizing the KS energy in this case. At the end, some examples will be presented to validate the implementation.

Chapter 1

Ab-initio Electronic Structure Calculation

1.1 Schrödinger Wave Equation and Born-Oppenheimer Approximation

The nature of the matter of our everyday experience such as atoms, molecules, condensed matter, and man-made structures is determined by the fundamental particles, electrons and nuclei, whose understanding is based upon the theoretical methods of quantum mechanics and statistical mechanics. The non-relativistic Hamiltonian $\hat{H}$ for a system consisting of N_e electrons and N_I nuclei can be written formally in the following general form:

$$\begin{aligned} H = &- \sum_{I=1,N_I} \frac{\hbar^2}{2M_I} \nabla^2_{R_I} - \sum_{i=1,N_e} \frac{\hbar^2}{2m_e} \nabla^2_{r_i} \\ &+ \frac{1}{2} \sum_{i \neq j} \frac{e^2}{|r_i - r_j|} - \sum_{i,I} \frac{Z_I e^2}{|r_i - R_I|} + \frac{1}{2} \sum_{I \neq J} \frac{Z_I Z_J e^2}{|R_I - R_J|}, \end{aligned} \tag{1.1}$$

where, the coordinates of nuclei are R_I and the ones of electrons are r_i. Following a widespread notation, we use upper-case indexes I, J for nuclei, while lower-case indexes i, j are reserved for electrons. Furthermore, M_I and $Z_I e$ are the mass and charge of the I^{th} nucleus, while the electronic mass and charge are m_e and $-e$, respectively. Therefore, all components in the Hamiltonian are perfectly known, and in principle, all properties of the system can be derived by solving the many-body Schrödinger equation:

$$\hat{H}\Psi(r_i, R_I) = E\Psi(r_i, R_I). \tag{1.2}$$

In practice, this problem is almost impossible to treat in a full quantum mechanical framework. Firstly, there are too many degrees of freedom in the system, which complicates wave function representation, and results in a mathematically unsolvable Shrödinger equation. Secondly, the complete wave function, $\Psi(r_i, R_I)$, can not be easily factorized due to the correlation in dynamics and energetics between nuclei and electrons.

To partially overcome this problem, the usual choice is to resort to the so-called adiabatic approximation, introduced by Born and Oppenheimer in 1927, indispensable in quantum chemistry. The general idea of this method is the factorization of the full wave function $\Psi(r, R)$ into a nuclear and an electronic one, based on the fact that

the mass of electrons and those of ions are sufficiently different, $m_{\text{nuclei}}/m_e \geq 1836$. Therefore, in this spirit, the electrons can be adequately described as following instantaneously the motion of the nuclei, while their dynamics is characterized by the dynamically screened interaction potential. The total wave function in Eq.(1.2) can be separated into the product of a nuclear part, $\Phi(R_I)$, and an electronic part, $\psi(r_i; R_I)$, as:

$$\Psi(r_i, R_I) = \Phi(R_I)\psi(r_i, R_I), \tag{1.3}$$

and the Hamiltonian in Eq.(1.1) can be rewritten as two coupled problems for electrons and nuclei, respectively, as

$$[-\sum_{i=1,N_e} \frac{\hbar^2}{2m_e}\nabla^2_{r_i} + \frac{1}{2}\sum_{i\neq j}\frac{e^2}{|r_i - r_j|} - \sum_{i,I}\frac{Z_I e^2}{|r_i - R_I|} + V_{II}]\psi(r_i, R_I) = E(\{R_I\})\psi(r_i, R_I), \tag{1.4}$$

and

$$[-\sum_{I=1,N_I}\frac{\hbar^2}{2M_I}\nabla^2_{R_I} + E(\{R_I\})]\Phi(\{R_I\}) = \Sigma\Phi(R_I). \tag{1.5}$$

Where, V_{II}, in the former equation, is the potential of direct ion-ion interaction. One can see that in the problem for electrons, the effect of fixed nuclei on the electron's properties is determined through the local ionic potential $V_I(r) = \sum_I \frac{Z_I}{|r-R_I|}$ in the electronic Hamiltonian, while the electronic effects on the nuclear motion are included in the definition of the interaction potential in the nuclear Hamiltionian. Furthermore the solution of the nuclear quantum equation in Eq.(1.5) in a large variety of cases of interest can be simplified and the system can be treated classically by employing the well known Newton's equations:

$$M_I\frac{d^2R_I}{dt^2} = -\frac{\partial E}{\partial R_I}. \tag{1.6}$$

According to Born-Oppenheimer approximations, the many-body problem is made simpler, the problem of Eq.(1.2) is replaced by the problem of finding the proper way for treating the Schrödinger equations of electrons, Eq.(1.4), at fixed nuclear position.

1.2 Density Functional Theory

1.2.1 Hohenberg-Kohn theorems

Solving the Schrödinger equation to find the electronic ground state wavefunction in Eq.(1.4) for the many-electrons is still an unsolvable mathematical problem in general because of its dependence on $3N_e$ degrees of freedom which double if we also consider the spin: when the interaction between electrons is turned on, the complexity of the problem increases exponentially with respect to the number of electrons. Therefore, even considering a system at the nano-scale, a fully known solution is still out of reach. One needs again to introduce suitable approximations for the given problem.

Since early in 1928, many simple approximations in quantum many-body theory such as the free electron or Hartree-Fock approximations have been widely used to deal with the electronic problem in physics and chemistry. Later higher accuracy methods, based on post-Hartree-Fock theories such as Møller-Plesset approach or configuration interaction (CI), have been investigated and developed in quantum chemistry. However, these approaches become very rapidly computationally very demanding. In 1964, Hohenberg and Kohn proposed and proved a theorem that allows to search for the ground state energy of a many-body electron system as a functional of its ground-state electron density, introducing the so-called Density Functional Theory (DFT). Employing DFT approach to the electronic problem is, in principle, simpler than the methods mentioned above since it can reduce the number of degrees of freedom from $3N_e$ to only 3 coordinate variables [8]. This theory is built upon two main theorems:

(i) An interacting particle system, that is characterized by a given external potential $v_{\text{ext}}(r)$, has a ground state particle density $n_0(r)$, and this density determines uniquely that external potential up to an additive constant. The proof of the first theorem was given for the first time by Hohenberg and Kohn in the original DFT publication [8], and was later generalized in a constrained-search formulation by Levy [21, 22]. It shows that the knowledge of the ground state density $n_0(r)$ determines completely all the ground-state properties of a system.

(ii) The energy can be defined as a functional of the density $n(r)$ for any given external potential v_{ext}. This energy functional satisfies a variational principle so that the global minimum of energy is the exact ground-state energy of the system and the density in this case is the ground-state density $n_0(r)$. This theorem allows to define the total energy of a system in its ground-state as follows

$$E_{\text{GS}} = \min_n\{F[n] + \int dr^3 v_{\text{ext}}(r)n(r)\} + E_{II}, \tag{1.7}$$

where $F[n] = T[n]+E_{\text{int}}[n]$ is a universal functional that is defined by the summation of $T[n]$ and $E_{\text{int}}[n]$ that are the kinetic energy functional and the electron-electron interaction energy at the given $n(r)$, respectively. The last term in Eq.(1.7), E_{II}, is the direct ion-ion interaction, which is treated classically.

1.2.2 Kohn-Sham Equations

In practice, it is not straightforward to solve the full many-body Schrödinger equation within the Hohenberg-Kohn formalism because this approach gives no information about how to construct the functionals, $E_{\text{int}}[n]$ and $T[n]$, in the universal functional $F[n]$ for an interacting system. The electron-electron interaction, $E_{\text{int}}[n]$, in principle, can be separated into the electrostatic (Hartree energy), $E_{\text{H}}[n]$, and exchange and correlation contributions, $E_{\text{xc}}[n]$. Among the three functionals, with the exception of the classical electrostatic energy, $E_{\text{H}}[n]$, the expression for $T[n]$ and $E_{\text{xc}}[n]$ are usually defined by some appropriate approximations. The two simplest approximations that have been widely used even before HK theorem are the Hartree and Thomas-Fermi approaches. While in the first one, the $E_{\text{xc}}[n]$ is neglected, the latter represents $T[n]$ in terms of a density functional. These approaches, however, are much too simple, and they usually give inaccurate results compared to the real problems.

In 1965, Kohn and Sham (KS) proposed the idea of replacing the kinetic energy of the interacting electrons with that of an equivalent non-interacting system which is practically solvable [9]. In particular, KS approach assumes that the ground-state density of the interacting system is equal to that of an auxiliary non-interacting system and that the kinetic energy of the system is approximated by the kinetic energy of the non-interacting one, while all the difficult many body terms of $T[n]$ are incorporated into the last exchange-correlation energy term, $E_{\text{xc}}[n]$.

Comparing to H-K theorems, the expression of the total energy that enters in Eq.(1.7) is evaluated, according to KS approach, by the universal functional $F[n]$:

$$F[n] = T_{\text{KS}}[n] + \frac{e^2}{2}\int \frac{n(r)n(r')}{|r-r'|}drdr' + E_{\text{xc}}[n]. \tag{1.8}$$

Where, $T_{\text{KS}}[n]$ denotes the kinetic energy of the non-interacting system, that is a functional of the ground state density $n(r)$. The second term is the well known expression for the Hartree energy in term of the Hartree potential and density,

$$E_{\text{H}}[n(r)] = \frac{1}{2}\int dr v_{\text{H}}(r)n(r) = \frac{e^2}{2}\int \frac{n(r)n(r')}{|r-r'|}drdr'. \tag{1.9}$$

The last term, $E_{\text{xc}}[n]$, is the exchange-correlation energy, whose expression is not known exactly but must be approximated.

According to the second H-K theorem, for a given external potential v_{ext}, the total energy is variational with respect to the density $n(r)$. Therefore, one can minimize the total energy given in Eq.(1.7) by employing the Euler-Lagrange equations

$$\delta E = \int \delta n\{\frac{\delta T_{\text{KS}}[n]}{\delta n} + v_{\text{ext}} + v_{\text{H}} + v_{\text{xc}} - \mu\}dr = 0, \tag{1.10}$$

where, $v_{\text{xc}}(r)$ potential is the so-called exchange correlation potential, which is defined as:

$$v_{\text{xc}}(r) = \frac{\delta E_{\text{xc}}}{\delta n(r)}. \tag{1.11}$$

Similarly, the minimization of KS energy in the auxiliary potential V_s gives:

$$\delta E^{\mathrm{KS}} = \int \delta n \{ \frac{\delta T_{\mathrm{KS}}[n]}{\delta n} + V_s(r) - \mu' \} dr = 0. \tag{1.12}$$

Here, the minimization of the total energies in Eq.(1.10), and Eq.(1.12) with respect to the variation of $n(r)$ is imposed so that the total number of electrons is kept fixed, which is obtained by introducing the Lagrange multipliers, μ and μ', respectively. Putting these two equations together, one obtains:

$$V_s(r) = v_{\mathrm{ext}}(r) + v_{\mathrm{H}}(r) + v_{\mathrm{xc}}(r). \tag{1.13}$$

Eq.(1.12) is the Euler-Lagrange condition for a system of non-interacting particles moving in an effective external potential $V_s(r)$. Minimizing the interacting ground state energy functional $E_{\mathrm{GS}}[n]$ in Eq.(1.7) is therefore equivalent to solve self-consistently the following equations:

i) The Schrödinger equations for the independent electrons in the local effective potential, $V_s(r)$, is solved:

$$\big[-\frac{\hbar^2}{2m}\nabla^2 + V_s(r) \big] \varphi_i(r) = \varepsilon_i \varphi_i(r). \tag{1.14}$$

ii) The electron density of the system is estimated from the KS orbitals that are solution of (i) as follows:

$$n(r) = \sum_{i=1}^{N} |\varphi_i(r)|^2. \tag{1.15}$$

iii) The local KS potential $V_s(r)$ is updated with respect to the given electron density,

$$V_s(r) = v_{\mathrm{ext}}(r) + e^2 \int \frac{n(r')}{|r - r'|} dr' + v_{\mathrm{xc}}[n(r)] \tag{1.16}$$

The solutions of KS equations are obtained by an iterative procedure in which the total energy at each cycle is constructed until convergence is attained. The total energy then can be obtained as:

$$E[n] = \sum_i \varepsilon_i - \int V_s(r) n(r) dr + E_{\mathrm{ext}} + E_{\mathrm{H}} + E_{\mathrm{xc}}. \tag{1.17}$$

In practical implementation of the theory, one usually introduces an approximate expression for the exchange-correlation energy in terms of the density or the Kohn-Sham orbitals such as the well known Local Density Approximation (LDA) or Generalized Gradient Approximation (GGA). In the first part of this thesis, the above procedure for solving KS equations will be used, while in the second part, we will explore the steps needed to compute the exchange-correlation energy following the adiabatic-connection fluctuation-dissipation formulism.

1.3 Plane Waves Pseudopotential Methods

In order to solve practically KS equations in Eq.(1.14), one needs to address two main issues: (i) to introduce a convenient wave function representation to reduce the KS equations to standard linear algebra, and (ii) to efficiently deal with the difficulties introduced by the strong attractive electron-ion interaction.

1.3.0.1 Kohn-Sham equations in the plane wave basis set

In perfect crystalline solids, electrons are characterized by moving in a periodic effective potential. The periodicity of the potential allows to consider wave-function of electrons in the crystal through Bloch's theorem with the following formula:

$$\varphi_{j,\mathbf{k}}(r) = e^{i\mathbf{k}r} u_{j,\mathbf{k}}(r). \tag{1.18}$$

Where, $u_{j,\mathbf{k}}(r)$ is a periodic function such that $u_{j,\mathbf{k}}(r) = u_{j,\mathbf{k}}(r + \mathbf{R})$ for all lattice vectors $\mathbf{R}$, while the first term is a phase factor characterized by Bloch's vector, $\mathbf{k}$. In this derivation, wave-functions of electrons for different values of $\mathbf{k}$ can be treated separately. Assuming Periodic Boundary Condition (PBC), $\mathbf{k}$ is a real vector, that spans the whole first Brillouin zone of the reciprocal lattice. In practice, Brillouin zone integration is performed considering finite K-point grids.

Through this approach, one can see that the study for a periodic system in PBC becomes very convenient. However, in applications of electronic structure calculations, there are also several systems that do not have a full three dimensional translational symmetry such as liquid, amorphous or isolated molecules or surfaces. In this case, a supercell technique is usually introduced to recover periodicity, and this technique allows to represent periodically the systems through space.

In Eq.(1.18), the periodic function, $u_{j,\mathbf{k}}(r)$, must be represented in a convenient basis set. While there are many possible choices, Plane-wave (PW) basis set is naturally chosen since its formalism is simple, and it has a similar expansion to free electron systems. In this representation, Eq.(1.18) is written in the form:

$$\varphi_{j,\mathbf{k}}(r) = \frac{1}{\sqrt{\Omega}} \sum_G C_{j,\mathbf{k}}(G) e^{i(G+\mathbf{k})r} = \sum_G C_{j,\mathbf{k}}(G) \phi_{\mathbf{k}}(G), \tag{1.19}$$

with

$$\phi_{\mathbf{k}}(G) = \frac{1}{\sqrt{\Omega}} e^{i(G+\mathbf{k})r} \tag{1.20}$$

where $C_{j,\mathbf{k}}(G)$ are expansion coefficients that give the reciprocal space representation of the orbitals, and G are reciprocal lattice vectors. The pre-factor, $\frac{1}{\sqrt{\Omega}}$, preserves the normalization of wave-function in the crystalline-unit cell, so that we have:

$$\int_\Omega dr |\varphi_{j,\mathbf{k}}(r)|^2 = 1 \tag{1.21}$$

and

$$\sum_G |C_{j,\mathbf{k}}(G)|^2 = 1. \tag{1.22}$$

In a PW basis set representation, matrix elements for the kinetic and effective potential contributions to the KS Hamiltonian have very simple expression. The kinetic energy is diagonal in reciprocal space:

$$T^{\mathbf{k}}_{G,G'} = -\frac{\hbar^2}{2m_e} < \phi_{\mathbf{k}}(G)|\nabla^2|\phi_{\mathbf{k}}(G') >= -\frac{\hbar^2}{2m_e}|\mathbf{k}+G|^2\delta_{G,G'}, \tag{1.23}$$

and the local KS potential, $V_s(r)$, in Eq.(1.16) is represented by

$$V_s^{G,G'} =< \phi_{\mathbf{k}}(G)|\hat{V}_s|\phi_{\mathbf{k}}(G') >= \frac{1}{\Omega}\int V_s(r)e^{-i(G-G')r}dr = \tilde{V}_s(G-G'). \tag{1.24}$$

Where, because $\hat{V}_s$ is a periodic potential, it can be rewritten through the components of its Fourier transformation, $\tilde{V}_s(G-G')$. The KS equations presented in this basis set finally become a problem of looking for the expansion coefficients of plane waves for each state j whose eigenvalue is $\varepsilon_{j,\mathbf{k}}$

$$\sum_{G'}\big[-\frac{\hbar^2}{2m_e}|\mathbf{k}+G|^2\delta_{G,G'} + \tilde{V}_s(G-G')\big]C_{j,\mathbf{k}}(G') = \varepsilon_{j,\mathbf{k}}C_{j,\mathbf{k}}(G). \tag{1.25}$$

Solving for Eq.(1.25) is equivalent to an eigenvalue and eigenvector problem. In principle, the size of the matrix on the right-hand-side of Eq.(1.25) can go up to infinity. However, because the matrix diagonal is dominated by kinetic energy, and the contribution of high Fourier components in the low-lying orbitals decay with increasing $|\mathbf{k}+G|^2$, the infinite dimensional problem can be reduced to a finite dimensional one by introducing a cutoff energy, E_{cut}, and restricting the basis set to PW such that:

$$\frac{\hbar^2}{2m_e}|\mathbf{k}+G|^2 < E_{\text{cut}}. \tag{1.26}$$

The convergence of DFT results can be checked by increasing E_{cut}.

The ground state electron charge density $n(r)$ is calculated by performing an integration over the first Brillouin zone, and sum over all the occupied states.

$$n(r) = \sum_{\mathbf{k}}\sum_{j}\omega_{\mathbf{k}}\theta(\varepsilon_F - \varepsilon_{j,\mathbf{k}})|\varphi_{j,\mathbf{k}}(r)|^2 \tag{1.27}$$

where ε_F is the Fermi energy, and ω_k is the weight of $\mathbf{k}$ point in the first Brillouin zone. The charge density can be expanded in plane waves as,

$$n(r) = \frac{1}{\Omega}\sum_{Q} e^{iQr}\tilde{n}(Q). \tag{1.28}$$

The number of Q vectors to be used in Eq.(1.28) is determined by E_{cutrho} as,

$$\frac{\hbar^2}{2m_e}|Q|^2 < E_{\text{cutrho}} \tag{1.29}$$

The maximum modulus of Q vectors in Eq.(1.28) is twice the maximum modulus of G in Eq.(1.20), which means, in practice, $E_{\text{cutrho}} = 4E_{\text{cut}}$.

1.3.0.2 Pseudopotential method

The direct use of a PW expansion faces difficulties in general systems due to the strongly attractive electron-ion interaction that determines strong localization around the nuclei of the chemically inert core electrons and strong and rapid oscillations in the core region of the chemically important valence orbitals, due to the orthogonality requirement with respect to core electrons. In principle, the rapid oscillations of the valence orbitals requires a large number of PW basis functions for their representation, hence, it induces a huge CPU memory and time requirement. In practice, in order to solve for this problems, methods known as all electron calculations such as the Full-Potential Linearized Augmented Plane Wave (FLAPW) and the Full-Potential Linearized Muffin-Tin Orbital (FPLMTO) approaches have been introduced.

In addition, the Pseudopotential (PP) approach is also widely known as an efficient method to solve this problem. The main idea of PP method is based on the fact that most properties of materials such as chemical reactivity, bonding formations, etc depend strongly on the valence electrons, while the core electrons are quite inert in these cases. This, therefore, allows to consider the core electrons and nucleus as a rigid core. On the background of the ion cores composed by nuclei and inert core electrons, the sea of valence electrons can be seen as moving in an effective potentials, or so-called pseudo-potential, induced by these ion cores.

Moreover, in PP, the wave functions of the valence electrons are represented as pseudo-wave functions. The new wave functions are constructed ideally so that the pseudo wave functions have no radial nodes within the core region and that the pseudo wave functions and potential are identical with the true wave functions and potential outside some cut-off radius r_{cut}. Furthermore, PP must preserve the atomic properties of the element, including phase shifts on scattering across the core, which actually can be shown to be connected with the norm-conserving conditions [23].

In solids, PP is represented via an effective potential that combines the local potential induced by the effective nucleus (formed by nuclei and core electrons) and valence electrons, $V_{\text{local}}(r)$, plus non-local terms mimicking orthogonality between core and valence electrons, $V_{\text{NL}}(r, r')$:

$$V_{\text{eff}}(r) = V_{\text{local}}(r) + V_{\text{NL}}(r, r'). \tag{1.30}$$

This representation is often called semilocal pseudo-potential form because this potential is local in the radial variable and nonlocal in the angular variables. The non-local potential, $V_{\text{NL}}(r, r')$, is a short ranged non-local term, which, by construction, has to be angular-momentum dependent,

$$V_{\text{NL}}(r, r') = \sum_{I} \sum_{l,m}^{max} V_{lm}^{I}(|r - R_I|)\delta(|r - R_I| - |r' - R_I|)P_{lm}(r, r'), \tag{1.31}$$

where R_I is position of the I^{th} atom. P_{lm} is the projector on the angular momentum, l, m. The construction for V_{lm} is done separately on each atom starting from

the all-electron solution, and V_{lm} should satisfy the norm-conserving conditions as mentioned above. One can see that the semi-local form of this pseudopotential is not very efficient for practical calculation. In a PW basis set representation, it would require to keep in memory the matrix $< k+G|V_{\text{eff}}(r)|k+G' >$ that becomes rapidly very big for large systems.

For convenience, Kleinman and Bylander have proposed a replacement for the non-local pseudopotential in Eq.(1.31) by a fully separable form [24]:

$$V_{\text{NL}}^{\text{KB}}(r,r') = \sum_{l,m} \frac{|V_{lm}\psi_{lm}^{\text{PS}} >< \psi_{lm}^{\text{PS}} V_{lm}|}{< \psi_{lm}^{\text{PS}}|V_{lm}|\psi_{lm}^{\text{PS}} >} \tag{1.32}$$

where, ψ_{lm}^{PS} are pseudo wave-functions calculated on each individual atoms. This derivation allows to represent the matrix element of the non-local part of the potential between two plane waves G and G' in the form of two independent integrals, one depending on $k+G$ and the other on $k+G'$.

On the other hand, in some cases, especially for p states in first-row elements and d states in first-row transition metals, as in O $2p$ or Cu $3d$, these states are not orthogonal to any other core state of the same angular momentum. They therefore are nodeless and quite compressed compared to other valence states, which makes them requiring a large number of PWs to be represented accurately. The pseudo representation of these wave functions is not much smoother than the all-electron ones because their charge must respect the norm conserving condition, and must match the charge of the all-electron wave function. To overcome this problem, Vanderbilt [25], introduced a more general formalism for pseudopotential construction that allows to relax the norm-conserving condition so that the pseudo potential is much smoother but still highly transferable. This method has been called as ultrasoft pseudopotential.

In this thesis, ultrasoft pseudopotentials will be employed in the catalysis problem where the system consists of d-metals, i.e. Ag and Cu, and other atoms such as C, O, H, while, in the ACFDT problems, the calculations will be done only with norm-conserving pseudopotentials for Be and other atoms [26].

1.4 Approximations for the Exchange-Correlation Functional

As it has been discussed when introducing KS formulation, the solution of KS equations yields the exact ground-state energy E and density $n(r)$ of the many-body electron system provided the exact exchange-correlation energy functional, $E_{\rm xc}[n]$, and its functional derivative $\delta E_{\rm xc}[n]/\delta n(r)$ are known. During the development of DFT, many approximations of $E_{\rm xc}$ functional have been investigated and applied to different practical applications. A suggestive picture proposed by Perdew [27] has depicted the hierarchy of DFT approximations as a "Jacob's ladder" rising from the "earth of Hartree world" to the "heaven of chemical accuracy", see in Fig.(1.1). The

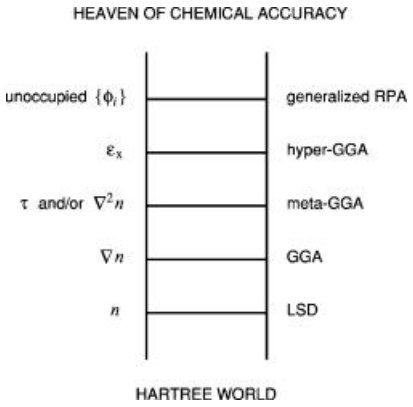

Figure 1.1: Jacob's ladder is presented for approximated levels of exchange-correlation energy.

first rung in the Jacob's ladder is the local density approximation (LDA) that is the most popular approximation being used for decades. This approximation was first proposed by Kohn and Sham in their original paper on KS method [9]. The formula of this approximation is based on the two main ideas that: i) the exchange correlation energy of a general inhomogeneous electron system can be obtained in term of an integral of local contributions, and ii) the expression of the exchange-correlation energy density, $\varepsilon_{\rm xc}(r,[n(r)])$, can be expressed in term of the exchange-correlation hole of the homogeneous electron gas which is already known [28]. The exchange correlation energy is therefore simply defined by an average over the system with respect to exchange-correlation density at each point r in space that associates with the density $n(r)$:

$$E_{\rm xc}[n(r)] = \int \varepsilon_{\rm xc}(r,[n(r)])n(r)dr. \tag{1.33}$$

Where, the expression of $\varepsilon_{\rm xc}(r,[n(r)])$ is written explicitly with respect to the exchange correlation hole functional, $\tilde{n}_{\rm xc}(r,r')$ as

$$\varepsilon_{\rm xc}(r,[n(r)]) = \frac{1}{2}\int dr' \frac{\tilde{n}_{\rm xc}(r,r')}{|r-r'|}. \tag{1.34}$$

LDA has been shown very successful in systems in the limit of high density or of slowly varying charge-density distribution. The calculations have shown that LDA is very successful in describing structural and vibrational properties for weakly correlated material such as semiconductor and simple metals. However, a number of failures of LDA are also known such as its tendency to overestimate crystal cohesive and molecular binding energies. Specially, LDA yields inaccurate results for strongly correlated systems such as transition-metal oxides.

In order to improve for LDA, Generalized Gradient Approximation (GGA), a higher level of approximation has been proposed by Perdew and Wang in 1992 [29]. In this approximation, one has modified the inhomogeneities issues in LDA formalism by considering the dependence of E_{xc} not only on local-density $n(r)$ but also on its gradients, $\nabla n(r)$. The general formula for exchange-correlation energy in GGA is:

$$E_{\mathrm{xc}}[n(r)] = \int \varepsilon_{\mathrm{xc}}^{\mathrm{GGA}}(n(r), \nabla n(r)) n(r) dr = \int \varepsilon_{\mathrm{xc}}(r) F_{\mathrm{xc}}(n(r), \nabla n(r)) n(r) dr, \tag{1.35}$$

where, $\varepsilon_{\mathrm{xc}}[n(r)]$ is the exchange energy per particle of the uniform electron gas, given in Eq.(1.34). F_{xc} is a dimensionless factor that can be decomposed linearly into exchange contribution F_{x} and correlation contribution F_{c}, $F_{\mathrm{xc}} = F_{\mathrm{x}} + F_{\mathrm{c}}$. The detailed treatments of F_{x} and F_{c} in different GGA versions can be referred in Ref. [30]. In practice, GGA-PBE proposed by Perdew, Burke and Enzerhof [31] is one of the most popular versions of GGAs. The calculations with GGA-PBE have shown results for properties such as binding energy of molecules with surface, activation energy, etc. in better agreement with experiments compared to LDA [32]. Therefore, on the Jacob's ladder GGA is seen as the second rung, higher than LDA.

The third rung of the ladder is meta-GGA, which expands GGA to include further the kinetic energy density, and/or the Laplacian of the density $\nabla^2 n(r)$. The general idea for constructing the functional is in the same spirit as GGA. In that respect, while adding higher orders of gradients to the expansion, it retains the good computational properties of the lower level approximations such as LDA and GGA [33].

The fourth rung is formed by the hybrid methods (or hyper-GGA functionals) that introduce nonlocality by replacing some portion of the local exchange energy density with the exact (HF-like) exchange energy density. The most popular of such hyper-GGA flavors is B3LYP functional [34, 35, 36], which has been shown to provide accurate predictions for thermochemistry of small covalent systems [37]. However, B3LYP gives poor predictions for noncovalent bonding interactions and reaction barrier heights, and the computational performance dramatically deteriorates with increasing size of the system [38].

The final rung of Jacob's ladder is given by the generalized RPA functionals. Derivation for exchange-correlation energy in this functional, in principle, utilizes the unoccupied, in addition to the occupied, KS orbitals. Therefore this rung is expected to give results close to the chemical accuracy over broad applications. In particular, employing this functional into DFT has shown very good accuracy for

thermochemistry, reaction barriers [39, 20, 19], and also ability in accounting for van der Waals (vdW) energy [11]. However, the complexity of the RPA expressions has prevented their wider application so far.

In this thesis, GGA-PBE functional will be employed in the study of catalytic properties. The accumulation of results of DFT calculations over the past decade has shown that, in spite of its simple form, GGA-PBE functional gives reliable accuracy in describing strong covalent and metallic, chemical bonds, together with great efficiency, allowing to treat big systems. On the other hand, vdW interaction remains challenging, and in order to better understand the non-local correlation effects giving rise to weak vdW bonding in simple molecules, we present our effort for the development and efficient implementation of "fifth-rung" functional that incorporates RPA correlation and exact-exchange (EXX) energy functionals.

Chapter 2

Modeling Selectivity of Ag-Cu Catalyst in Ethylene Epoxidation Reaction

Heterogeneous catalysis is one of the most important topics in modern chemistry. Chemical reactions occurring at catalyst surfaces can be accelerated or selective-controlled in order to produce the desired products. As recorded over the last decades, approximately more than 90% of the chemical industry processes are facilitated by catalysts, providing us with a wide range of products such as fertilizers, fuels, plastics, drugs, etc. In particular, heterogeneous catalysts play important roles in several fields involving environmental protection and energy conversion processes. Therefore, it can be said that the study of catalysts is of key importance for the present and future chemistry.

Several sophisticated experimental techniques in surface science and heterogeneous catalysis have been developed in order to provide a quantitative description of a range of surface phenomena. However, many applications of catalysts depend on detailed understanding at microscopic level such as the bond breaking and making of molecules and surface, and it, thus, needs a quantum mechanic description. Over the last couple of decades, it has been shown that the interactions can be simulated through computational models [5]. The availability of reliable theoretical models, computed with the ever increasing computer power and efficient algorithms, allows us to describe properly the properties of heterogeneous catalysis. In particular, advances in density functional theory (DFT) can interpret at the atomic scale characteristics of a chemical reaction occurring on the surfaces. Over many publications in this subject, DFT calculations have been found in quite good agreement with experimental data. It means that coupling between theory and experiment enables us to improve our understanding of this topic, i.e. DFT can result in predictions of catalytic properties of a new catalysts based on theoretical models before performing a complicate experiment.

In this work, one typical example of heterogeneous catalysis problem, ethylene epoxidation, will be studied. DFT approach and its related methods will show how the computational models can be used to understand the results obtained from experimental measurements for this reaction.

2.1 Heterogeneous Catalytic Partial Oxidation of Ethylene

2.1.1 Production of ethylene epoxidation: state of the art

Ethylene oxide (EO), with chemical formula C_2H_4O, is well known as an important chemical compound in modern chemical industry. EO is primarily used in the production of ethylene glycol (EG) and surface active agents such as detergent alcohol ethoxylates and nonionic alkylphenol ethoxylates [2]. EO is also a crucial component used in the derivation of several important fine petroleum and chemical intermediates, and it is therefore extensively used in applications such as washing/drying, electronics, pharmaceutics, pesticides, textiles, papermaking, automobiles, oil recovery and oil refining. The worldwide consumption of EO, as recorded in 2002, was 1.47×10^7 metric tons per year, and usage was divided among North America (44%); Western Europe (27%); Japan (20%); other Asia (6%); and other regions (3%) [40], which makes it the most utilized epoxide species, and stimulated a vigorous research activity over the last many years to understand and improve the production of EO.

EO is synthesized mainly from the direct oxidation of ethylene (C_2H_4) molecules. Ethylene-oxygen interaction, however, can occur via two different reaction pathways:

$$C_2H_4 + \frac{1}{2}O_2 \rightarrow C_2H_4O(\text{EO}) \tag{2.1}$$

or

$$C_2H_4 + \frac{1}{2}O_2 \rightarrow C_2H_4O(\text{Ac}) \dashrightarrow CO_2 + H_2O. \tag{2.2}$$

The creation of EO through the first path is also known as the selective, or partial oxidation (epoxidation) of ethylene path, while the second one, which is characterized by the formation of an acetaldehyde (Ac) intermediate state that is readily converted to carbon dioxide, is called total oxidation or combustion path. From a thermodynamic point of view, the second reaction is more favorable compared to the first one, i.e. the reaction enthalpy (ΔH) for the formation of EO is -25 kcal/mol, and for the total combustion, $\Delta H = -340$ kcal/mol [41]; therefore in a non-promoted condition, EO formation is very un-favorable. In 1931, Theodore Lefort discovered a new method for improving the formation of EO by using silver (Ag) particles to catalyze ethylene epoxidation, which, at present, has been applied widely in the industrial production of EO. Over more than 80 years, considerable research effort has been devoted to obtain more selective catalysts. However, Ag has emerged as the unique material that is at the same time active and selective for the formation EO in this reaction. Indeed, compared to its neighbors in the Periodic Table, Ag has been showed in both experiments and theory as an effective catalyst since besides selectivity for EO synthesis, it also optimizes reactivity in forming the oxygen- and ethylene-surface chemisorbed bonds [42, 43].

In industry, ethylene epoxidation is carried out over $\alpha-Al_2O_3$-supported Ag catalysts [44]. Ethylene epoxidation is usually carried out under conditions that

are either ethylene-rich (oxygen-based process) or equimolar to slightly oxygen-rich operation (if air is fed as the oxygen source). In the former condition, the typical ratio of ethylene and oxygen is from 3 : 1 to 4 : 1, whereas in the latter, this value is from 1 : 1 to 2 : 1 [45]. Furthermore, the conditions of temperature and pressure in this reaction are of $500 - 600$ K and $1 - 2$ MPa, respectively [44]. Moreover, in order to improve the EO selectivity in the industrial production, the current commercial silver-based catalysts are usually promoted by Cl, Cs, and Re that increases selectivity up to 90% [44].

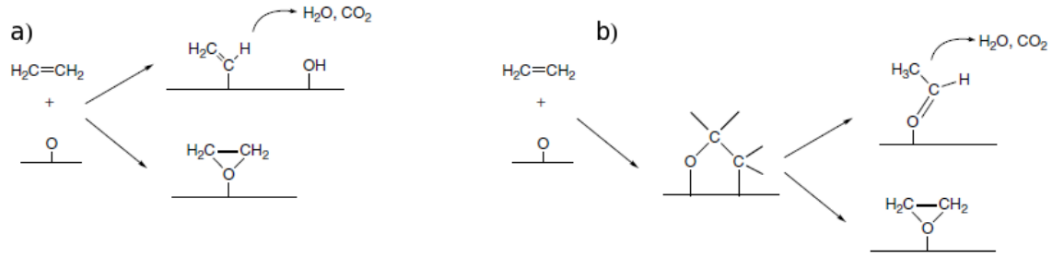

Figure 2.1: Sketches for ethylene epoxidation pathways a) the selective one is characterized by concerted addition of O across the C=C bonds, while the non-selective one is proceed via a surface vinyl intermediate, which is proposed in [44]. b) the oxametallacycles (OMC) is proposed as the intermediate that is selective forming ethylene oxide (EO) or acetaldehyde (Ac) final states. This mechanism is investigated by Barteau *et al.* [46].

To further increase the selectivity toward EO, it is necessary to get a good insight into the structural properties of catalysts as well as the mechanisms of reaction happening at surfaces. Considerable efforts have been devoted to understanding the mechanism of metal-catalyzed ethylene epoxidation. In the literature, a variety of possible reactive intermediates of the mechanisms has been discussed. In the earlier studies of ethylene epoxidation, van Santen and co-workers suggested that the formation of EO is characterized by addition of oxygen atom across the C=C double bond in ethylene molecules, which is competing with the un-selective pathway involving the surface oxygen-induced activation of ethylene C−H bonds, resulting in C−H scission and formation of −OH and vinyl adsorbates [44], see in Fig. 2.1(a). The vinyl intermediate in this second pathway rapidly reacts with additional surface oxygen and combusts to form CO_2 and H_2O [44]. The mechanism for total combustion received significant attention because the O−induced C−H bond activation on Ag is exothermic, and activation of C-H bonds by oxygen adsorbed on Ag has been obtained in hydrocarbons such as acetylene and propylene in ultra-high vacuum (UHV) experiments [47, 48, 49]. In contrast, the partial oxidation production of EO is a kinetically controlled step, which implies that the selectivity toward EO synthesis is determined by the reaction rate of the partial ethylene oxidation pathway [44].

Recently, an alternative mechanism has been proposed. In that case ethylene is oxidized on the silver surface to form an adsorbed intermediate that can lead either to the desired epoxy product or Ac that is more easily combusted. Such a mechanism was originally suggested by Cant and Hall to explain kinetic isotope effects on the rate and selectivity of ethylene epoxidation [50]. Later, in a series of alkene epoxidation studies (see Ref. [46] and references therein), Barteau *et al.* has provided compelling evidence that a surface oxametallacycle (OMC) is such "common intermediate", as shown in Fig. 2.1(b). The OMC intermediate is characterized by a $-O-C-C-$ back-bone where one C is bonded to a surface metal atom and the other C to a pre-adsorbed oxygen [46]. Surface OMC has been identified on the Ag(111) surface under UHV conditions by activated adsorption of EO. This intermediate reacts, mainly reforming EO, at ~ 300 K. The OMC intermediate has been identified, via high-resolution electron energy-loss spectroscopy (HREELS) [46] and high-resolution X-ray photoelectron spectroscopy (HRXPS) [51]. The activation barrier for ring-closure of the surface OMC to form EO was measured, in temperature-programmed desorption (TPD) experiments, as 68 kJ mol^{-1} [46]. In addition to these experimental observations, DFT calculations have suggested that surface OMC ring-closure to form EO is energetically possible under catalytic reaction conditions. Depending on the functional used and the particular implementation of DFT, the calculated activation barrier has been found to be between 60 and 85 kJ mol^{-1} that is in good agreement with the reported measured activation barriers [46, 52]. Similarly, A. Kokalj *et al.* [53] have computationally showed that OMC not only forms on (111) surface of pure Ag catalysts but can also form on other low-index orientations such as (100) and (110) or (210) surfaces. OMC is found in these works to act as the selective-controlling intermediate that allows the reaction paths going toward to either EO or Ac final states [53, 54], in which the reaction barrier of EO formation is compatible to those found in experiments on (111) surface. Furthermore, the authors have extensively considered OMC forming on other pure metal catalysts [53].

Another active area of study in ethylene epoxidation concerns the chemical states of adsorbed oxygen which, in some reports, are seen as one of the selectivity-controlling factors. It has been suggested that oxygen may be present in either a nucleophilic or an electrophilic form; the former would be active for total oxidation, while the latter would lead to epoxidation. Based on the first proposed reaction mechanisms in Fig. 2.1(a), it was suggested that electrophilic oxygen atoms would prefer to react with electron-rich ethylene double bond in the selective pathway, yielding ethylene oxide. On the other hand, the vinyl intermediate state, that would lead to the combustion, would more likely bind to nucleophilic oxygen. This hypothesis implies that electrophilic oxygen plays an important role in improving selectivity of ethylene epoxidation. The electrophilic oxygen has been postulated to be a surface (atomic) oxygen with chemical properties strongly modified by surface defects, or a surface oxide phase. In addition, the formation of sub-surface oxygen (O^{sub}) is also involved. O^{sub} is suggested as the promoter of improving selectivity of Ag. O^{sub}, in this case, is proposed to reduce the strength of the bonds of on-surface

oxygen, which facilitates the binding of on-surface oxygen with C=C double bond, forming EO [55]. However, DFT results recently show that this oxygen stabilizes the on-surface oxygen [56, 57, 58], and also increases the chemisorption energy of ethylene on pure Ag surface [57]. Mavrikakis *et al.* [57] computed the activation energy of reaction path forming EO from OMC intermediate states, and found that this energy is increased significantly with the presence of O^{sub}, which is suggested to be related to increase of binding energies of on-surface oxygen.

Several studies have confirmed that there are some elements in the Periodic Table that can be used as the promoters for improving the selectivity of Ag catalysts which are grouped into three categories: (i) alkalis, especially cesium and combinations of cesium with other alkalis; (ii) chlorine; (iii) early transition metal, such as rhenium, and other d−metals in some current high-selectivity catalysts. The use of promoters can increase the selectivity from $< 50\%$ for un-promoted catalysts to almost 90%. While cesium and chlorine promotion have been used in practice for decades, and have prompted a number of studies to try to explain their role, little information is available about the possible role of rhenium and other d-metals as the promoters.

In the case of Cs promotion, Barteau and co-workers have found experimentally that Cs significantly increases the selectivity of Ag as long as the amount of Cs is up to 80 ppm, while the promotion of Cs on activity of catalysts is quite small. In order to explain the role of Cs, the authors used DFT calculations to propose that Cs acts by altering energetic of OMC reactions. From this intermediate, the activation barrier for acetaldehyde formation on Ag(111) increases significantly with respect to the activation barrier for EO formation when Cs is co-adsorbed on the surface [59]. However, Cs is also known as a highly reactive element, therefore, during catalyst preparation the active sites on surfaces can be partially neutralized by ion exchange with Cs cations from solutions, and a lower yield of ethylene conversion percentage is usually found in this case [44]. Analogously, adding chlorine (Cl) to the catalyst also has been shown to increase the selectivity to EO [60, 61, 62, 63, 64]. Cl is continuously added to the reactor feed at ppm levels in the form of chlorinated hydrocarbons, such as dichloroethane ($C_2H_4Cl_2$) and vinyl chloride (C_2H_3Cl). It is generally found that the presence of Cl significantly increases the selectivity to EO while at the same time decreasing the rates of EO and CO_2 formation. Therefore, Cl works as a poison to inhibit the rate of carbon dioxide formation to a greater extent than EO formation.

The role of the last promoter group in changing the catalytic properties of Ag in ethylene epoxidation has been also studied for many years. Several d-metal additives have been shown to increase EO selectivity as well as Cs and Cl promoters. Verykios and co-workers examined several promoted-Ag systems and reported results for Zn [65], Au [66], Pd [67], and Cd [68] additives. Zn was found to have little effect on the Ag catalysts [65], while Cd was found to increase the turnover frequencies of both the combustion and epoxidation reactions [68]. In that work, Pd-promoted catalysts showed to increase only the rate of the combustion pathway (to decrease selectivity) [67]. A maximum was found in the activity of Au−impregnated catalysts, although the selectivity decreased with increasing Au loading [66]. Spectroscopic and diffrac-

tion techniques were employed to examine alloying of these promoters with Ag. Zn was not found to alloy with Ag, while Cd was [65]. The Au and Pd results were less certain, although alloying was assumed. Recently, Barteau and co-workers have combined the DFT modeling with scanning electron microscopy (SEM), electron-dispersive spectroscopy (EDS), and *ex situ* X-ray photoelectron spectroscopy (XPS) in order to provide the critical insights into the mechanism of ethylene epoxidation reaction happening on Ag particles promoted by additives such as Pd [69], Cd, Au, Pt, and Cu metals [70]. Firstly, the chemical reactions of ethylene epoxidation on the catalysts have been modeled through DFT simulations, which allows to predict the selectivity for different alloys [71], then experiments have been performed and compared to the computed results. The experimental data has showed that Pd also increases the activity and selectivity of Ag catalysts, agrees with those in calculation, while Pt and Au have been found to decrease selectivity, although the extent of the observed decrease with Pt addition is in conflict with the model prediction. Cd addition increased both the activity and selectivity of Ag, opposite to the predicted behavior. In particular, for the case of Ag promoted by Cu, both DFT and the experimental measurements show that this catalyst is significantly better in activity and selectivity compared to other promoters.

One can see that while selectivity promotion of alkalis and halogens is always followed by raising catalyst, price and decreasing catalysts activity, a wide usage of selective silver-based alloys, such as Ag-Cu alloy, into the EO industrial synthesis can be seen as a perspective in the near future. In order to understand the role of the additives in changing the catalysis property compared to pure Ag, the interpretation of the basic mechanism of ethylene epoxidation and chemical state of oxygen on the alloy surfaces should be studied analogously with pure Ag case. In the following, our studies will focus on the case of Ag-Cu alloy which was mentioned above as the most selective catalyst compared to others.

2.1.2 Selectivity improvement of Ag-Cu alloy catalyst

The improvement in selectivity of Ag-Cu alloy compared to pure Ag has been investigated by Barteau and co-workers. The authors used DFT methods to simulate an alloy model with 2-dimensional (2D) surface for Ag-Cu. The computed (111) surface is assumed by one out of four Ag atoms replaced by one Cu atom in a (2×2) cell. In this calculation, the role of Cu in improving the selectivity is understood through the effects on the OMC intermediate [72], given in Fig. 2.2. Later, DFT results have been tested experimentally at the laboratory scale and the measurements have shown that Ag-Cu bimetallic catalysts are more selective to EO than monometallic Ag catalysts over a wide range of Cu composition, see Fig. 2.3. The optimal selectivity was obtained with 0.2 to 0.5 (% mol) of Cu relative to Ag. Moreover, this selectivity enhancement is found to be maintained with the addition of conventional promoters such as Cs and Cl [73]. Increase of EO selectivity in this case has been estimated from 15 to 30% compared to promotion on Ag. In the same experimental setup, the authors also measured selectivity dependence on the

operating conditions such as oxygen and ethylene partial pressures [74]. While the latter dependence shows no effect on selectivity but activity that decreases with increasing ethylene partial pressures, the first one, on the other hand, improves the selectivity of EO formation, which has been explained with O^{sub} formation on Ag-Cu alloys [74]. Analysis of *ex situ* X-ray photoelectron spectroscopy (XPS) for this catalyst suggested that the surface of the catalyst is enriched with Cu [72], and the amount of Cu on surface is from 0.2 to 0.75 ML. Morphological changes of Ag catalyst particles in ethylene epoxidation reaction are also obtained by SEM, Fig. 2.4. This measurement also showed that once the content of Cu increases up to a certain value, the surfaces of Ag-Cu particles will be dominated by copper oxide phases that have structure different from that employed in DFT calculations suggested by the authors [72]. Since, in the conditions relevant for experiments, the formation of oxide on catalyst surfaces is very important [75], one needs to elucidate the role of Ag-Cu in increasing selectivity under these conditions [76].

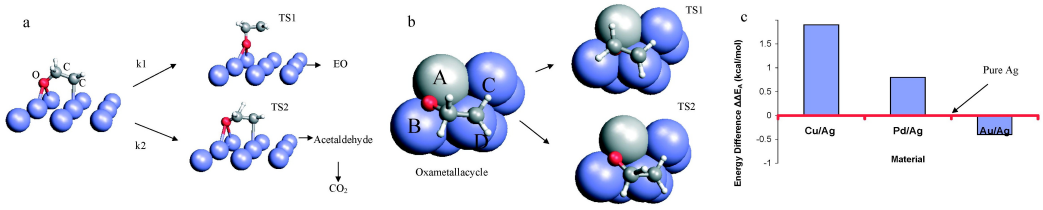

Figure 2.2: Computational design of ethylene oxide (EO) synthesis catalysts with improved selectivity [72]. a) Selectivity-controlling step from Oxametallacycle intermediate. TS1 and TS2 are the Transition States of pathways forming EO and Ac, respectively. b) Structure of the bimetallic model catalysts on which OMC is still assumed as the transition state. c) The selectivity descriptor, $\Delta\Delta E_A = (E^*_{Ac}(\text{alloy}) - E^*_{EO}(\text{alloy})) - (E^*_{Ac}(\text{Ag}) - E^*_{EO}(\text{Ag}))$, shown for a number of catalyst compositions. Positive value means that the bimetallic should be more selective than pure silver.

Recently, with the development of several experimental techniques for heterogeneous catalysis, the properties of the catalyst surface under conditions relevant for industrial production can be understood better. Employing *in situ* XPS experiments, Piccinin and co-workers have measured structural properties for Ag-Cu nanoparticles ($\sim$ 100 nm, 2.5 wt% Cu) at 520 K in O_2, H_2, and a C_2H_4:O_2 (1:2) atmospheres at a total pressure of 0.5 mbar [77]. XPS in this work shows that the valence spectra of Cu 3d in Ag-Cu samples are similar to those of Cu_2O and CuO ones. It indicates that Cu atoms on Ag-Cu alloy are in an oxide form; therefore, copper-oxide structure will play an important role in catalyzing ethylene epoxidation instead of pure Ag or Ag-Cu alloy. The analysis of these spectra also shows that the Cu content on the surface are significantly different when the ethylene and oxygen reactants are present compared to the case in vacuum ($\sim$ 50 times more surface copper compared to the nominal bulk composition). The surface structures obtained

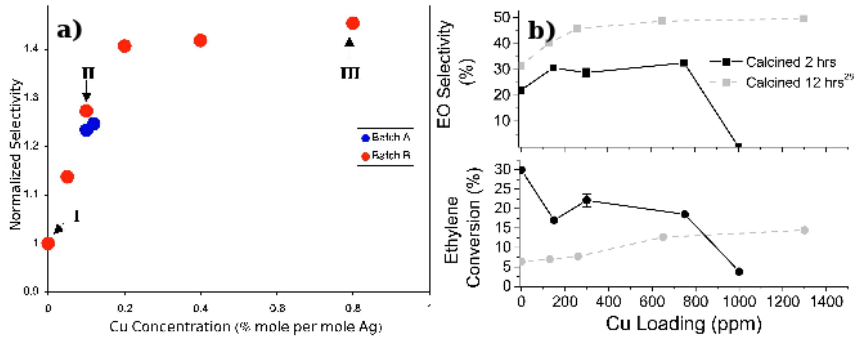

Figure 2.3: a) Normalized catalyst selectivity to EO of Ag-Cu relative to pure Ag under the same conditions as a function of bulk Cu content [72]. b)EO selectivity (top-panel) and Ethylene conversion (below-panel) results for Ag-Cu catalysts with respect to different calcination time: solid line is 2 hours, dashed line is 12 hour [76].

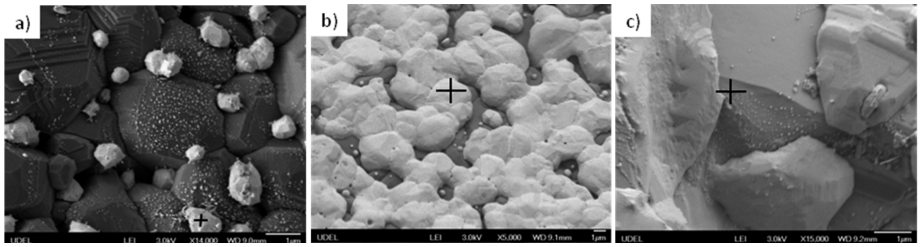

Figure 2.4: SEM images of Ag-Cu catalyst particles with different Cu contents: a) 300 ppm and b) 1000 ppm. c) SEM of support region of Ag-Cu particles with 1000 ppm Cu. White particles are Ag. Dark gray particles are α-Al_2O_3 [76].

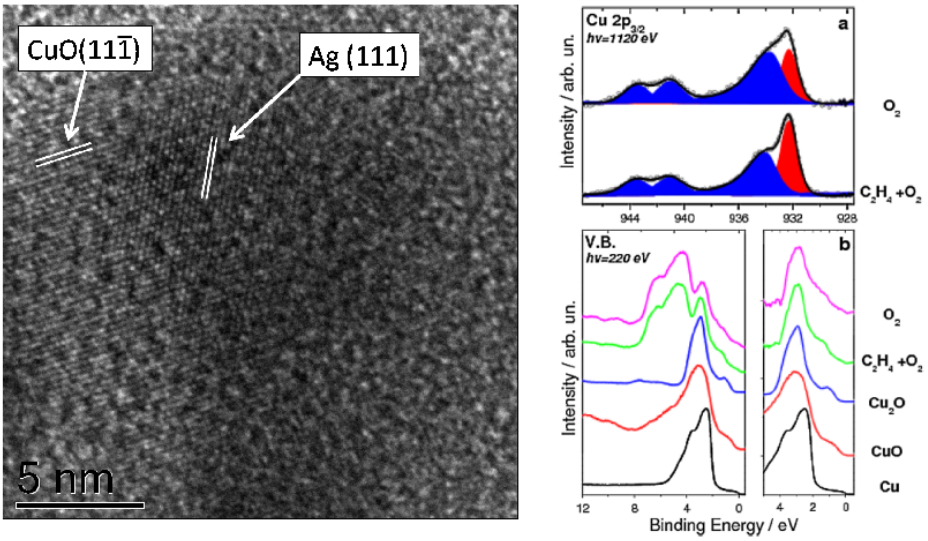

Figure 2.5: Experimental measurements of copper-oxide layer formation on Ag-Cu catalysts. In the left-panel: HRTEM image shows a silver particle partially covered with a 5 nm thick copper oxide layer. In the right-panel: a) the Cu $2p_{3/2}$ core level spectra of the Ag-Cu catalyst recorded under oxygen and reaction (C_2H_4:O_2) atmospheres (total pressure 0.5 mbar at 520 K). b) Valence band spectra of the Ag-Cu catalyst under oxygen and reaction atmospheres (left). The valence band region close to the Fermi edge obtained from the difference spectra between Ag-Cu and pure Ag samples (right). At the bottom, valence band spectra of reference oxides are given [77].

by the high resolution transmission electron microscopy (HRTEM), Fig. 2.5, show the segregation of Cu oxide patches on the surface of the Ag particles beside the pure Ag surfaces [77].

The experimental observations have been interpreted by first-principles electronic structure calculations [77]. It has been shown that the presence of oxygen in the reactive environment leads to copper segregation to the surface [78, 79], and around the temperature and pressure of interest for practical applications a thin layer of copper oxide on the top of silver surface is found, while the 2D alloy is not predicted to be stable [79, 78]. Therefore, the enhancement of the selectivity towards the formation of EO on Ag-Cu alloy should be understood under the effect of the thin oxide layer instead of a surface alloy. Moreover, by using thermodynamic equilibrium constrain methods, the stability of different structures that are proposed to be present on the surface during the ethylene converted to final EO or Ac products has been evaluated, suggesting that the surface of Ag-Cu alloy under this condition consists of energetically similar oxidic surface structures such as the thin CuO and AgO-CuO films on the Ag substrate. The structures are believed to be in dynamical coexistence. The results are supported by the experimental evidence that Cu is in an oxidized state and this is likely to have important consequences for the understanding of the mechanism by which Cu enhances the catalyst selectivity, since the active O species are O atoms which are part of an oxide layer, rather than O atoms chemisorbed on a metal surface [77].

2.1.3 Exploiting Brønsted Evan Polanyi principle

In heterogeneous catalysis, one of the most interesting findings through several studies of reactions on transition-metals is Brønsted Evan Polanyi (BEP) principle. That is found in 1928 by Brønsted [80], and Evan and Polanyi in 1938 [81]. This principle states a linear relation between activation energy (E^*) and enthalpy (ΔH) of an elementary reaction,

$$E^* = \alpha \Delta \mathrm{H} + \beta. \tag{2.3}$$

When using DFT for studies of catalytic reactions, the estimation of activation energies via the Nudge-Elastic-Band (NEB) method, that will be introduced fully later, is computational very demanding. In contrast, the calculations for enthalpy are much simpler. It means that, for a given elementary reaction, by employing BEP relation, a systematic study over a range of different catalyst surfaces can allow to predict the activation energy, E^*, of a new catalyst without performing the expensive calculations.

The accuracy of BEP principle and its applications have been extensively reported through many DFT calculations. In particular, Nørskov and co-workers have studied BEP principle for several dissociation reactions of different molecules on the catalysts [42]. The values of coefficients α and β in Eq.(2.3) of these reactions have also been obtained by scanning over many catalyst surfaces. The findings have provided useful approach for understanding the activity of existing catalysts in the reactions, and also allowed to predict the catalytic properties of new catalysts.

In ethylene epoxidation, the linear relation of BEP principle has been also examined for the reaction steps from OMC toward to EO and Ac final products on different surfaces. In particular, A. Kokalj *et al.* [53] have found that although the original form of BEP principle does not result a good predictor for selectivity of the catalyst, a modification for this relation can be employed as a selectivity indicator. In this thesis, the BEP principle in the reaction steps for the formation of EO and Ac products will be reconsidered to apply to the case of oxide-like layer structures of the Ag-Cu catalysts.

2.2 Computational Study of Chemical Reaction

In materials science, surface science and heterogeneous catalysis studies, computer simulations of surface processes can contribute significant insights regarding electronic properties, atomic-scale structure and transitions of chemical processes. The electronic description within Kohn−Sham density functional theory (DFT) has shown to be remarkably successful in numerous studies for the energetic properties of materials as well as catalyst surfaces. DFT calculations deal with electrons that are treated at their ground states corresponding to Born-Oppenheimer Adiabatic approximations, while other properties related to temperature and pressure usually are computed through kinetics of nuclei. In practice, several theoretical tools have been developed to depict properly the energetic and dynamic properties of the nuclei in systems such as Monte-Carlo, molecular dynamic, meta-dynamics, or saddle point finding methods, etc.

In this section, we will introduce the theoretical concepts that will be employed in the study of the heterogeneous catalysis problems in this thesis. Firstly, we will present an *ab initio* method allowing to incorporate the outcomes of DFT, such as forces and total energy, into modeling the surface catalyst that are possibly present under the temperature and pressure conditions relevant to experiments. Then, we will describe one possible approach to the study of rare events: the nudged-elastic band (NEB) method, which allows the calculation of reaction barriers for the elementary reaction steps on the selected catalyst structures.

2.2.1 Ab initio atomistic thermodynamics

In heterogeneous catalysis, having a detailed knowledge of the catalyst surfaces under operating conditions is a crucial first step toward understanding the full catalytic process at atomistic level. Classical surface science techniques operate in ultra high vacuum (UHV) and at room temperature or below, while industrial applications of heterogeneous catalysis usually require pressure of the order of atmospheres and temperatures often higher than room temperature. The information extracted from such surface science experiments cannot always be extrapolated to realistic conditions since structures that can exist at high temperature and pressure might not be seen in UHV conditions and vice versa. The difference in ambient conditions is usually referred to the pressure and temperature gaps, and trying to bridge these differences is one of the major goals in current surface science research [82].

In theoretical calculations, in order to overcome the above issue, well known methods such as lattice-gas Hamiltonian, equilibrium Monte-Carlo simulations or kinetic Monte Carlo simulations have been developed and employed for different particular type of problems [5, 6]. These methods are successful in describing the phenomena in heterogeneous catalysis at the macroscopic scales, such as the dynamic properties of adsorption, desorption, or diffusion of reactants and fluctuation or growth of surface structures, ect. However, there are also drawbacks in these methods. For example, since the force fields used in these methods are constructed

via classical ones with parameters extracted from DFT calculations, one do not have a detailed electronic information of the interaction between reactants and catalyst, and also the accuracy of these calculations is lower than that obtained directly from DFT calculations [5, 6].

On the other hand, understanding at the microscopic level phenomena, for example elementary processes such as bond-forming or -breaking of each molecule with the surfaces, is also crucial in determining the electronic properties of catalysts. While energetics of the microscopic processes can be addressed accurately by DFT calculations, the effects of atmosphere (T and p) can provide a picture of their thermodynamics. One approach for this aspect has been proposed recently by Scheffler and co-workers [83, 84, 85], and named *ab initio atomistic thermodynamics*. In this method, systems are assumed to be in thermodynamic equilibrium conditions where the appropriate thermodynamic potential functions, like the Gibbs free energy, can be calculated from the outcomes of DFT calculations. Then, the macroscopic system properties are studied through the standard methodology of thermodynamics. For a large system, this approach allows to decompose it into subsystems that are mutually in equilibrium with each other. Each of the subsystems is of course simpler, and can be treated separately. The contact between the subsystems is established by relating their corresponding thermodynamic potentials. This treatment can be efficient for an infinite systems such as a bulk surrounded by gas phases. The homogeneous parts like bulk or surrounding gases can be separated off, and then represented by corresponding reservoirs.

In heterogeneous catalysis, *ab initio thermodynamics* assumes that a catalysis system is composed by (i) the deep layers of catalyst surfaces that are in equilibrium with their bulk phases, (ii) the homogeneous gas phases such as oxygen or ethylene molecule gases that are treated as reservoirs, and (iii) the portion of the surface of the catalyst at which chemical reactions between reactants can occur. Therefore, in order to examine the stability of different surface structures, the Gibbs free surface energy is usually used, which allows to evaluate the variation of free energy of the catalyst surface with the adsorption of reactants, $G^{\text{total}}(T,p)$ compared to those of clean surface, $G^{\text{slab}}(T,p)$,

$$\gamma(T,p) = \frac{1}{A}\{G^{\text{total}}(T,p) - G^{\text{slab}}(T,p) - \sum_M N_M \mu_M(T,p) - \sum_i N_i \mu_i(T,p)\} \quad (2.4)$$

here A is the area of the surface unit cell, $\mu_i(T,p)$ and $\mu_M(T,p)$ are the chemical potential of reactants and metal atoms, respectively. N_i is the number of reactants present on surface, while N_M is the number of metal atoms added/removed to/from the surface compared to the clean slab. If we consider an alloy catalyst, that is a mixture between the based-metal and solutes, the solutes are assumed to be in equilibrium with their bulk reservoir. In Eq.(2.4), the solid phase Gibbs free energies, $G^{\text{slab}}(T,p)$, and $G^{\text{total}}(T,p)$ are approximately considered to be contributed by several terms. For example, in the case of $G^{\text{slab}}(T,p)$, we have:

$$G^{\text{slab}}(T,p) \approx E^{\text{total}} + F^{\text{vib}} + pV, \quad (2.5)$$

where V is volume of the system. E^{total} is the total energy that is evaluated by DFT methods, and F^{vib} is the vibration free energy. In Eq.(2.5), the dominant term is the total energy. Checking for the last term, one can find from a dimensional analysis that its contribution to $\gamma(T,p)$ is of the order of $\sim$ atm Å^3/Å^2 = 10^{-3} meV/Å^2, that is sufficiently small compared to the total energy. The vibrational contributions to the free energy, which in principle should be accounted for, have been shown to be sufficiently small so as not to play an important role for the O/Ag system [56]. When comparing systems with different stoichiometries, on the other hand, vibration contributions might play a non-negligible role. In order to estimate for F^{vib}, in practice, one needs to obtain the phonon density of state (DOS) of the vibration model (i.e. Einstein model) on the surfaces. An analytic expression for F^{vib} can be seen in Ref. [83]. However, it is worth to note here that, in Eq.(2.4), a difference of surface vibration free energy, $\Delta F^{\text{vib}}/A$, is of interest rather than an absolute value of F^{vib}. In calculations for $RuO_2(110)$ surface, Reuter *et al.* showed that $\Delta F^{\text{vib}}/A$ always stays within $\sim \pm 10$ meV/Å^2 for the entire range of temperature up to 1000 K. Similarly, on the Ag-Cu(111) surface, Piccinin *et al.* have shown that accounting for these contributions changes $\gamma(T,p)$ of $\sim \pm 10$ meV/Å^2 in the range of temperatures of interest $(0-1000$ K) [79]. These estimates indicate that such contributions are indeed small and that neglecting these terms will not alter the main conclusions of the work. Hence, within this model, the only term that depends on T and p is the chemical potential of the gas phases. As a consequence, the free energies G^{slab}, and G^{total} are approximated with the total energies E^{total}, and E^{slab}, respectively. Moreover, the removed metal atoms are assumed to be in equilibrium with it bulk reservoirs, $\mu_M(T,p) = E_M^{\text{bulk}}$. The definition of surface free energy, therefore, becomes :

$$\gamma(T,p) = \frac{1}{A}\{E^{\text{total}} - E^{\text{slab}} - \sum N_M E_M^{\text{bulk}} - \sum N_i \mu_i(T,p)\}. \tag{2.6}$$

Here, we also note that *ab initio atomic thermodynamics* can be seen as an approximate approach to study heterogeneous catalysis at steady-state condition where the systems are close to thermodynamic equilibrium (or a constrained equilibrium) to prevent catalyst degradation [6].

2.2.1.1 Gas phase chemical potential

In this section, we discuss how to directly extract the chemical potential values of gas-phase species, μ_i, from the standard thermochemical tables [86], and relate it to temperature and pressure conditions. According to the definition of thermodynamic equilibrium of reactants with their surrounding gas phase reservoir, the chemical potentials are approximated as those of the ideal gases; and are therefore defined by the Gibbs free energy per unit atom or molecule

$$\mu(T,p) = (\frac{\partial G}{\partial N})_{T,p,N} = \frac{G}{N}. \tag{2.7}$$

The Gibbs free energy is the thermodynamical potential function depending on pressure and temperature, so its total derivative can be written as:

$$dG = (\frac{\partial G}{\partial T})_p dT + (\frac{\partial G}{\partial P})_T dp = -SdT + Vdp, \tag{2.8}$$

where the Maxwell relations for the energy, S and volume, V is employed. Using the ideal gas equation of state, $pV = NkT$, the partial derivative of $G(T,p)$ with respect to pressure at constant temperature is consequently

$$(\frac{\partial G}{\partial p})_T = V = \frac{NkT}{p}. \tag{2.9}$$

In turn, a finite pressure change from pressure, p^o, to the finite value, p, results in

$$G(T,p) - G(T,p^o) = \int_{p^o}^{p} (\frac{\partial G}{\partial p})_T dp = NkT \ln(\frac{p}{p^o}). \tag{2.10}$$

Combining Eqs.(2.7 and 2.10), for the chemical potential of reactant gases we can finally write

$$\mu(T,p) = \mu(T,p^o) + kT \ln(\frac{p}{p^o}) \tag{2.11}$$

where, $\mu(T,p^o)$ is the so-called chemical potential at standard pressure, p^o. It is given by

$$\mu(T,p^o) = E^{\text{total}} + \Delta\mu(T,p^o) \tag{2.12}$$

where, E^{total} is the total energy of the isolated molecule in the gas. The increment of chemical potential at standard pressure with respect to 0 K, $\Delta\mu(T,p^o)$ is evaluated by:

$$\begin{aligned} \Delta\mu(T,p^o) &= \mu(0,p^o) + \Delta G(T,p^o) \\ &= [H(T,p^o) - H(0,p^o)] - T[S(T,p^o) - S(0,p^o)], \end{aligned} \tag{2.13}$$

where the relation $G = H - TS$ between the Gibbs free energy G and the enthalpy H is employed. It allows us to obtain the desired temperature dependence simply from the differences in enthalpy and entropy of gas molecule with respect to the $T = 0$ K limit.

The evaluation for this expression can be obtained from the NIST-JANAF thermochemical tables [86] that give us the information of enthalpy H and entropy S at the standard pressure p^o and different finite temperatures T. Moreover, an alternative approach can also directly calculate by first-principle calculations for each atom or molecule in gas phase [83, 85].

In the ethylene epoxidation reactions, the chemical potentials of the two reactant gases, ethylene and oxygen, mainly contribute to the reaction. From the above expansion, the chemical potential of ethylene molecule, for example, is explicitly calculated through:

$$\mu_{C_2H_4}(T,p^o) = E^{\text{total}}_{C_2H_4} + \Delta\mu_{C_2H_4}(T,p^o) \tag{2.14}$$

Table 2.1: $\Delta\mu_{C_2H_4}(T,p^o)$ and $\Delta\mu_O(T,p^o)$ in the temperature range of interest to our study. The entropy and enthalpy change used to obtain $\Delta\mu_{C_2H_4}(T,p^o)$ and $\Delta\mu_O(T,p^o)$ via Eqs.(2.15 and 2.17), respectively are taken from thermodynamical table at $p^o = 1$ atm.

T(K)	$\Delta\mu_O(T,p^o)$ (eV)	$\Delta\mu_{C_2H_4}(T,p^o)$ (eV)
100	-0.08	-0.15
200	-0.17	-0.35
300	-0.27	-0.57
400	-0.38	-0.81
500	-0.50	-1.06
600	-0.61	-1.32
700	-0.73	-1.59
800	-0.85	-1.88
900	-0.98	-2.17
1000	-1.10	-2.48

with

$$\begin{aligned}\Delta\mu_{C_2H_4}(T,p^o) =& [H(T,p^o,C_2H_4) - H(0,p^o,C_2H_4)] \\ & -T[S(T,p^o,C_2H_4) - S(0,p^o,C_2H_4)].\end{aligned} \tag{2.15}$$

The chemical potential of oxygen can be simply chosen as $\mu_O = \frac{1}{2}\mu_{O_2}$,

$$\mu_O(T,p^o) = E_O^{\text{total}} + \Delta\mu_O(T,p^o) \tag{2.16}$$

with

$$\begin{aligned}E_O^{\text{total}} &= \frac{1}{2}E_{O_2}^{\text{total}} \\ \Delta\mu_O(T,p^o) &= \frac{1}{2}\Delta\mu_{O_2}(T,p^o) \\ &= \frac{1}{2}[H(T,p^o,O_2) - H(0,p^o,O_2)] \\ &\quad - \frac{1}{2}T[S(T,p^o,O_2) - S(0,p^o,O_2)].\end{aligned} \tag{2.17}$$

In this work, the enthalpy and entropy of O_2 and ethylene molecules are extracted, at standard pressure $p^o = 1$ atm, from the NIST-JANAF thermochemical tables [86]. The total energy for these isolated molecules are calculated by ab initio (DFT) methods. Inserting them into Eqs.(2.15 and 2.17) leads finally to $\Delta\mu_O(T,p^o)$ and $\Delta\mu_{C_2H_4}(T,p^o)$, which we list in Table 2.1.

2.2.2 Reactivity and Selectivity in Thermalized Chemical Reaction

In heterogeneous catalysis, understanding and then improving properties such as activity and selectivity of catalysts for chemical processes are the main topics in

this field. According to the basic chemistry concepts [3], the catalyst activity is defined as the rate of the catalyzed chemical reaction, while selectivity is evaluated as the probability that the catalyst lead to the formation of only one type of product when reaction may occur in parallel or along several reaction paths. The selectivity can also be qualified through the rate, R_i, of the reaction paths, relative to the summation over the different the reaction rates,

$$\mathrm{S} = \frac{R_i}{\sum_j R_j}. \tag{2.18}$$

For the case of ethylene epoxidation reaction, as mentioned in the introduction, the mechanism of the reaction involves multiple-steps that are associated with the reaction rates R_i's. Several computational studies have assumed that oxygen molecules (or atoms) chemisorption or formation of oxide structures on the catalyst surfaces are the elementary reation steps with the lowest R_i. These are therefore seen as the rate-controlling step. In contract, ethylene oxidation on these surfaces to form the final states, EO and Ac, is seen as the selectivity-controlling one [87, 44]. Through searching for the catalysts that are able to increase the rates of the former step, one can improve the catalysis activity in the ethylene epoxidation; on the other hand, the evaluation of rates of the EO and Ac formation steps allows us to estimate the selectivity of different catalysts (this can be seen in Eq.(2.18), and will be clarified later by expressing the selectivity of ethylene epoxidation in terms of reaction barriers). Therefore, a detailed study of the kinetic quantities (such as reaction barrier) of the reaction steps of ethylene epoxidation is also needed beside of DFT calculations for the stable structures.

Chemical reactions in heterogeneous catalysis are usually characterized by a series of thermally activated processes. The kinetic energy of initial states or final states on the reaction paths is mainly contributed by the thermal fluctuations around the local minima on the Potential Energy Surfaces that are associated with the stable configurations. Since at the temperatures used in heterogeneous catalysis kinetic energy of reaction is much smaller than the energy of the reaction barrier, at the atomistic time scales ($\delta\tau \lesssim 10^{-13}$ s), the possibility of overcoming reaction's energy barrier is very small. One calls such a problem as a rare event problem. The study of kinetic properties of such problem is treated by statistical approaches; and the so-called Transition State Theory (TST) is usually chosen for evaluating reaction rates of heterogeneous catalytic reactions [1].

Considering a general example of chemical reaction $nA + mB \rightarrow C + D$, the TST proposes that (i) the distribution of A and B reactants, and C and D products in an elementary path is given by the Maxwell-Boltzmann one, which ensures that at a given microscopic time-scale, the reactants and products will be relaxed and redistributed between their degrees of freedom before changing into the other state; (ii) for a given reaction path direction, the transformation goes through a transition state and, as a "moment decision", only the forward direction of reaction, with the TST rate constant $k_{\mathrm{TST}} = k_{\rightarrow}$, is available while the backward one is assumed to

be neglected, $k_{\leftarrow} = 0$. It means that the rate of the reactant consummation is

$$R = \frac{dN_{\mathrm{IS}}}{dt} = -k_{\mathrm{TST}} N_{\mathrm{IS}}. \tag{2.19}$$

Here, N_{IS} is the ensemble population of the initial state (IS) involving A and B reactants, while under the equilibrium condition, the TST rate constant, k_{TST}, represents the flux of configurations crossing the TS from the IS to the final state (FS).

In order to evaluate k_{TST}, TST states that k_{TST} is the product of the probability P_{TS} to find the system in the transition state times the rate, v_{TS} at which the system moves across the transition state once it gets there. The probability P_{TS} deals with the thermal fluctuation of atoms in the systems,

$$P_{\mathrm{TS}} =< \delta(r - r^{\dagger}) >_R \tag{2.20}$$

where $< \cdots >_R$ indicates an ensemble average over the reactants, and $\delta(r - r^{\dagger})$ specifies that system must be at transition state $r^{\dagger}$ to contribute to the average. For systems, such as solids, which are well described as harmonic oscillators around stationary points (minima and saddle points), the harmonic form of TST is often a very good approximation which can be used to evaluate P_{TS} .

$$P_{\mathrm{TS}} = \frac{\int_r e^{\kappa r^2/2kT} \delta(r - r^{\dagger}) dr}{\int_r e^{\kappa r^2/2kT} dr} = \frac{e^{-E^*/kT}}{\sqrt{2\pi kT/\kappa}} \tag{2.21}$$

where, κ in this expansion represents a spring constant of harmonic oscillation, which depends on the motion around the global minima of the IS atoms. $E^* = (E^{\mathrm{TS}} - E^{\mathrm{IS}})$ is the so-called activation energy or energy barrier. On the other hand, the average velocity of atoms at transition state can be calculated through the average momentum in phase space as,

$$< |v| >= \frac{< |p| >}{m} = \frac{1}{m} \frac{\int_p |p| e^{p^2/2mkT} dp}{\int_p e^{p^2/2mkT} dp} = \sqrt{\frac{2\pi kT}{m}}. \tag{2.22}$$

Therefore, the expansion of k_{TST} is established,

$$\begin{aligned} k_{\mathrm{TST}} =& \frac{1}{2} < |v| > P_{\mathrm{TS}} = \frac{1}{2} \sqrt{\frac{\kappa}{m}} e^{-E^*/kT} \\ =& \nu(\mathrm{IS}) e^{-E^*/kT}. \end{aligned} \tag{2.23}$$

The factor 1/2 here means that the system is moving only from reactants to products, and ν(IS) is seen as the oscillation frequency around the IS. Eq.(2.23) is equivalent to the van't Hoff-Arrhenius law [1], which states that the probability of rare event occurrence depends only on the IS properties and activation energy. From it, the rate constants of any given pathways can be estimated explicitly.

For the catalyzed ethylene epoxidation reaction considered in this thesis, the rates R_{EO} and R_{Ac} of the two competing parallel steps forming the final states EO

and Ac, respectively, are estimated by Eq.(2.19), while the selectivity of catalysts is calculated by Eq.(2.18). Beside considering TST, we make two assumptions that: (i) the IS of the two competing reaction pathways forming the final states EO and Ac are the same, which is either an ethylene physisorbed or a chemisorbed intermediate state; (ii) the prefactor, ν(IS), in Eq.(2.23) is similar for different catalyst surfaces. Combining Eqs.(2.19 and 2.23), then substituting into Eq.(2.18), the selectivity can be finally written as,

$$S = \frac{1}{[1 + e^{-(E^*_{\mathrm{Ac}} - E^*_{\mathrm{EO}})/kT}]}, \tag{2.24}$$

where E^*_{Ac} and E^*_{EO} are the activation energies for the Ac and EO synthesis steps, respectively. Through Eq.(2.24), the selectivity in ethylene epoxidation is determined by the $\Delta E^* = E^*_{\mathrm{Ac}} - E^*_{\mathrm{EO}}$, which shows that the more positive is ΔE^*, the higher is the selectivity toward EO formation.

2.2.3 Computational Methods to Estimate Chemical Reaction Paths

In the previous sections, one has seen that the activation energy of the reaction paths is a quantity of central importance for estimating the selectivity of catalysts and transition rates of chemical reactions, according to the van't Hoff-Arrhenius law, within harmonic TST. The activation energy is defined by the difference between the energy of the Transition State (TS) and the Initial State (IS).

In principle, the IS on the reaction path, and similarly for the Final State (FS), are identified as local minima located on the Potential Energy Surfaces (PES), and are normally evaluated by minimizing the total energy and the internal forces corresponding to the most stable configurations. In this thesis, we have used Broyden-Fletcher-Goldfard-Shanno (BFGS) algorithms to do this optimization.

On the other hand, finding for TS needs more efforts. First of all, a specific algorithm should be used to find the Minimum Energy Path (MEP) of the reaction paths on the multi-dimensional configuration space PES. The MEP is defined as the specific path that connects two local minimum points corresponding to IS and FS, and is characterized by the property that the perpendicular forces on this paths are vanishing:

$$F_\perp = F - \hat{\tau}[\hat{\tau}.F] = 0, \tag{2.25}$$

where $\hat{\tau}$ is the vector tangent to the path, and $F = -\nabla V$ with V the potential in the PES. After establishing MEP, the saddle point with the highest energy on the reaction path is located as the TS that we are looking for.

The method that is most widely used for finding TS in plane-wave DFT calculations is the nudged elastic band (NEB) method [88]. This method was developed by Hannes J. Jönsson and co-workers as a refinement of earlier "chain-of-states" methods [89]. The primary aim of this technique is to define MEP, between two local minima by constructing a number of intermediate configurations, called "images" between the IS and FS. The total energy of each image is then optimized while keeping the distance between consecutive images constant, meaning that the path

can be elongated or shorten, but the images will remain approximately equispaced. In order to warranty this constraint, spring forces will be introduced for each images (this is referred as the elastic band method). In the NEB method, minimization of the elastic band is carried out where the perpendicular component of the spring forces and the parallel component of the force induced by the external potentials are excluded. The force on image i then becomes

$$F(x_i) = \{-\nabla V(x_i) + \hat{\tau}_i[\hat{\tau}_i \nabla V(x_i)]\} - k[(2x_i - x_{i+1} - x_{i-1})\hat{\tau}_i]\hat{\tau}_i, \tag{2.26}$$

where k is the elastic force constant of the virtual springs. In Eq.(2.26), the first contribution is the force perpendicular to the path, which is due to the external potential and is calculated by DFT with respect to the intermediate image geometries. The second term is the spring force contribution that is projected onto the parallel direction at each image. The idea of projecting the spring forces is call nudging of the elastic band [89].

Moreover, because the elastic forces act exclusively along the MEP, one is free to choose values of spring elastic constants that are different between pairs of images. The values of k are usually chosen so that there are stronger for images closer to TS. This results in a higher number of images closer to TS, and one thus can have a better description of the path around this point. This method is called variable elastic constants NEB [89].

While the NEB method gives a discrete representation of the MEP, the energy of the saddle point needs to be obtained by interpolation. When the energy barrier is narrow compared with the length of the MEP, few images land in the neighborhood of the saddle point and the interpolation can be inaccurate. The climbing image NEB (CI-NEB) method constitutes a small modification to the NEB method. Information about the shape of the MEP is retained, but a rigorous convergence to a saddle point is also obtained. This additional feature does not add any significant computational effort. After a few iterations with the regular NEB, the image with the highest energy $imax$ is identified. The force on this one image is not given by Eq.(2.26) but rather by

$$F_{x_{imax}} = -\nabla V(x_{imax}) + 2\hat{\tau}_{imax}[\hat{\tau}_{imax} \nabla V(x_{imax})] \tag{2.27}$$

where, one can easily recognize that the spring force component parallel to the path is removed at the highest image. The last component that is parallel to the path will shift up the maximum image toward the TS, while the geometry is still optimized [88].

The relaxation of the intermediate images along the path simultaneously converges them toward the MEP. The convergence of the path is characterized by a decrease of forces on the images, that are calculated by Eq.(2.26), until they are smaller than a threshold value. Here, one should note that the relaxation procedure of each image is similar to the relaxation used in finding the local minimum geometry. The NEB algorithm is already implemented in the Quantum ESPRESSO distribution, with a very high level of parallelization [90].

2.3 Results and Discussion

In heterogeneous catalysis, surfaces of solid particles act as catalysts. The identification of the composition and geometry of the catalyst's surface and the determination of the various chemical reactions that take place under realistic conditions are the main prerequisites for reaching a microscopic understanding of heterogeneous catalysis. Surface science techniques [3] usually operate under ultra-high vacuum (UHV) conditions ($10^{-13} - 10^{-9}$ atm) and low temperature (room temperature or even below) where the behavior of catalyst may be different compared with high pressure ($\sim$ 1 atm) and temperature (often higher than 300 K) regime, where the catalysts typically operate. In addition, structural properties such as composition and geometry measured under thermodynamic equilibrium conditions may be different to those under realistic non-equilibrium conditions, where there is a flux of incoming reagents and outgoing products, and various dynamical phenomena such as bond-making and bond-breaking between reactants and the surfaces occur simultaneously. These differences may lead to inconsistencies between the properties of catalysts measured in typical UHV surface science experiments and those of the real catalyst under operating conditions.

Recent experimental and theoretical works have shown that working catalysts can be thought as "living objects". In some cases, it has been found that the surface of catalysts can consist of a number of possible structures with similar energetics rather than a single low energy one. These structures during catalytic operation can evolve with respect to time or transform between those having similar energy. This picture emerged, for example, in recent studies of CO oxidation on $RuO_2(110)$ and Pd(100), where the highest catalytic activity is reached in regions of the phase diagram corresponding to the boundaries between different stable surface oxide structures [91, 5]. STM measurements of the CO oxidation, under steady-state catalysis, have shown the formation of oxide-layer structures on the Pd(100) and Pt(110) catalysts, and these structures are evolving continuously in time [91, 5]. Similarly, on Ag(111) surfaces, the coexistence of different surface oxide structures is also found by STM experiments performed under conditions relevant to oxidation catalysis [92]. These experiments therefore suggest that to study oxidation reactions such as ethylene epoxidation on catalyst surfaces, one needs to carefully examine the role of high pressure and temperature on the structural properties of the catalyst surfaces.

In atomistic simulations, this problem has been considered by combining accurate first-principle methods and equilibrium and non-equilibrium statistical mechanics techniques [5]. In the first-principle methods, the combination of DFT and ab initio thermodynamics methods can yield a successful prediction for stability of several structures on the catalyst surfaces. On the other hand, employing the Kinetic Monte-Carlo approach, one can simulate a coarse-grained dynamics of the full steady-state catalysis. Nevertheless, a detailed description of the complete set of elementary heterogeneous catalysis processes is needed to set up an *ab initio* Kinetic Monte Carlo, usually involving very expensive calculations. In this thesis, we will limit ourselves to study of heterogeneous catalysis of ethylene epoxidation on

Ag-Cu catalyst structures under the thermodynamic equilibrium conditions.

As mentioned in the section 2.1.2, experiments of ethylene epoxidation on the Ag-Cu catalysts were carried out under the steady-state conditions by Piccinin and co-workers [77]. The authors have identified the formation of a thin oxide CuO structures on Ag-Cu surfaces in the reactive environments. This result has been confirmed using DFT calculations. Cu was found to segregate to the surface showing tendency to form a copper oxide-like layer structure due to the relative bond strength of Cu-O and Ag-O in presence of oxygen. Furthermore, the most stable structures formed by the oxide-like layer on low-index facets of Ag-Cu are also examined in thermodynamic equilibrium conditions. In this study, the surface free energy of several surface structures as function of temperature and partial pressure of oxygen has been studied, where the presence of ethylene has been neglected. The results have suggested that in the regions relevant for ethylene epoxidation reaction, i.e. $T = 600$ K and $p_{O_2} = 1$atm, depending on the copper content, clean Ag, or copper oxide-like structures can coexist on Ag-Cu surfaces. In contrast, the two-dimensional (2D) structures of Ag-Cu alloy that have been assumed as catalyst surfaces in the DFT calculations for ethylene epoxidation in Refs. [72, 53, 93] are not stable on these low-index facets. In Fig. 2.6, we show the geometry of the most stable structures on the three low-index facets, associated to those investigated in Refs. [79, 78].

On the (111) surface, three kinds of Ag-Cu structures have been examined. They consist of Ag slabs covered with a thin layer of either Cu_2O-like structure or CuO-like structures. The first one is labeled P4-OCu3/Ag(111) that is a (4×4) periodic structure with ring-like O-Cu patterns and one OCu3 unit removed. O atoms in this structure are coordinated to three Cu atoms and Cu atoms are coordinated to two O atoms, except around the missing unit, where the O coordination is reduced to two. A similar structure is also found for the second one that is, however, characterized by a (2×2) periodicity. This structure is label P2/Ag(111). These two Cu_2O-like configurations have an average energy per oxygen atom of 1.41 and 1.37 eV, respectively, and their Cu-O bond length are between $1.84 - 1.85$ Å. The third structure is built from (2×2) periodic structures of the CuO-like thin layer including defective ones. When present on the phase diagrams, the CuO/Ag(111) structure, given in Fig. 2.6, is shown as the most stable one on the regime relevant to experimental conditions. In this structure, O is coordinated to three Cu atoms and Cu is coordinated to either two or four oxygen atoms, and the Cu-O distances are between 1.82 and 1.95 Å. The average binding energy per oxygen in this structure is 1.16 eV [79]. On the (100) surface, Cu and O on this structure are 4-fold coordinated with a Cu-O distance of 2.08 Å. For the (110) surface, on the other hand, Cu and O are 2-fold coordinated, with Cu occupying "added row" positions on the underlying Ag surface. The Cu-O distance is, in this case, 1.81 Å. On both these facets, the stable structure formed by CuO-like layer have (4×4) periodic structure, and they are labeled as CuO/Ag(100) and CuO/Ag(110), respectively [78]. According to the experimental and theoretical results, it is suggested that the structures formed by thin copper oxide layer on the surfaces of Ag-Cu catalysts are very important under operating conditions. In modeling ethylene epoxidation on the Ag-Cu catalysts, the

stable structures introduced above will be considered as the most relevant catalysts under real catalytic conditions.

In the next sections, we will examine the relative stability of the catalyst surface structures in presence of both oxygen and ethylene reactants. In this case, the interactions between ethylene molecule and oxygen atoms in the oxide layers can supply more accurate information about the thermodynamic stability of the structures present on the catalyst surfaces in ethylene epoxidation. The possible mechanisms the reactions for the formation of EO and Ac on the stable structures are also examined. Our results provide evidence of the role of Cu in promoting the selectivity toward the formation of EO, compared to the case of the pure Ag. In addition, we also study for the effects of sub-surface oxygen, O^{sub}, and Cu compositions on catalytic properties of these oxide-like layer surfaces. On the other hand, it is also worth noting that since the catalyst structures considered in this work are assumed as the stable ones under thermodynamic equilibrium conditions, our theoretical analysis only approximately describe the structure of the catalyst under operating conditions. However, this study can give useful guidelines for understanding the possible catalytic reactions occurring on a set of phase structures that could be relevant under catalytic conditions.

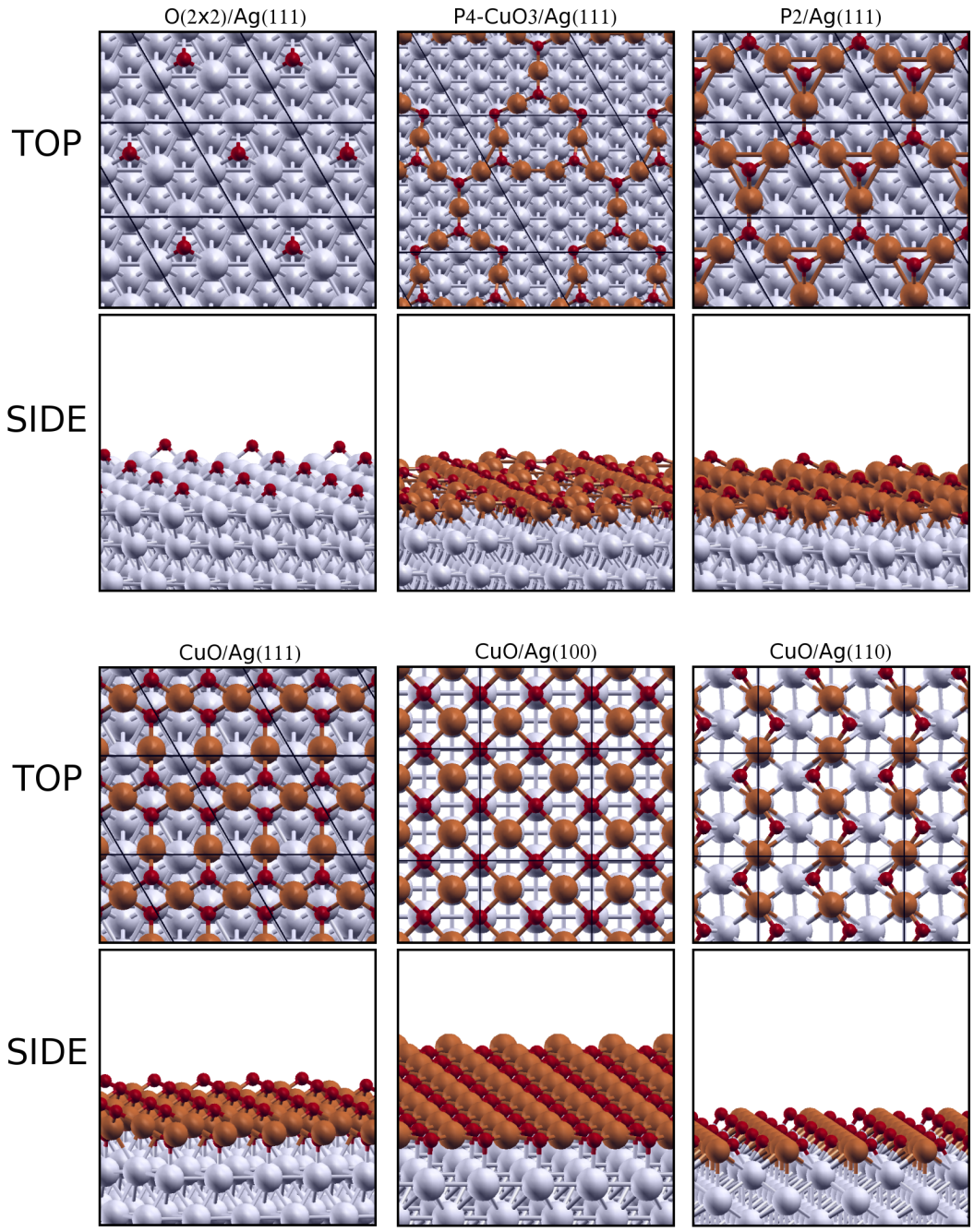

Figure 2.6: Top and side view of the six low energy structures on three low-indexed (111), (100) and (110) surfaces. The small red (black) atoms represent oxygen, the larger brown (light black) ones represent copper, the grey (light grey) ones represent silver.

Table 2.2: Adsorption energy (in eV) of the most stable physisorbed and chemisorbed ethylene configurations on Ag-Cu alloy surfaces. The last column shows the formation energy per oxygen atom (in eV) of the thin oxide-like surface layers.

Surface	C_2H_4	OMC	EDO	E_O^f
P2/Ag(111)	−0.07	0.86	−0.36	−0.97
CuO/Ag(111)	−0.10	0.33	−0.71	−1.06
CuO/Ag(100)	−0.08	0.53	−0.63	−1.09
CuO/Ag(110)	−0.04	−0.12	−1.01	−1.28

2.3.1 Stability of intermediate states formed on Ag-Cu alloy

In the previous section, we have introduced the stable surface structures of Ag-Cu likely to be present in an oxygen atmosphere for the three low-index surface orientations as a function of oxygen chemical potential (i.e. T and p_{O_2}). However, in real conditions of ethylene epoxidation reaction, not only oxygen but also ethylene is present, which acts as the reducing agent. In this study, the adsorption of the reactants on the stable surface structures will be considered. The stability of intermediates will be estimated for different temperature and pressure conditions. Construction of the phase diagram allows to obtain the lowest free energy phase structures that may be found on the Ag-Cu particle facets under conditions of temperature and pressure relevant for experiments. In particular, we will also investigate the shape of the catalyst particles as a function of the copper loading and temperature. Details of the computational setup for the calculations are presented in Appendix A.

2.3.1.1 Adsorption of Ethylene on Ag-Cu alloy surfaces in Reactive Environment

Ethylene physisorption on oxygen pre-covered Ag-Cu alloy surfaces The adsorption of the reactants on the catalyst surface is the first step of the mechanism of ethylene epoxidation that has been proposed on monometallic as well as on alloy catalysts [94, 53]. Several theoretical studies, therefore, have examined adsorption of ethylene on both the clean and oxygen pre-covered Ag and Cu surfaces. For example, A. Kokalj *et al.* [95] found that ethylene adsorbes weakly (~ -0.1 eV) on the clean Ag surfaces. It has been also shown that the adsorption of ethylene is strongly promoted by the presence of sub-surface oxygen, [95] Ag adatoms [96] as well as by positively charged Ag sites in Ag-oxide covered Ag(111) [75]. Analogously, the studies of ethylene adsorption on clean Cu surfaces show a similarly small binding energy in the $\theta_O = 1/16 - 1/4$ ML coverage range.

In the case of Ag-Cu alloy in an oxygen environment, several surface structures with similar energetics have been predicted to form on the low index surfaces of this material. Here we will focus on the two most stable structures with a (2×2)

periodicity of the (111) facet labeled "P2" and "CuO", and on the "CuO" structures on the (100) and (110) facets [79, 78]. In Fig. 2.7(a-d), we show the relaxed adsorption geometries of ethylene on these four surface structures.

The ethylene adsorption energy on different surfaces is shown in Table 2.5. Its value is given by:

$$E^{\mathrm{b}} = E_{\mathrm{tot}} - [E_{\mathrm{surf.}} + E^{\mathrm{gas}}_{\mathrm{C_2H_4}}], \tag{2.28}$$

where E_{tot} and $E_{\mathrm{surf.}}$ are the total energy of the surfaces with and without the presence of ethylene molecules, respectively. $E^{\mathrm{gas}}_{\mathrm{C_2H_4}}$, on the other hand, is the energy of the isolated ethylene molecule in the gas phase. We can see that this quantity is almost unchanged on different orientations of Ag-Cu catalyst surfaces and comparable with that obtained in pure Ag and Cu. Consistently, we find that the geometry of adsorbed ethylene is unchanged with respect to the gas phase. The C-C length, for example, is in all cases 1.33 Å.

In Fig. 2.7(a-d) we also show the contour plot of the induced charge density, defined as $\Delta n(r) = n_{\mathrm{tot}} - [n_{\mathrm{C_2H_4}} + n_{\mathrm{surface}}]$, i.e. the difference between the charge density of the adsorption system and the sum of the isolated ethylene and catalyst surface. This shows that there is no net charge transfer between ethylene and the surface, and also indicates the lack of formation of any covalent interaction between ethylene and the surface, in agreement with the small adsorption energies predicted by our calculations.

Here we point out that GGA functionals, however, do not provide a correct description of dispersion (i.e. van der Waals) interactions, which are an essential component of physisorption. The computed adsorption energies are therefore likely underestimated (in absolute value).

Formation of the oxametallacycle Since OMC has been found to be a common intermediate for both the selective and unselective paths on pure Ag(111) [94], we now investigate the stability of this configuration on the thin oxide-like layers that we predicted to be present in an oxidizing atmosphere. In Fig. 2.7(e-h), we display, for each of the four thin oxide-like layers considered in this work, the most stable OMC structure. The ethylene fragment in OMC can be seen as a di-σ bonded ethylene with the first carbon atom linked to copper and with the second one bound to oxygen. Ethylene undergoes a change from sp^2 to sp^3 hybridization during the formation of OMC, which is evident from a reduction of the trans H-C-C-H dihedral angle and an elongation of the C-C bond. The former reduces from 180° in gas-phase ethylene to values ranging from 137° to 168°, depending on the surface orientation. These values are higher than those on the low oxygen-covered surfaces of pure Cu (108°) or Ag (116°−120°) catalysts [97, 54]. The C-C distances on the OMC configurations (1.48−1.49 Å) are elongated relative to the gas phase (1.33 Å), and are slightly smaller than those found for OMC on pure Ag (1.50 Å) and Cu (1.518 Å).

In Table 2.5 we show the adsorption energy of OMC relative to ethylene in the gas phase. We can see that the formation of OMC is exothermic only on the CuO/Ag(110) surface, while on the other three surface structures considered here

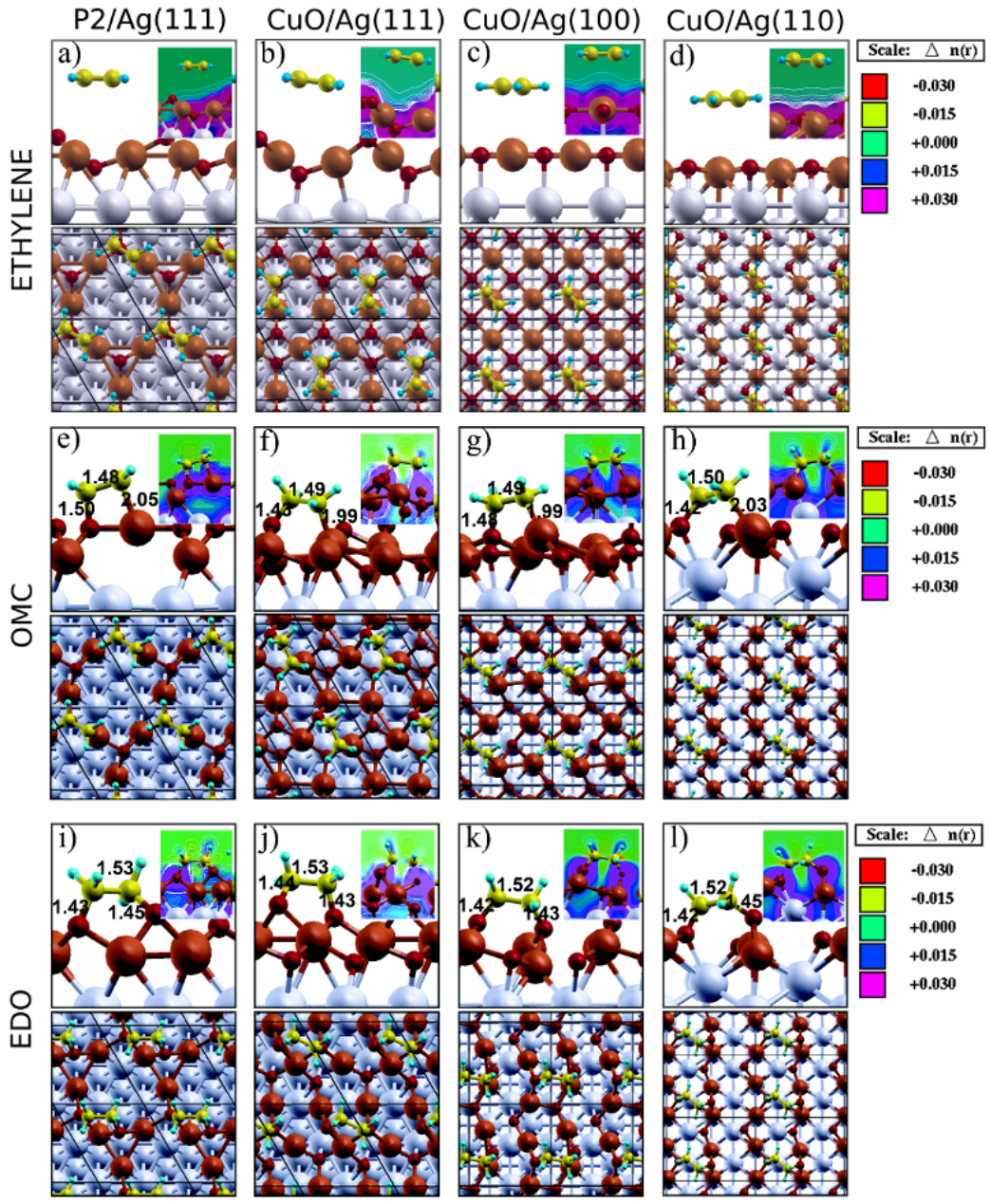

Figure 2.7: Top and side view of physisorbed ethylene (a-d), chemisorbed ethylene for OMC configuration (e-h) and for EDO configuration (i-l) on the low energy structures considered in this work: P2 on the (111) surface and 1 layer of CuO on the (111), (100) and (110) surfaces. The small red (black) atoms represent oxygen, the larger brown (dark-grey) ones represent copper, the larger grey (light-grey) ones represent silver, the minimum yellow (grey) ones represent carbon, and the small green (grey) ones represent H. The insets show charger density difference for considered structures. Contours are drawn in linear scale from -0.03 to 0.03 e/Å^3 with the increment of 0.015 e/Å^3. The charge flows from red to blue region.

the formation of this intermediate is not energetically favorable. We found that the OMC adsorption energy correlates with the formation energy per oxygen atom of these oxide layers (last column in Table 2.5). This suggests that the stability of the oxygen atoms in the oxide layers is the key factor in determining the energetics of OMC formation.

In Fig. 2.8(a) we show the energy profile of the OMC formation reaction, starting from the physisorbed ethylene configuration. We find that the activation energy, E^*, for the formation of OMC on the CuO/Ag(110) is only 0.5 eV, whereas on (111) and (100) surfaces $E^* = 1.02$ eV and 0.89 eV, respectively. For the P2 structure on the (111) surface we find an even higher value, $E^* = 1.22$ eV. From Fig. 2.8(a) we can see that the lowest activation energy corresponds to the most exothermic reaction, while the highest corresponds to the most endothermic, in agreement with the Brønsted-Evans-Polanyi relation that predicts a linear relationship between activation energy and reaction enthalpy [80, 81]. We note, though, that this relation does not hold for the CuO/Ag(111) and CuO/Ag(100) structures, however these two systems have similar energetics.

Formation of the ethylenedioxy Another candidate intermediate in the ethylene epoxidation reaction is ethylenedioxy (EDO), where each of the two carbons in ethylene is bound to a chemisorbed oxygen atom. This structure and its single carbon analogous, dioxymethylene, have been observed experimentally through Temperature Programmed Desorption (TPD) during ethylene glycol decomposition on the surface of a silver catalyst and through Fourier Transform Infrared (FTIR) spectroscopy and chemical trapping on the surface of a copper supported on zinc aluminate upon adsorption of formaldehyde [98, 99, 100].

First-principles simulations have shown that on pure Ag surfaces EDO is formed when the oxygen coverage is increased to 1/2 ML [58]. Since the thin oxide layers we are considering here have a high oxygen content, EDO represents a likely intermediate also for these systems. In Table 2.5 we show the adsorption energy of EDO relative to gas phase ethylene. Clearly this intermediate is considerably more stable than both physisorbed ethylene and OMC. We note however that the adsorption energies reported in Table 2.5 are zero-temperature values, while the effects of temperature and pressure will be analyzed in detail in section 2.3.1.2.

In Fig. 2.7(i-l), we show the relaxed adsorption geometries for EDO. The C-C distances in the EDO on four surface structures are elongated compared to gas phase ethylene also compared to OMC. The trans H-C-C-H dihedral angles are strongly reduced with respect to the planar structure of ethylene. The dihedral angles are of 62°, 75°, 62°, and 48° for EDO on P2, CuO on (111), and CuO on (100) and (110), respectively. The induced charge density displayed in the insets of Fig. 2.7(i-l) shows a large perturbation around the oxygen atoms, indicating the formation of strong C-O-metal bonds.

In Fig. 2.8(b) we show the reaction profile for the formation of EDO staring from physisorbed ethylene. The activation energies exceed, on all surface structures, 1.0

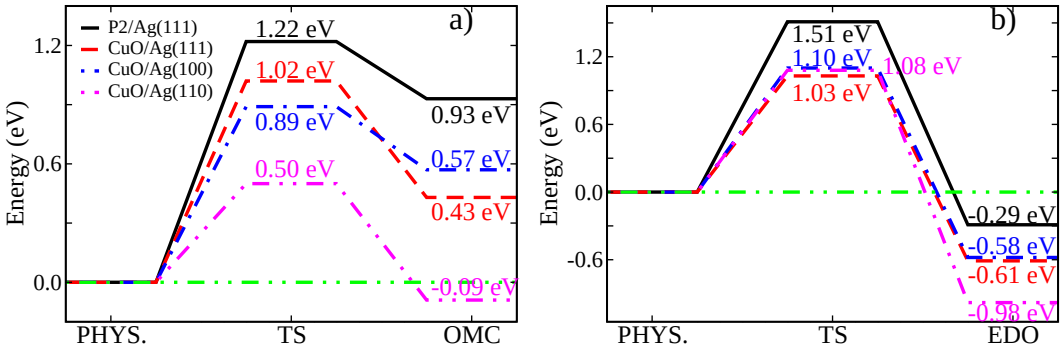

Figure 2.8: Reaction profiles for the formation of OMC (a) and EDO (b) on the most stable Ag-Cu alloy surfaces. The zero level is the energy of physisorbed ethylene on P2 and CuO structures at different surface orientations.

eV, suggesting that the formation of this stable intermediate might be kinetically hindered. We anticipate here that the activation energy to form either EO or AC starting from EDO is considerably higher than starting from other intermediates, indicating that the formation of EDO would poison the catalyst surface. As we will see in section 2.3.1.2, EDO is predicted to be found at the surface of the alloy catalysts only at high ethylene partial pressure. This could be a possible explanation for the experimental observation that the activity of the catalyst is reduced as the ethylene partial pressure is increased [74].

2.3.1.2 Thermodynamic diagrams of Ag-Cu alloy in Reactive Environment

Having established the relevant low energy structures formed by oxygen and ethylene on Ag-Cu alloy surfaces, we now turn to the surface phase diagrams of the (111), (100), and (110) surfaces. The key quantity is the surface free energy calculated as a function of chemical potentials of O and C_2H_4, as follows:

$$\gamma(T,p) = \frac{1}{A}\left[E^{\text{total}} - E^{\text{slab}}_{\text{Ag}} - \Delta N_{\text{Ag}}\mu_{\text{Ag}} - \Delta N_{\text{Cu}}\mu_{\text{Cu}} - N_{\text{O}}\mu_{\text{O}}(T,p) - N_{\text{C}_2\text{H}_4}\mu_{\text{C}_2\text{H}_4}(T,p)\right], \tag{2.29}$$

where, $E^{\text{slab}}_{\text{Ag}}$ and $E^{\text{slab}}_{\text{Ag}}$ are the total energies of the total system (comprising ethylene and/or oxygen adsorbed on the Ag-Cu alloy surfaces) and the clean Ag surface, respectively. ΔN_{Ag} is the number of Ag atoms in addition to the ones contained in the slab, $N_{\text{Cu}}, N_{\text{O}}$, and $N_{\text{C}_2\text{H}_4}$ are number of Cu, O atoms and Ethylene molecules, μ_{Ag}, μ_{Cu}, μ_{O}, and $\mu_{\text{C}_2\text{H}_4}$ are the chemical potential of Ag, Cu, O and Ethylene, respectively. With this definition, the most stable structures are identified as the ones that minimize the surface free energy for particular value of $\Delta\mu_{\text{O}}$ and $\Delta\mu_{\text{C}_2\text{H}_4}$.

In Ref. [77], Piccinin *et al.* considered the stability of thin oxide-like layers in the presence of the reducing agent (ethylene), while neglecting the possibility of physisorbed or chemisorbed ethylene (which, as we show below, is correct for values

of temperature and oxygen/ethylene pressure used experimentally). They showed that, in agreement with experimental findings, the oxidation of ethylene to either EO or AC does not reduce the oxide layers to metallic copper. Here we extend this study by explicitly considering physisorbed and chemisorbed ethylene structures on these layers and studying their relative stability as a function of temperature and partial pressure of both oxygen and ethylene.

In this section we consider the surface free energy of adsorption of the ethylene structures (OMC and EDO) on clean Ag, the thin oxide-like CuO/Ag and P2/Ag, and their subsurface oxygen structures, on the (111), (100) and (110) surfaces. In total we have studied 47 different surface structures. Projecting the lowest surface energies on the $(\Delta\mu_{\mathrm{O}}, \Delta\mu_{\mathrm{C_2H_4}})$ plane, we obtain the surface phase diagrams of the thermodynamically most stable configurations (Fig. 2.9). In these graphs we also report, for three values of temperature (300, 500 and 600 K), the values of partial pressure for oxygen and ethylene corresponding to the chemical potentials shown on the axis.

Analyzing these phase diagrams we note that, as expected, at low values of ethylene chemical potential (i.e. low ethylene partial pressure or high temperature) the stable structures do not contain ethylene. In these regime we therefore recover the phase diagram of the O/Ag/Cu system already investigated in previous publications. [79, 78] As the value of the ethylene chemical potential is raised, the first ethylene-containing structures that appear in the phase diagram contain EDO, on all three facets. This reflects the stability of EDO intermediates already highlighted in Table 2.5.

Physisorbed ethylene is found to be stable only at high ethylene and low oxygen chemical potentials, and only on pure Ag surfaces, on all three facets. This can be understood since at low values of $\Delta\mu_{\mathrm{O}}$ the formation of oxygen-containing EDO and oxide-like structures is disfavored. Of particular interest are the thermodynamic conditions close to the experimental values of temperature and partial pressures used in real catalysis. These roughly correspond to $T = 500 - 600$ K and pressures in the range of a few atm [101]. In Fig. 2.9 we show with a dashed polygon the area corresponding to $T = 300 - 600$ K and pressures in the $10^{-4} - 10^{0}$ atm range. The conditions that more closely resemble the surface science experimental setups are found on the lower-left corner of the polygon, while industrial conditions correspond to the central region of the polygon. We can see that around this point, on all three facets, we find the CuO/Ag structure, while at lower temperature and higher pressure end of the polygon we find EDO chemisorbed on the thin oxide-like CuO/Ag of (100) and (110) surfaces, and on the subsurface oxygen structure of the thin oxide-like CuO/Ag of (111) surface. We recall here that EDO has been predicted to be present also in the phase diagram of pure Ag(111) under conditions of temperature and partial pressures compatible with those used experimentally [58]. We have shown in an earlier work [102] that once EDO is formed, the kinetic barrier toward the formation of the final products is very high (1.84 eV in the case of the P2/Ag(111)). This intermediate would therefore poison the catalyst surface. Fixing the partial pressures of both oxygen and ethylene to 1 atm, our calculations predict

that this intermediate would be present on the CuO/Ag(110) surface below 480 K, on the CuO/Ag(100) surface below 323 K, on the subsurface oxygen structure of CuO/Ag(111) surface below 475 K, and on the P2/Ag(111) surface below 208 K.

As already mentioned earlier, OMC has been experimentally found to be a common intermediate for the conversion of ethylene to both EO and AC [94, 103]. It is therefore important to stress that our calculations predict that this intermediate is not the most stable structure under any value of chemical potential of ethylene and oxygen. It has been argued that the presence of OMC intermediate on pure Ag surfaces might be stabilized at high oxygen chemical potential in the presence of sub-surface oxygen [58]. To test this possibility we considered the presence of sub-surface oxygen and verified that, even in this case, OMC is not present in the phase diagram.

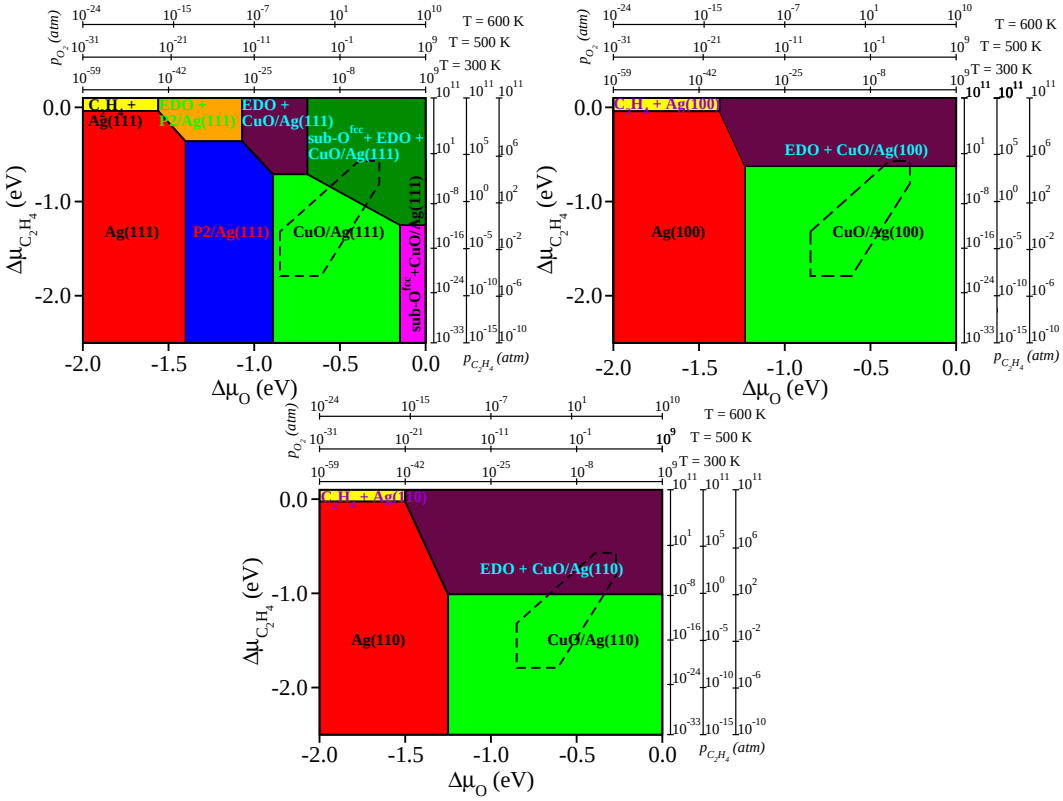

Figure 2.9: Surface phase diagrams of stable structures on Ag-Cu alloy surfaces in equilibrium with oxygen and ethylene environments, as a function of $\Delta\mu_{\mathrm{O}}$ and $\Delta\mu_{\mathrm{C_2H_4}}$ in the gas phase. The additional axes show the corresponding pressure scales at $T = 300$, 500, and 600 K.

2.3.1.3 Geometry of Ag-Cu alloy catalysis particles as known Cu surface content

Recently, experiments have showed that the catalytic selectivity in ethylene epoxidation on alumina-supported silver catalysts depends on both reaction conditions and geometric structure of catalytically active Ag particles [104]. Indeed, the selectivity to EO on Ag nanowire catalysts is much higher than that on conventional Ag particles with similar external conditions. The enhanced EO selectivity of the nanowire catalysts is attributed by higher concentration of the Ag(100) surface facets on nanowire in comparison to Ag particles [104, 105, 106, 107]. Density functional theory calculations also showed that the Ag(100) surface facet is inherently more selective toward EO than the Ag(111) [94, 108]. It is therefore important to study how the shape of the particles depends on the ambient conditions and on the copper content. To this end we use the Wulff construction to predict the shape of the particle that minimizes its total surface free energy. We fix the value of the chemical potentials of both ethylene and oxygen corresponding to partial pressures $p_{O_2} = p_{C_2H_4} = 1$ atm, and to three values of temperature, $T = 300$, 500 and 600 K. The chemical potential of Cu measured relative to its bulk value, $\Delta\mu_{Cu}$, will be used as a parameter that controls the amount of Cu in the particle. Low values of $\Delta\mu_{Cu}$ correspond to Cu-lean conditions, while high values correspond to Cu-rich conditions. In Fig. 2.10 the vertical dashed lines represent the Cu chemical potential above which Cu oxidizes to bulk copper oxide, which, as one can show, corresponds to the computed heat of formation of bulk copper oxide at the fixed value of oxygen chemical potential. In Fig. 2.10 we show, for three values of temperature, the surface free energy of the most stable structure found on each of the three facets as a function of $\Delta\mu_{Cu}$. For selected values of $\Delta\mu_{Cu}$ we plot the shape of the particle predicted through the Wulff construction. Since experimentally the Cu surface content is found to be in the $0.1 - 0.75$ ML range [72, 74], the values of $\Delta\mu_{Cu}$ compatible with these findings are those when some of the facets start being covered by thin copper oxide-like layers. We can see the values of $\Delta\mu_{Cu}$ for which this happens is not far from the bulk copper oxide formation boundary. Taking into consideration our computational error-bars and kinetic effects we can therefore expect some competition between bulk copper oxide and CuO/Ag surface formation, reflecting the fact that the formation energy of the thin layers is similar to their bulk counterpart. Examining the surface free energy plots in Fig. 2.10 at $T = 600$ K we can see that, as $\Delta\mu_{Cu}$ is increased, the first facet to be covered by the thin layers is the (110), while as soon as all the facets are oxidized the lowest energy surface is the (100). This is particularly relevant since in pure Ag the lowest energy surface is the (111), while the most selective is the (100). Our calculations show that the inclusion of copper has the effect of lowering the surface free energy of the (100) facet relative to the other low-index facets, and we therefore predict that Cu-containing catalyst particles should expose a larger fraction of (100) area compared to pure Ag. This effect is, on the other hand, reversed at lower temperature. Looking at the $T = 300$ K case in Fig. 2.10 we can see that as soon as all facets are covered by thin oxide

layers, the (100) facet is not dominant. In this case all facets are covered by EDO chemisorbed on CuO/Ag and, as reported in Table 2.5, EDO binds more strongly to the (110) and (111) surface compared to the (100) one, therefore lowering their surface free energy relative to the (100).

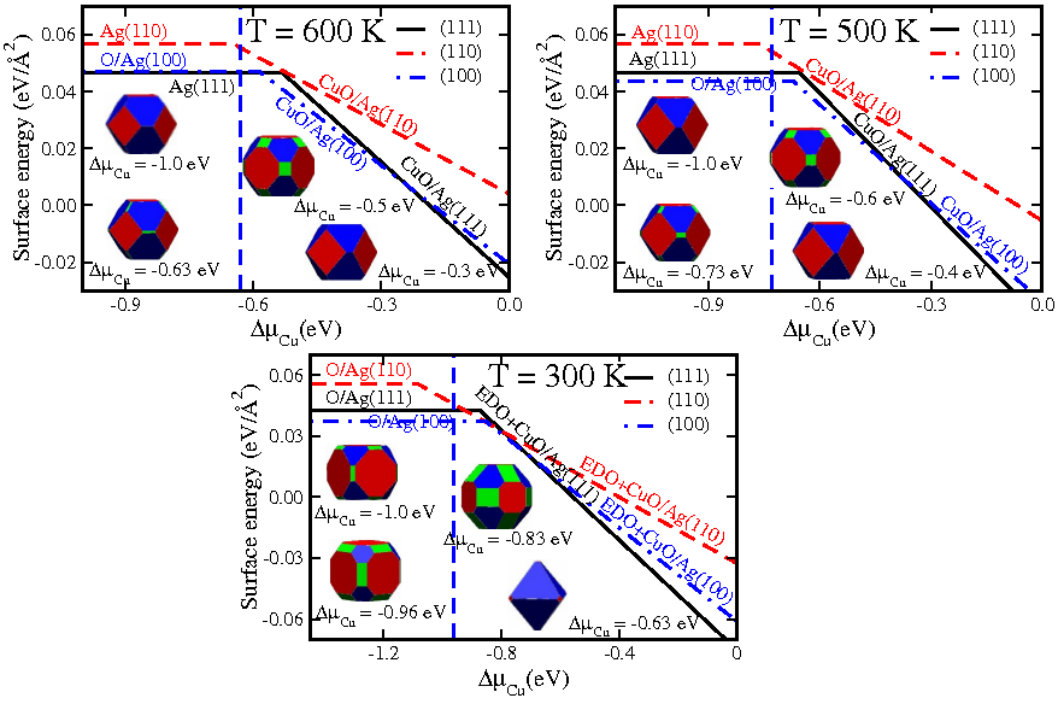

Figure 2.10: Surface free energies of the most stable surface structures on each of three surface orientations as a function of the Cu chemical potential. At selected Cu chemical potentials, also a model of a catalyst particle obtained through the Wulff construction is presented. $\Delta\mu_{\mathrm{O}}$ and $\Delta\mu_{\mathrm{C_2H_4}}$ are set to the values corresponding to $T = 300$, $T = 500$ and $T = 600$ K, and $p_{\mathrm{O_2}} = p_{\mathrm{C_2H_4}} = 1$ atm.

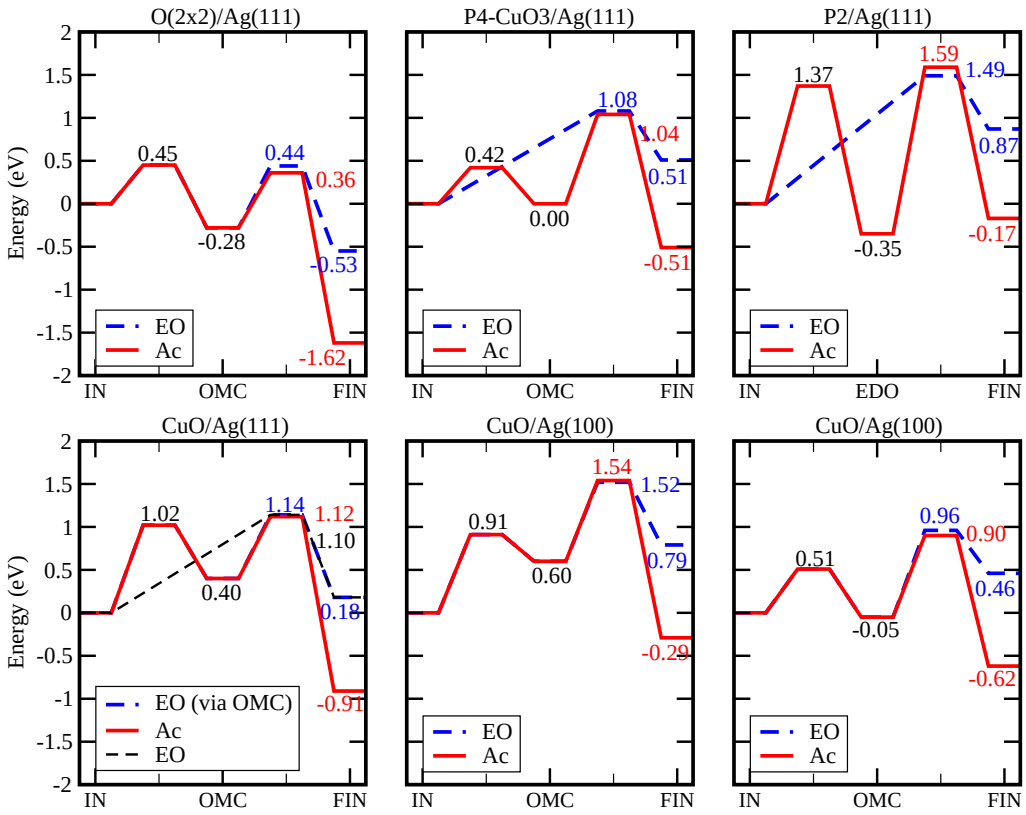

Figure 2.11: Energy profiles for ethylene epoxidation over selected surface structures. At the initial state (IN) ethylene is physisorbed on the surface, the intermediate state is the oxametallacycle, while at the final state (FIN) the reaction has either produced acetaldehyde (Ac, black solid line) or ethylene oxide (EO, red dashed line). The energies of the final states correspond to the products physisorbed on the surface. The reaction can process through the formation of intermediates such as the oxametallacycle (OMC) or ethylenedioxy (EDO). The zero of energy is set at the initial state.

2.3.2 Mechanism of Ethylene Epoxidation catalyzed on Ag-Cu Alloy

In this section, we will present the study of the mechanism of ethylene epoxidation catalyzed by the thin oxide layers that are predicted and found to be present at the surface of Ag-Cu alloy under operating conditions. We consider the adsorption of ethylene and the two competing chemical reactions leading to the formation of Ac and EO. On the clean Ag surfaces, the ethylene molecule is known to bind very weakly, as on thin Ag oxide-like layers [96, 75]. Here, as well, we find that the adsorption energy of ethylene, defined in Eq.(2.28), never exceeds 0.15 eV on any of the surface structures considered. The location of the transition state (TS)

Table 2.3: Cu surface content (Θ_{Cu}), activation barriers for the formation of acetaldehyde (E^*_{Ac}) and ethylene oxide (E^*_{EO}) and the difference between the two (ΔE^*) for selected surface structures, the reaction enthalpies for the formation acetaldehyde ΔH_{Ac}, and ethylene oxide ΔH_{EO}.

Structure	Θ_{Cu}(ML)	ΔE^*(eV)	E^*_{Ac}(eV)	E^*_{EO}(eV)	ΔH_{Ac}	ΔH_{EO}
O(2 × 2)/Ag(111)	0.00	-0.08	0.64	0.72	-1.34	-0.27
P4-OCu3/(111)	0.56	-0.04	1.04	1.08	-0.51	0.51
P2(111)	0.75	0.45	1.94	1.49	0.18	0.17
CuO/Ag(111)	1.00	>0.02	>1.12	1.10	-0.91	0.18
CuO/Ag(100)	1.00	0.02	0.94	0.92	-0.89	0.19
CuO/Ag(110)	1.00	-0.06	0.90	0.96	-0.57	0.51

is determined through the climbing-image NEB method using as initial state the most stable configuration for ethylene adsorption and as final state the product molecules in gas phase (i.e. far enough from the surface so that they do not interact significantly with the surface). On the Ag-O(2×2)(111) and Ag-O(2×2)(100) surface with pre-adsorbed oxygen both reactions are known to proceed through a common oxametallacycle (OMC) intermediate [94, 109, 53], where ethylene is bonded with one C atom to a surface metal atom and with the other C atom to oxygen. The formation of Ac has a slightly (0.01 eV to 0.07 eV [94]) smaller activation barrier in both cases, in agreement with experimental measurements [94]. Similar conclusions have been reached also for the thin Ag oxides [110]. We find, on the other hand, that on thin copper-oxide layers the picture is different. We find that while the formation of Ac always proceeds from the formation of an intermediate (OMC occurs in all cases except for the P2 structures, where ethylenedioxy forms), the formation of EO can proceed through different paths, depending on the surface structure of the catalyst.

The formation of EO on the P2/Ag(111) and P4-OCu3/Ag(111) structures does not involve the formation of an intermediate. In the case of CuO/Ag(111) we find that there are two competing reaction paths for the formation of EO. For the lowest energy one, EO is formed directly from the physisorbed ethylene molecule, without the formation of any intermediate. In the second path, whose transition state is only slightly (0.02 eV) higher in energy than the direct path, the reaction goes through the formation of an OMC. On the other hand, we find that the OMC is a common intermediate for both the formation of Ac and EO in the case of Ag-O(2 × 2)/Ag(111), CuO/Ag(100) and CuO/Ag(110). These findings clearly stress how the reaction mechanism is structure-dependent. The activation energies for the formation of Ac (E^*_{Ac}) and EO (E^*_{EO}) are shown in Table 2.3, together with their difference ($\Delta E^* = E^*_{Ac} - E^*_{EO}$). A positive value of ΔE^* suggests a selective formation of EO. In Fig. 2.11 we show the energy profile of the two competing reactions

on some of the most relevant surface structures. The energies of the initial and final states correspond to the reagents and products physisorbed on the surface. There is a range of possible values for the activation barriers, due to the different mechanisms underlying the epoxidation reactions on different surface structures. In addition to the activation barriers reported in Table 2.3, we note that, using analogous methodologies to the ones employed here, the value of ΔE^* for the O(2×2)/Ag(100) surface has been found to be just 0.01 eV smaller that the one on the (111) structure [53]. We can see that all the Cu-containing structures provide a better selectivity toward EO compared to pure Ag structures, in agreement with the superior selectivity of Ag-Cu alloys compared to pure Ag seen in experiments [94]. The P2/Ag(111) structure, in particular, is very selective, although it involves activation energies larger that any other surface structure considered here. The structures on the (100) and (110) surfaces, on the other hand, provide only a marginally higher selectivity than the Cu-free structures.

For the case of CuO/Ag(111) structure, the mechanisms is more complicated, since in the lowest energy path, OMC is found as the meta-stable intermediate state only for the formation of Ac whereas it is not for the formation of EO. To determine the difference of activation energies in this case, Piccinin *et al.* have adopted the so-called "Sabatier analysis", proposed by Nørskov *et al.* [111, 112], to give an estimation of selectivity of CuO/Ag(111) [102]. In this approach, the authors have found that a lower bound of the difference of the effective activation energies can be evaluated as the difference between the highest points in the energy profiles of the two processes, > 0.02 eV, see in Fig. 2.11. Therefore, this result states that CuO/Ag(111) structure can be from slightly to very selective toward the formation of EO. To this end, we note here that the absolute values of ΔE^* computed on the structures considered in this work are significantly small, i.e. < 0.1 eV (with the acception of P2/Ag(111) structure, where $\Delta E^* = 0.45$ eV). These values are on order of the numerical error of NEB algorithms, i.e. ± 0.01 eV (see in Appendix A). Therefore, the catalyst selectivity toward EO synthesis computed in this work must be regarded as qualitative.

In previous studies of ethylene epoxidation on pure Ag and other monometallic catalysts, the activation energies for the formation of Ac and EO was found to be in agreement with the Brønsted-Evans-Polanyi (BEP) relation [80, 81], introduced earlier in this Chapter. Thus, we now turn to examine this relation in ethylene epoxidation on the stable surface structures of pure Ag and Ag-Cu alloy. In Fig. 2.12, the results show that, for two competing pathways forming Ac and EO, there are two different BEP relations displayed through two linear dependences of the activation energies, E^*_{Ac} and E^*_{EO} on the reaction enthalpies, $\Delta \mathrm{H}_{\mathrm{Ac}}$ and $\Delta \mathrm{H}_{\mathrm{EO}}$, respectively. The values $\Delta \mathrm{H}_{\mathrm{Ac(EO)}}$ for the formation of Ac(EO) on different surface structures are computed as the difference of the total energies between the final states and the initial states in mechanism of ethylene epoxidation, presented in Table 2.3. These findings are at variance with the universal relation proposed for dissociation reaction of simple molecules on different metal surfaces [42]. In ethylene epoxidation, however, the two reaction involve different mechanisms, i.e. in the formation of Ac,

hydrogen shifts between the two C atoms, and the formation of a C=O double bond, while closure of the epoxy ring occurs in the formation of EO, and thus clearly display a different BEP law. Interestingly, we find that the geometry of the two transition states is only weakly influenced by the underlying surface structures. As shown in Fig. 2.13, the reactions on all the selected surfaces share very similar transition states. Based on the assumption of the presence of OMC intermediate, A. Kokalj *et al.* [53] described the formation of the TS of Ac as a partial break of both the bond between O and the surface and the one between C and the surface, whereas in the formation of EO at TS the bond between C and the surface is completely broken. This interpretation suggests that the difference of binding energies between C- and O-surface is the appropriate descriptor to explain the enhanced selectivity of Cu containing structure such as the surface alloy. However, in this work, the results have shown that OMC is not always formed as the intermediate in ethylene epoxidation, and the enhancement in selectivity of some structures can be attributed to the structure-dependent mechanism, that is different from what has been found on the clean Ag or 2D surface alloy. In the following section, we will examine the structures on which the formation of OMC is favorable, and the model proposed by A. Kokalj *et al.* [53] will be re-discussed.

The results presented in this work, therefore, suggest that there is not an unique surface structure that is solely responsible for the catalytic activity of the Ag-Cu alloy. Namely, in an oxidizing environment, several surface structures can be present, and, thus, the mechanism for ethylene oxidation is different according to the difference between the stable structures. Moreover, the computed activation energies toward the formation of the oxidation products on these structures are found to be similar, and hence, it can be understood that these structures can be available to play a role in the catalytic process. The picture illustrated by the synergetic interplay of different reaction pathways and of different surface structures is very important for describing and interpreting the efficiency and long time-scale catalysis of the steady state. In real catalysis, temporal fluctuations of the local structure and composition among the ones identified in this work might be present, and this can induce a change of the mechanism of reaction.

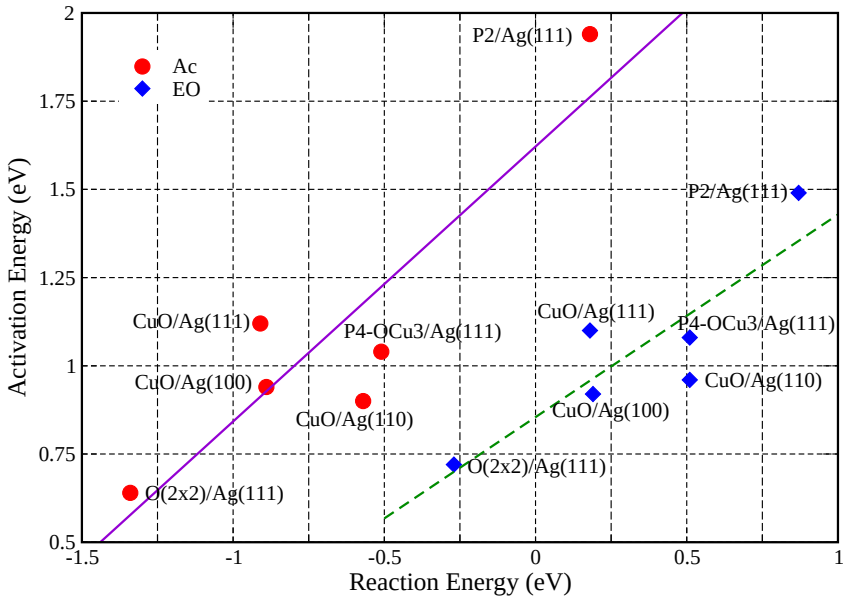

Figure 2.12: Brønsted-Evans-Polanyi relation between the reaction energy and the activation energy. The red circles correspond to the formation of acetaldehyde, while the blue diamonds correspond to the formation of ethylene oxide. The violet solid line and the green dashed line are linear fits for the formation of acetaldehyde and ethylene oxide, respectively.

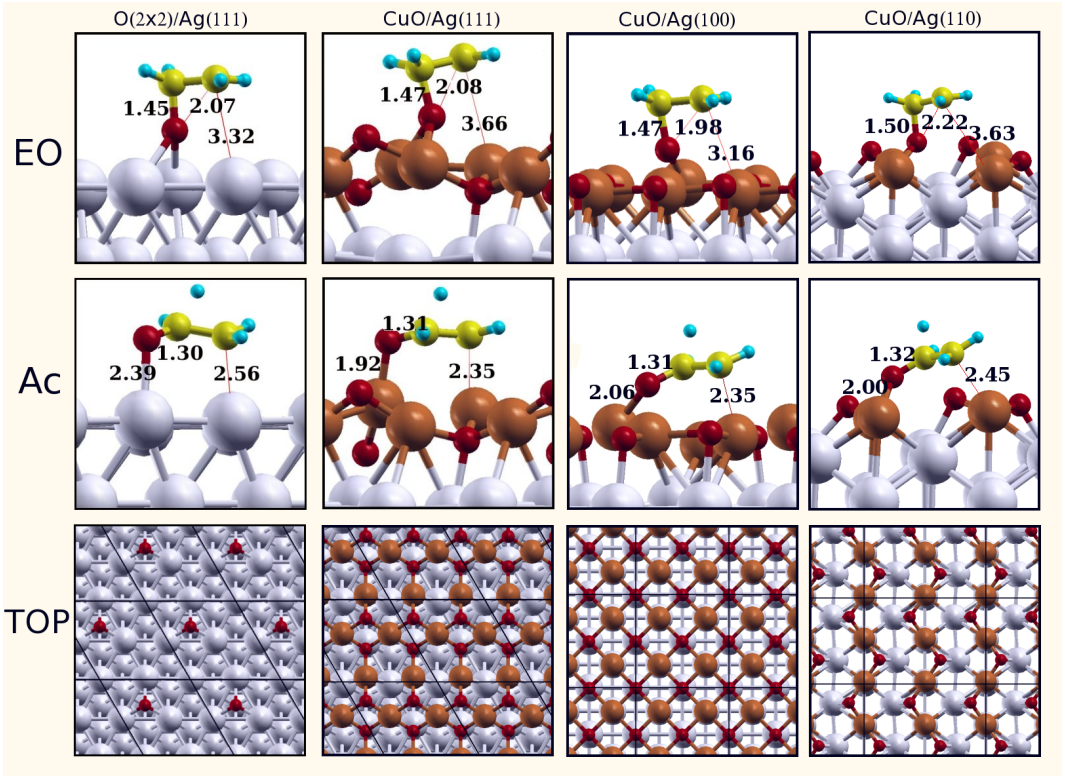

Figure 2.13: Sketch of the transition state geometries for the formation of ethylene oxide (top panels) and acetaldehyde (central panels) and top view of the surface for four structures. The small red (black) atoms represent oxygen, the larger brown (dark-grey) ones represent copper, the larger grey (light-grey) ones represent silver, the small yellow (grey) ones represent carbon, and the small green (grey) ones represent H. Note how the geometry of the transition state is, to a large degree, independent of the surface structure.

2.3.3 The role of sub-surface oxygen on catalytic properties of Ag-Cu Alloy in ethylene epoxidation

Sub-surface oxygen species, O^{sub}, has often been suggested to be responsible for catalyst activity in several oxidation reactions [3]. In particular, on Ag surfaces, O^{sub} has been suggested to play a pivotal role in several oxidation reactions, such as the partial oxidation of methanol to formaldehyde [113], carbon mono-oxide oxidation [114], and especially, ethylene epoxidation [115, 55, 41]. However, as mentioned in section 2.1.1, the role played of O^{sub} in the ethylene epoxidation is still a controversial topic. For example, van Santen *et al.* have suggested that the presence of O^{sub} induces the formation of the loosely bounded electrophilic oxygen O^{sur} on surfaces [55]. Mavrikakis *et al.*, on the other hand, by DFT calculations, found that O^{sub} changes the properties of Ag surfaces by shifting the d-band center of Ag atoms with respect to the Fermi level, increasing its reactivity [57].

In the ethylene epoxidation on the Ag surfaces, experiments detect the presence of O^{sub} upon oxidizing ethylene molecules, however, the catalytic promotion of this oxygen strongly depends on the experimental set-ups. For example, in the transient experiments by Grant and Lambert [116] and van Santen and co-workers [117, 118], an increase of silver selectivity toward the formation of EO was found with presence of O^{sub}. On the other hand, the experiments done by Campbell and co-workers, under steady-state conditions showed that O^{sub} is more stable with respect to increase of temperature compared to O^{sur}, and in this case O^{sub} does not effect the catalytic properties [119, 120]. Similarly, by using temperature program reaction (TPR) and temperature program desorption (TPD) for ethylene and oxygen species, Atkins *et al.* showed that O^{sub} can be present on Ag(111) surface with a coverage up to 2.28 ML [121]. Moreover, measurements of Ag surfaces in oxygen atmosphere showed that O^{sub} induces an electronic effect on Ag atoms on surfaces in the same way as Cl does [122, 123, 124].

To the best of our knowledge, no study has addressed O^{sub} on Ag-Cu surfaces. In *ex situ* XPS experiments, Barteau *et al.* have obtained ethylene epoxidation reaction on Ag-Cu. The authors have found that the selectivity of Ag-Cu alloy increases with the oxygen pressure, which was suggested to be related to the role of O^{sub} formed on the catalysts [74]. In the previous section of this thesis, we have discussed how, on thermodynamic phase diagram of the (111) surface, O^{sub} can be stabilized on the CuO/Ag(111) structure at high pressure conditions, while on other low-index surfaces such as (110) or (100), O^{sub} is not energetic favorable. Here, we will study the effect of O^{sub} on the selectivity and reactivity of Ag-Cu alloy in ethylene epoxidation, and compare the results with those obtained on pure Ag. In addition, in order to rationalize these findings, a selectivity indicator along the lines proposed by A. Kokalj *et al.* [93, 53, 93] will also be considered.

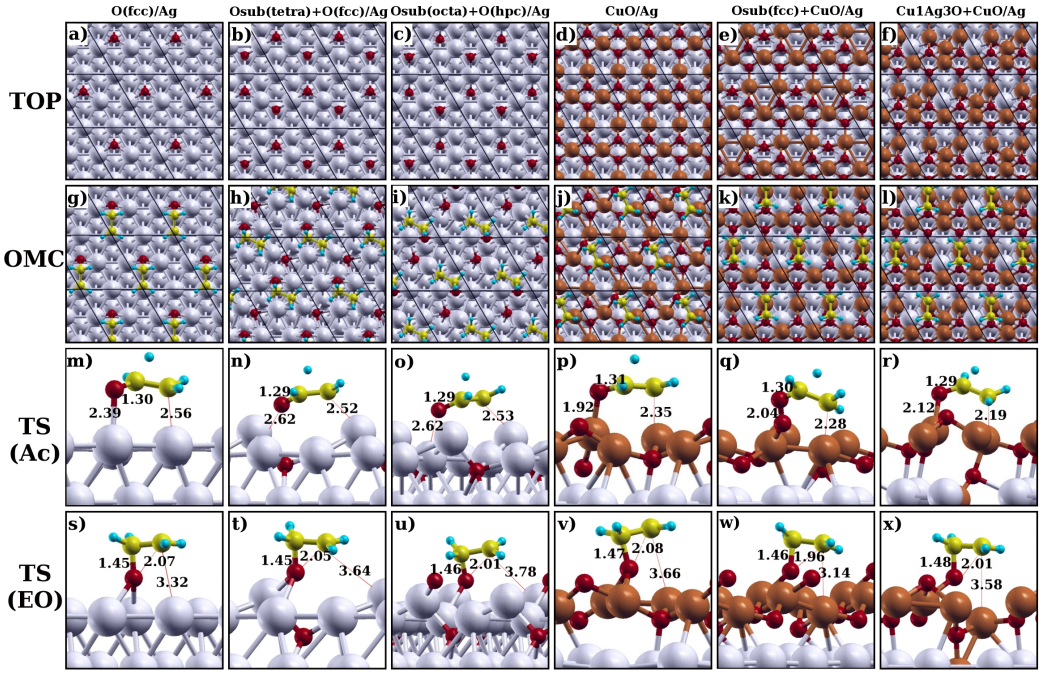

Figure 2.14: Top view of the six low energy surface structures (a–f) and chemisorbed ethylene for Oxametallacycle(OMC) configurations (g–l). Sketch of the transition state geometries for the formation of acetaldehyde (m–r) and ethylene oxide (s–x) of the six low energy structures considered in this work. The small red atoms represent oxygen, the large brown ones represent copper, the large light-grey ones represent silver, the small yellow ones represent carbon, and the small green ones represent H.

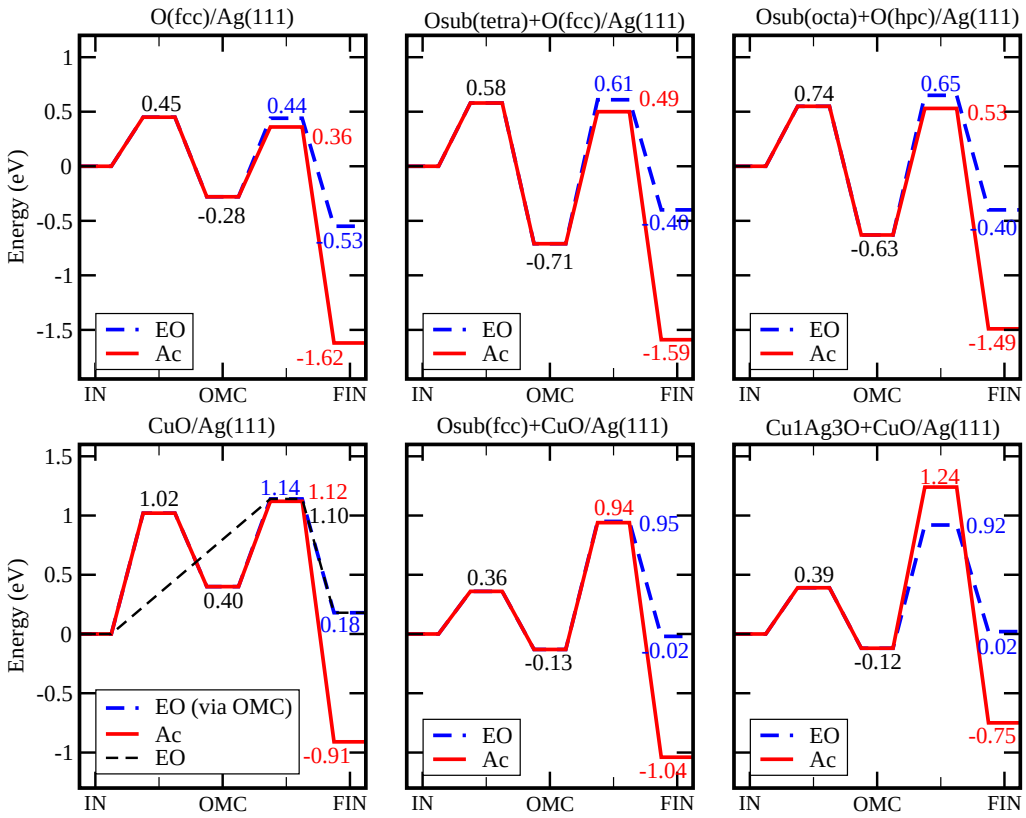

Figure 2.15: Energy profiles for ethylene epoxidation over the selected surface structures. At the initial state (IN) ethylene is physisorbed on the surface, the intermediate state is the Oxametallacycle (OMC), while the final state (FIN) the reaction has either produced acetaldehyde (Ac, red solid line) or ethylene oxide (EO, blue dashed line). The EO formation can be preceded directly from the initial state without formation of OMC intermediate (black dashed line). The energies of the final states correspond to the products physisorbed on the surface.

2.3.3.1 Formation of sub-surface oxygen on Ag(111) and Ag-Cu(111) surface

We found that for the Ag-Cu system in the presence of O and ethylene, the catalyst surfaces can consist of several possible structures, and energetically equivalent structures can coexist under catalytic operation conditions. We will, however, restrict ourselves to study the formation of O^{sub} on the stable structures of the (2×2) periodic surfaces of pure Ag(111), CuO/Ag(111) and CuO/Ag(111) with Cu replacing Ag at the second layer below the copper-oxide layer. Furthermore, on Ag-based alloy particles, because Ag(111) is the lowest energy surface for silver particles [125], the typical understanding is that a large portion of the nanoparticle surfaces will consist of (111) planes. This is not necessarily true at high temperature, where the particle can be quite round, especially in the case of noble metals, and in the presence of oxide-like structures on the surface, that can alter the relative surface energies compared to the case of pure Ag at zero temperature

In Fig. 2.14(a), we show a pure Ag(111) surface with 0.25 ML of chemisorbed oxygen at the face-centered cubic (fcc) site on the surface, which is noted by O(fcc)/Ag(111). The presence of O^{sub} on the pure O(fcc)/Ag(111), as shown in Fig. 2.14(b-c), is characterized by 0.25 ML O^{sur} and 0.25 ML O^{sub} coverage. We have found two stable configurations having the same surface free energy that are characterized by: (i) a structure with O^{sur} at fcc site and O^{sub} at the the tetrahedral (tetra), i.e. Fig. 2.14(b), which are noted Osub(tetra)+O(fcc)/Ag(111), and (ii) a structure with O^{sur} at hexagonal close packed (hpc) site and O^{sub} at octahedral (octa), i.e. Fig. 2.14(c), which are noted Osub(octa)+O(hpc)/Ag(111). This finding is in agreement with the results calculated for O^{sub} configurations on the p(2×2) Ag(111) by Scheffler and co-workers [56].

On Ag-Cu alloys, under catalytic environment, stable surface structures have been experimentally examined to have a thin copper oxide-like layer on the top of pure Ag slabs [79, 78, 77]. In the previous section, we have presented a computational study for the stability of the structures on the low-index Ag-Cu surfaces in a thermodynamic equilibrium condition. In particular, on the (111) surfaces, the structure formed by thin CuO layer on Ag(111) surfaces, named as CuO/Ag(111), has been found as the most stable structure under the conditions relevant to experiments, see Fig. 2.14(d). In addition, the O^{sur} formation on this stable structure has been also preliminarily reported. We have found that thermodynamically favorable O^{sub} forms only at oxygen partial pressure greater than 10^2 atm and $T = 600$ K. The stable position of this O^{sub} is predicted at the fcc site on (111) facet at the interface between the CuO layer and silver, labeled Osub(fcc)+CuO/Ag(111), shown in Fig. 2.14(e).

The catalytic properties of Osub(fcc)+CuO/Ag(111) as shown later are very crucial in ethylene epoxidation reaction, and in this work we also design a third group of structures that are relevant for O^{sub} formation. The predicted structures are still keeping the positive properties of this species, while they can be present on the thermodynamic phase diagram under experimental conditions. On the (2×2)

periodicity of the (111) surface, the structures contain both Cu and Ag content under the CuO layer, and are named $Cu_xAg_{(4-x)}O_y$+CuO/Ag(111). Here x is the number of Cu atoms replacing Ag on the (2×2) slab, and y is the number of O atoms at sub-surface positions. In the next section of this work, the reaction path calculated by NEB algorithm will be illustrated for one structure with $x = 1$ and $y = 1$, Cu1Ag3O+CuO/Ag(111), see in Fig. 2.14(f), while, for the others their stability as well as their catalytic properties will be estimated in detail in the last section.

2.3.3.2 Effects of sub-surface Oxygen on transition states and reaction mechanisms

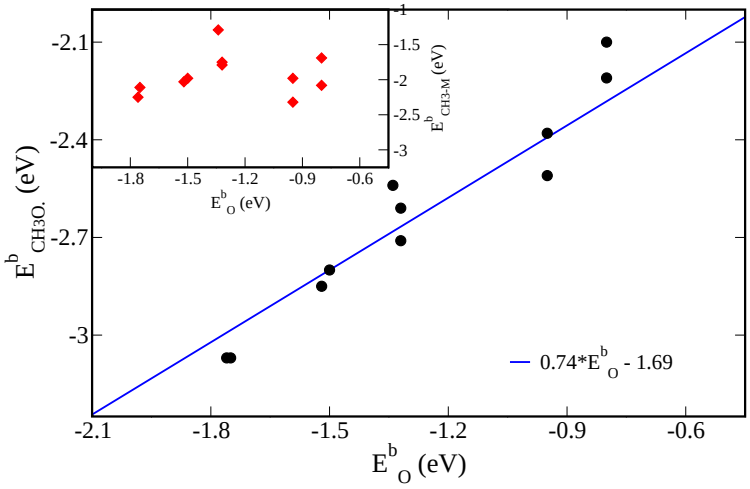

Figure 2.16: The linear relationship between $E^{\mathrm{b}}_{\mathrm{CH_3O.}}$ and $E^{\mathrm{b}}_{\mathrm{O}}$, the relationship between $E^{\mathrm{b}}_{\mathrm{CH_3.}}$ and $E^{\mathrm{b}}_{\mathrm{O}}$ represented in the inset.

Table 2.4: Cu surface content (Θ_{Cu}), sub-surface oxygen content (Θ_{Osub}), activation barriers of the selectivity controlling step for the formation of acetaldehyde (E^*_{Ac}) and ethylene oxide (E^*_{EO}), and the difference between two (ΔE^*) for selected surface structures.

Surface	Θ_{Cu}(ML)	Θ_{Osub}(ML)	ΔE^*(eV)	E^*_{Ac}(eV)	E^*_{EO}(eV)
O(fcc)/Ag(111)	0.00	0.00	-0.08	0.64	0.72
Osub(tetra)+O(fcc)/Ag(111)	0.00	0.25	-0.12	1.20	1.32
Osub(octa)+O(hpc)/Ag(111)	0.00	0.25	-0.12	1.16	1.28
CuO/Ag(111)	1.00	0.00	>0.02	>1.12	1.10
Osub(fcc)+CuO/Ag(111)	1.00	0.25	-0.01	1.07	1.08
Cu1Ag3O+CuO/Ag(111)	1.25	0.25	0.32	1.36	1.04

Table 2.5: Binding energies (in eV) of the stable Oxametallacycle ($E^{\mathrm{b}}_{\mathrm{OMC}}$) configurations, on-surface oxygen ($E^{\mathrm{b}}_{\mathrm{O}}$), methyl ($E^{\mathrm{b}}_{\mathrm{CH3.}}$), methoxy ($E^{\mathrm{b}}_{\mathrm{CH_3O.}}$), and physisorbed acetaldehyde and ethylene oxide, $E^{\mathrm{b}}_{\mathrm{Ac}}$, $E^{\mathrm{b}}_{\mathrm{EO}}$, respectively, with the selected surfaces. $\Delta \mathrm{H_{Ac}}$, and $\Delta \mathrm{H_{EO}}$ are the reaction enthalpies for the formation acetaldehyde and ethylene oxide, respectively. The two last columns show the selectivity ($\Delta E^* = E^*_{\mathrm{Ac}} - E^*_{\mathrm{EO}}$), calculated from the selectivity indicator of Eq.(2.40) ($\Delta \bar{E}^*$) and from NEB algorithm (ΔE^*).

Surface	$E^{\mathrm{b}}_{\mathrm{OMC}}$	$E^{\mathrm{b}}_{\mathrm{O}}$	$E^{\mathrm{b}}_{\mathrm{CH3.}}$	$E^{\mathrm{b}}_{\mathrm{CH_3O.}}$	$E^{\mathrm{b}}_{\mathrm{Ac}}$	$E^{\mathrm{b}}_{\mathrm{EO}}$	$\Delta \mathrm{H_{Ac}}$	$\Delta \mathrm{H_{EO}}$	$\Delta \bar{E}^*$(eV)	ΔE^*(eV)
O(fcc)Ag(111)	-0.49	-0.40	-1.59	-2.17	-0.13	-0.06	-1.34	-0.27	-0.03	-0.08
(OMC_1)Osub(tetra)+O(fcc)/Ag(111)	-0.23	-0.95	-1.98	-2.38	-0.19	0.01	-1.16	0.08	-0.15	-0.25
(OMC_2)Osub(tetra)+O(fcc)/Ag(111)	-0.76	-0.95	-2.32	-2.51	-0.41	-0.26	-0.88	0.31	-0.15	-0.11
(OMC_1)Osub(octa)+O(hpc)/Ag(111)	-0.18	-0.80	-1.69	-2.10	-0.12	-0.06	-1.26	-0.15	-0.10	-0.24
(OMC_2)Osub(octa)+O(hpc)/Ag(111)	-0.67	-0.80	-2.08	-2.21	-0.13	-0.07	-0.86	0.23	-0.15	-0.12
CuO/Ag(111)	0.38	-1.34	-1.29	-2.54	-0.19	-0.12	-0.91	0.18	0.16	0.02
(OMC_1)Osub(fcc)+CuO/Ag(111)	-0.02	-1.32	-1.79	-2.71	-0.11	-0.22	-1.01	-0.01	0.22	0.32
(OMC_2)Osub(fcc)+CuO/Ag(111)	-0.19	-1.32	-1.75	-2.61	-0.22	-0.22	-0.91	0.11	0.12	-0.01
Cu1Ag3O+CuO/Ag(111)	-0.12	-1.52	-2.03	-2.85	-0.10	-0.35	-0.63	0.10	0.25	0.31
Cu2Ag2O2+CuO/Ag(111)	-0.13	-1.76	-2.25	-3.07	-0.19	-0.16	–	–	0.28	–
Cu3Ag1O2+CuO/Ag(111)	-0.01	-1.75	-2.11	-3.07	-0.16	-0.16	–	–	0.07	–
Cu4Ag0O4+CuO/Ag(111)	-0.03	-1.50	-1.98	-2.80	-0.17	-0.24	–	–	0.06	–

On the selected structures, we study the minimum energy paths (MEP) of the two competing chemical reactions leading to the formation of final states (FS) Ac and EO. The transition state (TS) of the reactions is determined through the climbing-image (CI-NEB) method [88]. Similar to the previous works, the physisorbed ethylene molecule is considered as the initial state. The energy profiles consist of initial state's, transition state's, and final state's energies, and are shown in Fig. 2.15. We found that, on the surfaces with O^{sub}, OMC is formed as the common intermediate state on MEPs for the formation of both Ac and EO. In the first column of Table 2.5, we present the binding energy E^{b}_{OMC} relative to ethylene molecule in the gas phase, as given in Eq.(2.28). The results show that there are many possible OMC intermediates with different binding energies formed on the surfaces. The geometry of the most stable OMCs on these surfaces is shown in Fig. 2.14(g-l). In addition, it is also found that the presence of O^{sub} increases the stability of OMC intermediates on the Ag(111) and CuO/Ag(111), while this intermediate becomes less favorable when more Cu atoms replace Ag atoms in the second layer under the first CuO layer.

From OMC intermediate, the formation of Ac and EO is characterized by activation energies E^{*}_{Ac} and E^{*}_{EO}, respectively. The values of these energies are presented in Table 2.4, together with their difference $\Delta E^{*} = E^{*}_{Ac} - E^{*}_{EO}$. Here we remind that according to the definition of selectivity a positive value of ΔE^{*} indicates to a selective formation of EO. The results suggest that, on Ag(111), the presence of O^{sub} increases the height of activation energies in both reactions ($\sim$ 0.5 eV), in agreement with the result found by Mavrikakis *et al.* [58]. On the thin oxide-like layer structures, in contrast, O^{sub} slightly decreases the activation energies (~ -0.05 eV), however, these energies change in different ways with respect to an increase of the Cu content, i.e. E^{*}_{Ac} increases by 0.3 eV, while E^{*}_{EO} is almost unchanged (~ -0.05 eV). This means that the reactivity and selectivity of thin-oxide structures is ruled mainly by the Cu composition.

In order to get insights into the factors that cause alteration of activation energies in the pathways and, in particular, the selectivity, one needs to search for simpler quantities correlating to the kinetics of reactions. In section 2.3.2, the study of mechanism for ethylene epoxidation found the BEP relations between activation energies, E^{*}s, and enthalpy of reaction on the stable structures of Ag-Cu(111), (100), (110), and Ag(111) surfaces. Similarly, here we also examine this relation for O^{sub} structures shown in Fig. 2.17. One can see that the linear relation of the BEP principle, $E^{*} = \alpha \Delta H + \beta$, still holds for the O^{sub} structures. The fitting errors, root mean squared errors (RMSE), and maximum absolute error (MAE), associated to BEP relations for the formation of EO are of 0.10 and 0.17 eV, respectively, whereas for the formation of Ac are RMSE = 0.11 eV and MAE = 0.27 eV. Although the approximate magnitude of the activation energies for Ac and EO formation can be determined from the BEP principle, the selectivity of catalyst toward EO formation computed by taking the difference between the activation energies, $\Delta E^{*} = E^{*}_{Ac} - E^{*}_{EO}$, can not be estimated by the BEP principle with a sufficient degree of accuracy. The reason of this drawback is that the magnitude of ΔE^{*} is too small

(< 0.1 eV) compared to the errors in the BEP estimate of E^*_{Ac} and E^*_{EO}. These errors yield an overestimation for ΔE^*. This, therefore, requires to find an improvement for the BEP relations. In this thesis, we will adopt the approach proposed by A. Kokalj *et al.* [53, 93] to correct the BEP principle in the ethylene epoxidation. Catalyst selectivity toward the formation of EO with respect to Ac formation will be derived from the new BEP-like relations, that will be briefly recall in the following.

By considering the structural features of transition states for the two reactions, see in Fig. 2.14(m-x), A. Kokalj *et al.* noticed that on different substrates $\mathrm{TS^{EO}}$ is characterized by a fully broken C-surface bond, whereas, in $\mathrm{TS^{Ac}}$ both the C- and O-surface bonds are only partially broken. Indeed, in the formation of EO, the closure of epoxy ring is characterized by the oxygen shift beneath the ethylene fragment that is concomitantly lifting upward, and thus breaking the C-surface bond completely. On the other hand, the formation of Ac is determined by the hydrogen transfer from one C to the second C in the ethylene molecule, and the formation of C=O double bond, that thus break the C- and O-surface bonds only partially. This mechanism shows that the activation energies for the formation of Ac and EO can be attributed to the strength of C- and O-surface bonds. To make these arguments more quantitative, A. Kokalj *et al.* decomposed the OMC intermediate into two different groups, methyl ($CH_3\cdot$) and methoxy ($CH_3O\cdot$) radicals, that interact with the surface as follows:

$$E^{\mathrm{b}}_{\mathrm{CH_3\cdot}} = E^{\mathrm{CH_3\cdot}}_{\mathrm{tot}} - E_{\mathrm{surf.}} - E^{\mathrm{CH_3\cdot}}_{\mathrm{iso}} \tag{2.30}$$

and

$$E^{\mathrm{b}}_{\mathrm{CH_3O\cdot}} = E^{\mathrm{CH_3O\cdot}}_{\mathrm{tot}} - E_{\mathrm{surf.-1O}} - E^{\mathrm{CH_3O\cdot}}_{\mathrm{iso}}. \tag{2.31}$$

Here $E^{\mathrm{CH_3\cdot}}_{\mathrm{tot}}$ and $E^{\mathrm{CH_3O\cdot}}_{\mathrm{tot}}$ are total energies of the catalyst surface with the chemisorbed $CH_3\cdot$ and $CH_3O\cdot$. $E_{\mathrm{surf.-1O}}$ is the total energy of the surface removed one $\mathrm{O^{sur}}$ atom. The values of $E^{\mathrm{CH_3\cdot}}_{\mathrm{iso}}$, and $E^{\mathrm{CH_3O\cdot}}_{\mathrm{iso}}$ are the total energies of radicals assumed to be isolated in vacuum. Computed results for these E^{b}s are presented in the third and fourth column of Table 2.5. Through these simple quantities, the magnitude of the reaction barriers for the formation of EO and Ac can be understood in terms of binding energies of these radicals. Namely, for the formation of EO, since the O-surface bond is not broken in the transition state, $\mathrm{TS^{EO}}$, the energy barrier E^*_{EO} will not be related to this bond, but to strength of the C-surface bonds. A higher $E^{\mathrm{b}}_{\mathrm{CH_3\cdot}}$ will be associated to a higher E^*_{EO}. On the other hand, since the O- and C-surface bonds are partially broken during forming $\mathrm{TS^{Ac}}$, the activation energy for formation Ac is related to both bonds. Increasing binding energies of both $CH_3\cdot$ and $CH_3O\cdot$ can induce a higher activation energy for the formation of Ac. The relations can be represented through expressions of the activation energies for the EO and Ac formation from OMC, as follows:

$$E^*_{\mathrm{EO}} = C_1 + \alpha E^{\mathrm{b}}_{\mathrm{CH_3\cdot}} + \gamma E^{\mathrm{BEP}}_{\mathrm{EO}}, \tag{2.32}$$

and

$$E^*_{\mathrm{Ac}} = C_2 + \alpha E^{\mathrm{b}}_{\mathrm{CH_3O\cdot}} + \beta E^{\mathrm{b}}_{\mathrm{CH_3\cdot}} + \gamma E^{\mathrm{BEP}}_{\mathrm{Ac}}. \tag{2.33}$$

Where C_1 and C_2 are additive constants, while $E_{\mathrm{Ac}}^{\mathrm{BEP}}$ and $E_{\mathrm{EO}}^{\mathrm{BEP}}$ are the energy contributions computed by the BEP principle. The calculation of these energies in the approach by A. Kokalj *et al.* [53, 93] is obtained through the difference between binding energy of Ac (or EO) and that of the OMC intermediate with the substrate, that is:

$$E_{\mathrm{Ac}}^{\mathrm{BEP}} = E_{\mathrm{Ac}}^{\mathrm{b}} - E_{\mathrm{OMC}}^{\mathrm{b}} \text{ and } E_{\mathrm{EO}}^{\mathrm{BEP}} = E_{\mathrm{EO}}^{\mathrm{b}} - E_{\mathrm{OMC}}^{\mathrm{b}}, \tag{2.34}$$

where $E_{\mathrm{Ac}}^{\mathrm{b}}$ and $E_{\mathrm{EO}}^{\mathrm{b}}$ are computed as:

$$E_{\mathrm{Ac}}^{\mathrm{b}} = E_{\mathrm{tot}}^{\mathrm{Ac}} - E_{\mathrm{surf.-1O}} - E_{\mathrm{gas}}^{\mathrm{Ac}}, \tag{2.35}$$

and

$$E_{\mathrm{EO}}^{\mathrm{b}} = E_{\mathrm{tot}}^{\mathrm{EO}} - E_{\mathrm{surf.-1O}} - E_{\mathrm{gas}}^{\mathrm{EO}}. \tag{2.36}$$

The computed values of $E_{\mathrm{Ac}}^{\mathrm{b}}$ and $E_{\mathrm{EO}}^{\mathrm{b}}$ on the structures considered are presented in Table 2.5. The results show that, on Ag(111), the increase of E_{EO}^{*} and E_{Ac}^{*} in the presence of $\mathrm{O^{sub}}$ does not orderly depend on $E_{\mathrm{Ac}}^{\mathrm{b}}$ and $E_{\mathrm{EO}}^{\mathrm{b}}$, whereas it correlates with increasing binding energies of radicals, i.e. $E_{\mathrm{CH_3\cdot}}^{\mathrm{b}}$ increases from -1.59 to -2.32 eV, and $E_{\mathrm{CH_3O\cdot}}^{\mathrm{b}}$ increases from -2.17 to -2.51 eV. In addition, in Fig. 2.16, we also find the linear relation between the binding energy of $\mathrm{O^{sur}}$, $E_{\mathrm{O}}^{\mathrm{b}}$, and $E_{\mathrm{CH_3O\cdot}}^{\mathrm{b}}$, however, with $E_{\mathrm{CH_3\cdot}}^{\mathrm{b}}$ this relation is not systematic. These findings are consistent with those on Ag(111) in Ref. [58], where the study found that E_{EO}^{*} increases with the presence of $\mathrm{O^{sub}}$, and this energy relates to $E_{\mathrm{O}}^{\mathrm{b}}$. On the other hand, Fig. 2.15 shows that while on pure Ag catalyst OMC forms as the common intermediate, in the case of CuO/Ag(111), there are two competing reaction paths for the formation of EO. The first one has a lower energy, and it goes directly toward to EO without the formation of any intermediate. The second path, whose transition state is only slightly (0.02 eV) higher than the direct path, goes through the formation of an OMC. In contrast, the single MEP through the formation of OMC is found in the reaction path toward to EO when $\mathrm{O^{sub}}$ presents on CuO/Ag(111). The presence of $\mathrm{O^{sub}}$ on CuO/Ag(111) increases E_{EO}^{*} and E_{Ac}^{*} that are computed as the difference energy between $\mathrm{TS^{Ac}}$, and $\mathrm{TS^{Ac}}$ and OMC intermediate, i.e. ~ 0.35 eV for the both activation energies. This increase is found to be related to the enhancement of $E_{\mathrm{CH_3\cdot}}^{\mathrm{b}}$ and $E_{\mathrm{CH_3O\cdot}}^{\mathrm{b}}$, in agreement with relation in Eqs.(2.32 and 2.33). In addition, the substitution of Ag atoms by Cu atoms at the layer under the first CuO layer induces a significant increase of binding strength of bonds between $\mathrm{CH_3\cdot}$, $\mathrm{CH_3O\cdot}$ radicals and the surface. However, this only increases the activation energy for the formation of Ac, i.e. ~ 0.60 eV, while for EO it is not effected, which can be seen as a limit case of the new BEP-like relations.

2.3.3.3 Selectivity indicators

From NEB calculations presented in Fig. 2.15 and Table 2.4, the results show the slight decrease of the selectivity of Ag(111) and CuO/Ag(111) catalysts in EO synthesis (~ 0.04 eV), while Cu significantly improves a selective formation of EO. In

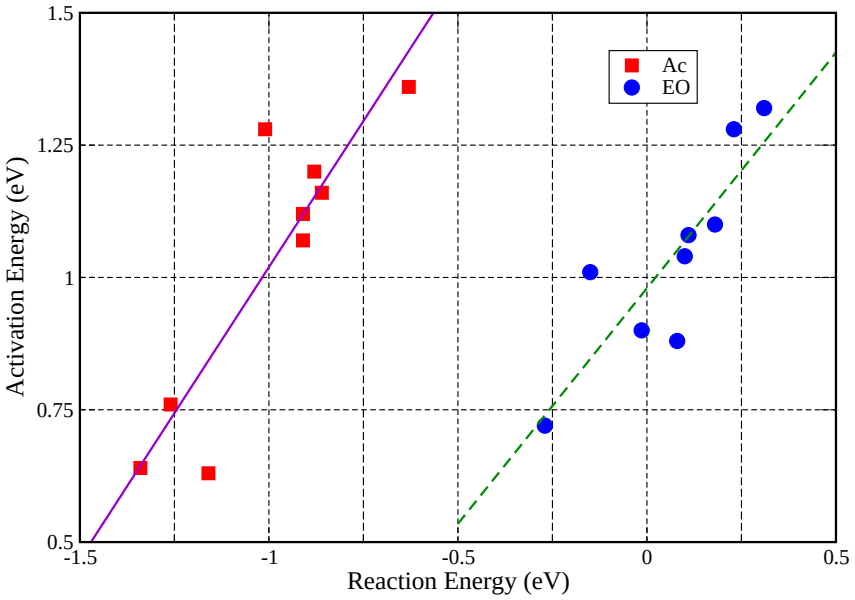

Figure 2.17: Brønsted-Evans-Polanyi relation between the reaction energy and the activation energy. The red squares correspond to the formation of acetaldehyde, while the blue circles correspond to the formation of ethylene oxide. The violet solid line and the green dashed line are linear fits for the formation of acetaldehyde and ethylene oxide, respectively.

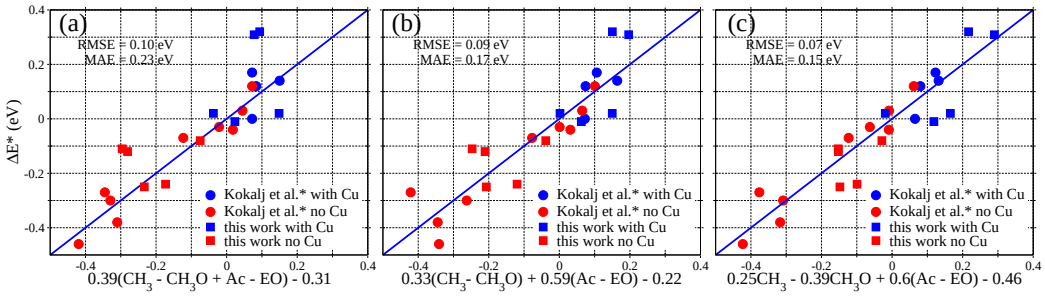

Figure 2.18: Comparison of selectivity indicators for different catalysts included the computed data of A. Kokalj *et al.* [53, 93] (filled cycle) and our data (filled square). a) The indicator proposed by A. Kokalj *et al.* [53, 93] according to Eq.(2.38). b) The first new indicator according to Eq.(2.39). c) The second new indicator according to Eq.(2.40).

order to clarify the effects of these promoters on selectivity, a selectivity indicator, will be employed in this section. Taking the difference between E^*_{Ac} and E^*_{EO} expressed in the relations of Eqs.(2.33 and 2.32), one can obtain a simple approximation for selectivity as:

$$\Delta E^* = \alpha E^{\mathrm{b}}_{\mathrm{CH_3\cdot}} + \beta E^{\mathrm{b}}_{\mathrm{CH_3O\cdot}} + \gamma(E^{\mathrm{b}}_{\mathrm{Ac}} - E^{\mathrm{b}}_{\mathrm{EO}}) + C. \tag{2.37}$$

This expression shows that the selectivity can be obtained from the estimation for the binding energies of $CH_3\cdot$, $CH_3O\cdot$ radicals, and of the two final states, Ac and EO, to the catalyst surfaces. Through several surface structures, A. Kokalj *et al.* [93, 53] established an approximation for the parameters in Eq.(2.37), such that $\alpha = -\beta = \gamma \backsimeq 0.39$ and $C = -0.31$, and the indicator is given by:

$$\Delta E^* = 0.39[E^{\mathrm{b}}_{\mathrm{CH_3\cdot}} - E^{\mathrm{b}}_{\mathrm{CH_3O\cdot}} + E^{\mathrm{b}}_{\mathrm{Ac}} - E^{\mathrm{b}}_{\mathrm{EO}}] - 0.31. \tag{2.38}$$

Because of the resemblance of the absolute value of α, β, and γ, A. Kokalj *et al.* demonstrated that ΔE^* is determined mainly by two contributions: (1) the difference between the adsorption energies of $CH_3\cdot$, $CH_3O\cdot$, and (2) the difference between the adsorption energies of the two final states, Ac and EO. A. Kokalj *et al.* [93, 53] showed that the parameters in Eq.(2.38) can estimate ΔE^* for the models of the pure metal catalysts such as Ag, Cu, Rh, and Au, and 2D-alloy of Ag/Cu alloys with an accuracy better than 0.1 eV (with RMSE and Maximum Absolute error of 0.05 and 0.07 eV, respectively), see in Fig. 2.18(a). However, employing this indicator into our NEB results shows that only the Ag(111) structure fits within the error bars obtained by A. Kokalj *et al.* When applying this indicator to the whole set of the structures, including the thin oxide layers, we find a much higher uncertainty, i.e. RMSE = 0.102 and MAE = 0.23 eV.

In order to find out an indicator able to describe all structures, we present here two different approaches to estimate the parameters in Eq.(2.37). The first is obtained by re-fitting α, γ, and C parameters over the selected structures while keeping $\alpha = \beta \neq \gamma$, in agreement with the A. Kokalj's demonstrations above. A better approximation is shown in Fig. 2.18(b) with the new parameters 0.33, 0.59, and -0.22 for α, γ, and C, respectively. The selectivity indicator is therefore given by:

$$\Delta E^* = 0.33[E^{\mathrm{b}}_{\mathrm{CH_3\cdot}} - E^{\mathrm{b}}_{\mathrm{CH_3O\cdot}}] + 0.59[E^{\mathrm{b}}_{\mathrm{Ac}} - E^{\mathrm{b}}_{\mathrm{EO}}] - 0.22. \tag{2.39}$$

Compared to the errors in the previous one, this indicator improves the accuracy so that it can predict the selectivity of catalysts within MAE = 0.17 eV, and RMSE = 0.09 eV.

The second approach for selectivity indicator improvement is based on the general expansion of ΔE^*, Eq. (2.37), where the contributions from adsorption energy of $CH_3\cdot$, $CH_3O\cdot$ radicals are considered independently. It requires fitting through whole data for four parameters α, β, γ, and C. Fig. 2.18(c) presents a good quality of the fit given by:

$$\Delta E^* = 0.25E^{\mathrm{b}}_{\mathrm{CH_3\cdot}} - 0.39E^{\mathrm{b}}_{\mathrm{CH_3O\cdot}} + 0.60[E^{\mathrm{b}}_{\mathrm{Ac}} - E^{\mathrm{b}}_{\mathrm{EO}}] - 0.46. \tag{2.40}$$

The parameters in this indicator yield the errors of RMSE = 0.07 eV and MAE = 0.15 eV. In addition, Eq.(2.40) also shows that although the binding energies of the final states, Ac and EO with the catalysts surfaces are smaller compared to those of $CH_3\cdot$, $CH_3O\cdot$, their contributions are still significant in selectivity of catalysts, which is seen through a large coefficient of γ compared to α and β. One can see that Eq.(2.40) does not depend on initial states of reactions, but transition states play the key role. In Fig. 2.14, transition states of two reactions for the formation of EO and Ac are very similar for different surface structures. Therefore although the mechanism of the reaction toward the EO formation does not go through OMC on the CuO/Ag(111) surface, the selectivity indicator still gives a good description. Furthermore, the selectivity indicator can also describe the improvement of selectivity with the amount of Cu present on Ag surface to form Ag/Cu catalyst increases. Fig. 2.18 shows that the Ag/Cu alloy structures are found mainly in the top-right corner of the figures, according to $\Delta E^* > 0$.

Overall, one can see that the new indicator in our work allows to depict well the selectivity, ΔE^*, for the both the mono-metal catalysts and the catalysts formed by thin oxide-like layers that are stable under the conditions relevant for experiments. However, we cannot fail to notice that the error in the indicator ($\sim$ 0.1 eV) is as big as the differences in ΔE^* between one structures and the other. So it gives an qualitative indication, but its predictive power is limited in the cases where $\Delta E^* \lesssim$ 0.1 eV. On the other hand, estimating the catalyst selectivity, $\Delta E^* = E^*_{\mathrm{Ac}} - E^*_{\mathrm{EO}}$, through evaluating the computationally simpler quantities such as binding energies, is very useful in saving computational time. It allows us to predict the selectivity of catalysts without doing further expensive NEB calculations.

2.3.3.4 Ag/Cu alloy structures as function of Cu content

In the previous section, we showed that the Osub(fcc)+CuO/Ag(111) structure formed by O^{sub} on CuO/Ag(111) has a higher selectivity toward the formation of EO compared to a pure Ag(111) surface. However, as shown in the surface phase diagram of (111) surface, Fig. 2.9, Osub(fcc)+CuO/Ag(111) is thermodynamically favorable only at high oxygen pressure condition, i.e. $p_{O_2} = 10^2$ atm, and $T = 600$ K. The question is how to stabilize this O^{sub} under the first CuO layer so that it can be available for catalysis in the conditions relevant for experimental regime.

Due to the relative strength of binding energy between Cu-O compared to Ag-O bonds, in an oxygen atmosphere Cu atoms in Ag/Cu catalysts tend to segregate to the catalyst surface and bind with the oxygen, forming the thin CuO oxide layer on the top of Ag surfaces. Therefore, O^{sub} present at the interface between the CuO layer and silver layers prefers to bind to Cu atoms in the second layer more than Ag ones. If the content of Cu in the Ag/Cu alloy increases, after forming a thin copper oxide layer, Cu atoms continue to occupy the second layer to bind with O^{sub}, forming a second CuO layer on the Ag slabs that can be more stable than a single CuO layer present. O^{sub} in this case is assumed to play a role as the nucleation site for bulk oxide formation [56]. In recent studies of oxidation reactions over transition

metal such as Ru, Rh, Ag, and alloy surfaces such as NiAl(110) [126, 127, 128, 56], it has been shown that the incorporation of oxygen into sub-surface positions relates to the oxide formation on the surfaces [56, 75]. According to this evidence, the stability of the Osub(fcc)+CuO/Ag(111) structure can be increased by replacing the silver atoms in the second layer by the Cu ones.

In Fig. 2.20, we present the surface free energy, computed by Eq.(2.29) at the oxygen chemical potential $\mu_O = 0.61$ eV ($p_{O_2} = 1$ atm and $T = 600$ K), of the possible structures with respect to different Cu coverages. The content of oxygen on the surface is increased up to 2 ML. In the case of Cu content equal to 1 ML (i.e. no Cu replacing Ag in the second layer) the presence of O^{sub} is unfavorable. At lest a quarter of a monolayer in the second layer (i.e. one Cu replacing an Ag atom in the 2×2 cell) is necessary to promote the presence of O^{sub}. The calculations show that O^{sub} atoms prefer to reside right at the interface under the first CuO layer rather than on the surface or the deeper in the Ag slab (i.e. under the second Ag layer). This is due to the fact that the Cu-O bonds are energetically favorable compared to Ag-O. Fig. 2.20(a) also shows that as the number of Cu atoms replacing Ag atoms in the second layer increases, so does the number of O^{sub} atoms at the interface. In Fig. 2.19, the top-view and side-view of these stable structures at different composition of Cu atoms in the second layer is presented.

Moreover, from the phase diagram in Fig. 2.20(a), one can see that the most stable structure is the one where the formation of a full mono-layer of CuO in the first two layers takes place. O^{sub} in this structure is energetically favored to occupy the positions involved in the trilayer O-Cu-O formation, which creates a crystal similar to cuprite bulk in (111) direction [129]. This was to be expected, since at these conditions of T and p_{O_2}, the formation of bulk copper oxide is thermodynamically favorable [79, 78]. In this case, we must however bear in mind that DFT-PBE predicts CuO bulk to be a metal with an almost orthorhombic structure, while experiments have found that CuO is a strongly correlated antiferromagnetic semiconductor, with a monoclinic structure [130]. Therefore, the formation of thicker CuO oxide layers similar to CuO bulk in our work must be regarded as qualitative.

Figure 2.19: The top-view (top panel) and side-view (below panel) of the most stable structures at the given Cu surface content. In the top penal, the small red atoms represent oxygen on the first thin oxide layer, the large peru ones represent copper on the first thin oxide layer, the small dark-red ones represent sub-surface oxygen, the large sienna ones represent copper on the second layers, and the large white ones represent silver.

As shown in the previous sections, the presence of O^{sub} on the most stable Cu/Ag alloy leads to a higher catalyst selectivity toward the formation of EO compared to pure Ag. However this structure, as shown in the phase diagram, is not favorable compared to CuO/Ag(111). Replacing one Ag in second layer by one Cu atom can decrease the surface free energy of this structure, and by NEB calculations, we have found that this structure increases significantly the selectivity of catalysts toward EO formation compared to CuO/Ag(111). In Fig. 2.20(b), by employing the selectivity indicator proposed in Eq.(2.40), we presented the change of selectivity for the most stable geometries with different Cu contents. This result shows that the stable structures are highly selective, however, there is no trend found upon changing the Cu content.

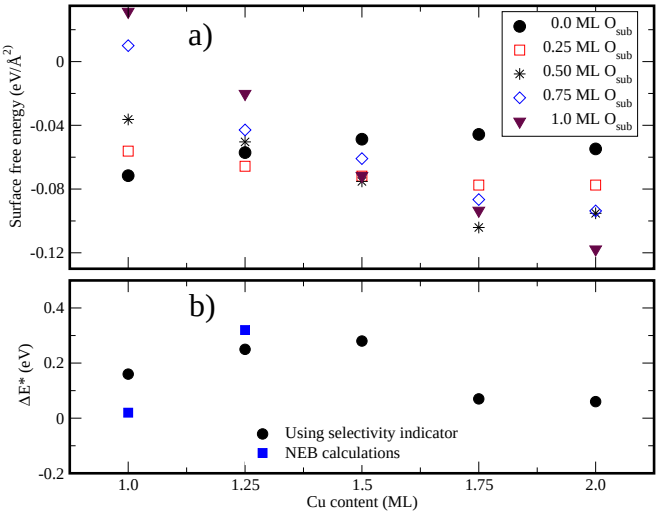

Figure 2.20: (a) Surface phase diagram showing the surface free energy at $\Delta\mu_O = -0.80$ eV ($T = 600$ K, $p_{O_2} = 1$ atm), for the structures as the function of Cu surface content and the changing of O^{sub} coverage. (b) The selectivity calculated by the indicator in Eq.(2.40) of the most stable structures at the given Cu surface contents, i.e., those having the lowest surface free energy of phase structure presented in (a). The selectivity evaluated by NEB algorithm of the structures with 1 ML and 1.25 ML Cu coverage is also presented for comparison purpose.

2.4 Conclusion

Through density functional theory (DFT) calculations and employing *ab initio* atomistic thermodynamics, we studied the ethylene epoxidation reaction toward the final Ac and EO products on the Ag-Cu alloy. The calculations are performed on the different stable structures formed on the low-index facets including (111), (100), and (100). According to results found by *in situ* X-ray photoelectron spectroscopy (XPS) experiment [77], and verified by DFT calculations [79, 78], around the temperature and pressure of interest for practical applications the stable structures of Ag-Cu alloy form a thin layer of copper oxide on the top of silver surface. The thin oxide layer structures therefore play an important role to enhance the selectivity towards the formation of EO rather than the 2D alloys which were considered in the previous works [72, 53, 93].

By considering the system to be in constrained equilibrium with both oxygen and ethylene reservoirs, we were able to identify the stable surface structures on the low-index surfaces as a function of temperature and partial pressures. We found that around values of temperature and partial pressures relevant for industrial applications, the catalyst is formed, on all three facets examined, by a thin CuO oxide-like layer on top of pure Ag. At lower temperatures or higher partial pressures, these surface structures are covered by the ethylenedioxy (EDO), where ethylene binds to the surface via two oxygen atoms. Moreover we predict that, under these conditions, on the (111) surface, sub-surface oxygen will be present at the interface between the CuO layer and the silver slab. Our calculations also indicate that around 600 K and for Cu contents below one monolayer, the (100) facet becomes dominant. At lower temperatures, where the facets are covered by EDO, the (111) facet is the dominant one. We found that OMC, a proposed common intermediate for both the selective and unselective reaction paths in pure metal catalysts, is not present on the phase diagrams of any facets under any condition of temperature and partial pressures. This is due to the considerably higher stability of the EDO intermediate compared to OMC. This could have important implications for the mechanism of reaction, because the conversion of EDO to either EO or Ac is a highly activated process.

We also studied how the reactions that convert ethylene to EO and Ac final products proceed on each of the stable surface structures. The results show that the reaction mechanism of ethylene epoxidation is influenced by the underlying surface structures, and that the reactions not always proceed through the formation of an oxametallacycle (OMC) intermediate. We also find that the geometry of the transition states is not very sensitive to the surface structure and that activation barriers and enthalpies of reaction are approximately related by the linear Brønsted-Evans-Polanyi relation. The DFT estimates of the activation barriers for the competing processes suggest that these thin Cu-O layers can enhance the selectivity toward the formation of EO, even though our calculations suggest that the improvement in the selectivity is small.

The effect of sub-surface oxygen O^{sub} on the thin oxide-like layer structures, on mechanism of reaction and on the catalyst selectivity toward the formation of

EO final product is also examined in this thesis. The calculations show that O^{sub} stabilizes OMC intermediate on CuO/Ag(111) with respect to the ethylene in the gas phase, similarly to what happens on the pure Ag(111). Furthermore, O^{sub} is found to increase the activation energy of the reaction paths from OMC toward the final products, in agreement with findings on the pure Ag surface [58]. We also found that on the pure Ag(111), the presence of O^{sub} reduces the selectivity of this structure, while this oxygen species does not affect strongly the selectivity of CuO/Ag(111). In particular, the selectivity of CuO/Ag(111) with/without O^{sub} is found to be higher than pure Ag. In contrast, the selectivity of CuO/Ag(111) depends strongly on the Cu content on the surfaces. In particular, in the presence of O^{sub} under the first CuO layer, the Cu atoms are thermodynamically favorable to segregate on the Ag-Cu alloy catalyst surface, and they tend to form the deeper oxide layers.

In order to get an insight into the role of Cu atoms in improving the selectivity of the catalyst structures, we consider the selectivity indicator proposed by A. Kokalj *et al.* [53, 93]. In this indicator, the selectivity, ΔE^*, is represented through a relation depending on the strength of C- and O-surface bonds in the OMC intermediate, and on the binding energies between the final products, Ac (E^b_{Ac}) and EO (E^b_{EO}), and the surfaces,

$$\Delta E^* \propto \alpha E^b_{CH_3\cdot} - \beta E^b_{CH_3O\cdot} + \gamma[E^b_{Ac} - E^b_{EO}]. \tag{2.41}$$

In this relation, C- and O-surface bonds are approximated as the bonds of the methyl (CH_3) and methoxy (CH_3O) radicals with the surfaces. The α, β, γ coefficients in Eq.(2.41) are estimated so that this indicator can be applied to predict for both the pure metal catalyst and surface oxide catalysts. Through the new indicator, the role of Cu to improving selectivity is interpreted. Moreover, it also allows to predict the selectivity toward the formation of EO of new catalysts, with the error of $\Delta E^* < 0.1$ eV, without performing expensive Nudged Elastic Band (NEB) calculations.

Chapter 3

Exact Exchange and RPA Correlation Energy and Potential in the Adiabatic Coupling Fluctuation-Dissipation Theory

3.1 Introduction

Through several applications, Kohn-Sham (KS) density functional theory (DFT) has been shown as the standard and convenient method for study at the atomistic scale of the ground-state properties of solid-state and molecular systems. However, DFT still has many drawbacks that reduce the accuracy of the computational results. One of the most critical elements is the evaluation of the exchange-correlation energy, $E_{\rm xc}[n(r)]$, as a functional of the electron density $n(r)$. For many years, LDA and GGA have been widely used for $E_{\rm xc}[n(r)]$, and the results have shown that these functionals usually yield a good description of the atomic equilibrium structures and vibrational properties of molecules and solids. However, these approximations notably fail to predict molecular dissociation energy within chemical accuracy $\sim$ 50 meV [131], and do not properly include van der Waals (vdW) interactions in weakly bonded systems such as noble gas molecules, solids layered materials, and bio-molecules [11]. These shortcomings originate from the lack of truly non-local correlations effects that are at the heart of the vdW interaction in LDA or GGA functionals.

During last couple of decades, high level quantum chemical methods such as Symmetry Adapted Perturbation Theory with Coupled Cluster (SAPT-CC), or Møller-Plesset (MP) perturbation theory approach, or Configuration Interaction (CI), etc. have been shown to be the most powerful methods for the description of vdW interactions, however, for large systems these approaches become rapidly computationally very demanding [132]. Therefore, this motivates us to improve the inexpensive DFT calculations so that the limitations of LDA or GGA can be corrected. One of the simplest approaches is carried out by including the attractive component C_6/R^6 of Lennard-Jones potential to the conventional density functional calculation [12]. While this approach may work fairly well for many vdW complexes such as NH_3, H_2O, CH_3F,... there is not a unique way to select the damping functions and C_6 coefficients for the systems [12]. Another approach in this field introduces a non-local correlation functional that can treat the entire range

of dispersion interactions in systems in a general and seamless fashion. However, the expression of this functional usually depends only on two-body contributions of the dispersion energy, it thus limits the accuracy of evaluation of correlation energy in larger models [133, 134]. Moreover, other schemes such as exact-exchange only, or hybrid functionals have been also applied, but they have shown a very limited success in the description of vdW interactions [135, 136].

Recently, employing the adiabatic connection fluctuation dissipation (ACFD) theorem to the calculations of E_{xc} in DFT has been considered for weakly bonded interacting systems [137, 13]. In particular, calculations using the simplest approximation in this theory, the Random Phase Approximation (RPA), for correlation energy have improved the computational accuracy compared to experiment [11]. In ACFD theorem, the calculations for the RPA correlation energy are usually carried out based on a perturbative approach with input KS orbitals calculated with the standard local and semi-local exchange-correlation energy functionals. The exchange energy, on the other hand, is evaluated in the Hartree-Fock (HF) formalism constructed from the KS orbitals. This energy is the so-called exact-exchange energy (EXX). A common name of the total energy obtained combining these two calculations is EXX/RPA.

Why can EXX/RPA overcome the problems of the weakly bonded systems? The answers are seen through the definitions of the energy functionals of EXX and RPA correlation energy. In the original formula, RPA correlation contains non-local correlation effects characteristic of vdW interactions [138]. It is well known that this functional can describe properly the long-range dependence of the correlation energy [11]. In addition, since the expression of EXX is based on the HF exchange formalism, EXX does not lead to any self-interaction errors usually found in the standard DFT with LDA and GGA exchange-correlation functionals [14]. Therefore, using EXX/RPA to compute vdW interactions is expected to yield a greater accuracy than LDA or GGA. Furthermore, compared to the other approaches using quantum chemistry such as SAPT-CC, CI, etc. EXX/RPA is less computationally intensive for large systems, since it works mainly with the KS orbitals. This makes EXX/RPA more practical for applications.

In practice, EXX/RPA formulated within ACFDT has been extensively applied to many different systems. In the beginning, RPA correlation energy has been computed for approximate models such as jellium [139], jellium slabs [140, 141], and used to study the asymptotic atom-atom vdW interaction [142]. Later, EXX/RPA calculations for more realistic systems such as diatomic molecules [138, 143, 144, 145, 16], and crystal solids [146, 147, 148], which are more demanding, have also been presented. Furthermore, the problems of molecule physisorption on surfaces, similar to the one we have seen in the previous chapter, have also been performed within EXX/RPA framework. The results of physisorption binding energies between the different molecules and surfaces show an agreement with the values measured by experiments, and are better than those obtained by LDA or GGA exchange-correlation functionals [39, 20, 19].

Attempts have been made to include EXX/RPA based on the framework of

ACFD theory into DFT. For instant, Furche *et al.* [138, 149] have introduced EXX/RPA calculations for KS equations with single-particle electronic orbitals represented by localized basis sets, and density matrices. This first approach, in principle, yields a quite expensive calculation since its computational workload scales as N^6, and as N^5 in the newest version [15]. Where N is the number of valence electrons in the system. Recently, EXX/RPA calculations within KS equations represented by PW basis set and Pseudopotential (PP) or Projector Augmented Wave (PAW) methods have been also reported by Gonze *et al.* [143], and Kresse *et al.* [146]. Where, while EXX is computed from the occupied KS orbitals, the RPA correlation energy is derived by direct diagonalization of a finite matrix of KS density-density response function. The computational workload of this method, thus, scales as N^4, faster than Furche's approaches. However, the calculations are found to be very time consuming and CPU memory limited due to cumbersome summations. In addition, the convergence of RPA correlation energy strongly depends on the numbers of PW [146]. An alternative approach in PW and PP method has been developed by Huy-Viet Nguyen *et al.* [14]. The evaluation of RPA correlation energy in this approach is based on the concept of dielectric band structures. This calculation is greatly improved since it only employs a relatively small number of eigenvalues of RPA dielectric matrix, efficiently computed by iterative density response calculations in the framework of density functional perturbation theory [14].

Despite the achievements of EXX/RPA in many applications for cohesive energy, lattice constant of bulk systems, bond lengths of molecules, and specially, the vdW interactions of the weakly bounded systems [11], this scheme also has some shortcomings in general. First, in RPA correlation energy the depth of the short-range part of the electronic correlation hole is seriously overestimated, determining an overestimation of the magnitude of the correlation energy close to the equilibrium bond length position. This problem can be corrected by introducing the so-called RPA+ scheme. The implementation of RPA+ in the calculation of some simple systems has been presented [14]. The calculated structural properties such as equilibrium bond-length, or vibrational frequency are, however, turned out to be not comparable to those computed by EXX/RPA in agreement with experiments [14]. Second, since EXX/RPA is a post-functional of KS orbitals, the computed results strongly depend on the input KS orbitals. For example with different exchange-correlation functionals or different basis sets, the final computed total energies are inconsistent [138]. It therefore requires to find ways to do self-consistent calculations for EXX/RPA energy functional so that the final results are consistent. A third problem appears in some EXX/RPA calculations for several simple molecules such as Be_2, Ca_2, N_2, Mg_2, etc [16, 145, 138]. The binding energy curves of these molecules has shown an unphysical bump at intermediate distances between the two atoms. The reason of this problem, however, has not been fully understood yet. Some studies recently proposed by Toulouse *et al.* have shown a possible solution for EXX/RPA calculation of Be_2 molecule by employing Green's function many body theory [145], while recently, in an extensive studies of different molecules, Huy-Viet Nguyen *et al.* have provided evidence that lacking self-consistent field (scf) procedure in EXX/RPA

scheme can induce this problem for Be_2 [16].

In principle, in order to carry out a scf procedure for EXX/RPA energy functional, one needs to compute the derivative of EXX/RPA with respect to the charge density to obtain the EXX/RPA potential. In practice, because EXX/RPA are explicit functionals of the KS orbitals rather than explicit functionals of the KS density (such as GGA or LDA), treatment of scf for these functionals in the DFT framework requires the so-called optimized effective potential (OEP) method to compute the corresponding effective single-particle potentials. While the OEP methods have been studied widely for EXX-only, and many different approaches of this problem have been reported for many years, applying OEP methods for both EXX and RPA correlation energies, however, has not been yet attempted. Recently, Gonze *et al.* have formally derived an expression to obtain the EXX/RPA potential based on the Sham-Schlüter equations [150], and the authors have also discussed about the asymptotic EXX/RPA potential [131]. On the other hand, U. von Barth *et al.* [151, 152, 153] have proposed a way to optimize EXX/RPA energy by employing a variational methods for functional of one-particle non-interacting-Green's functions. This approach however, has been applied just to a local basis set, and studied only for atoms so far.

This motivates us to carry out the OEP procedure with EXX/RPA energy functional. We will derive an expression for EXX/RPA self-consistent potential from EXX/RPA formalism. While the implementation for EXX potential is obtained from the framework of the OEP method applied to EXX-only, the formalism for RPA correlation potential consists of two main steps: (i) the expression of the functional derivative with respect to the KS potential of the relatively small number of eigenmodes of RPA dielectric matrix, and (ii) the use of an OEP procedure similar to EXX to find this potential. In the last part of this thesis, the implementations will be employed to study some simple molecule examples such as Be_2, H_2 and LiH.

3.2 Exact Exchange and RPA Correlation Energies in Adiabatic Connection Fluctuation-Dissipation Theory

3.2.1 Exact exchange and RPA correlation energies in ACFDT

The Adiabatic Connection Fluctuation-Dissipation (ACFD) theory [13, 28] for the determination of the exchange-correlation energy in DFT can be obtained by considering the idea of slowly turning-on the electron-electron interaction multiplied by a coupling constant λ while the ground state density of the system is kept fixed. This is ensured by a compensating variation of the external potential $v_{\text{ext}}(r,\lambda)$. When λ varies from zero to unity, the system turns from the non-interacting to the fully interacting one, while the ground state densities associated with it remains unchanged, $n(r,\lambda) = n(r,\lambda=0)$. Considering a finite value of λ, the Hamiltonian of the system will read,

$$\hat{H}(\lambda) = \hat{T} + \hat{v}_{\text{ext}}(\lambda) + \lambda\hat{V}_{\text{ee}}. \tag{3.1}$$

The total ground-state energy is evaluated as the expectation value of $\hat{H}(\lambda)$ by,

$$E^{\lambda} =< \varphi^{\lambda}[n]|T|\varphi^{\lambda}[n] > + < \varphi^{\lambda}[n]|\lambda\hat{V}_{\text{ee}}|\varphi^{\lambda}[n] > + < \varphi^{\lambda}[n]|\hat{v}^{\lambda}_{\text{ext}}(\lambda)|\varphi^{\lambda}[n] > . \tag{3.2}$$

According to Hellmann-Feynman theorem, the variation of E^{λ} with respect to change of coupling constant λ is given by:

$$\frac{\partial E^{\lambda}}{\partial\lambda} =< \varphi^{\lambda}[n]|\hat{V}_{\text{ee}}|\varphi^{\lambda}[n] > + < \varphi^{\lambda}[n]|\frac{\partial\hat{v}^{\lambda}_{\text{ext}}(\lambda)}{\partial\lambda}|\varphi^{\lambda}[n] > . \tag{3.3}$$

Therefore, one can simply obtain the total ground-state energy of the fully interacting systems, associated with $\lambda = 1$, through the integration:

$$\begin{aligned} E^{\lambda=1} =& E^{\lambda=0} + \int_0^1 d\lambda \frac{\partial E^{\lambda}}{\partial\lambda} \\ =& E^{\lambda=0} + \int \left\{v_{\text{ext}}(r,1) - v_{\text{ext}}(r,0)\right\} n(r)dr + \int_0^1 d\lambda < \varphi^{\lambda}[n]|\hat{V}_{\text{ee}}|\varphi^{\lambda}[n] >. \end{aligned} \tag{3.4}$$

Here, one can identify $E^{\lambda=0}$ with the KS auxiliary system:

$$E^{\lambda=0} = T_{\text{KS}}[n] + \int V_s(r)n(r)dr, \tag{3.5}$$

where $v_{\text{ext}}(r,0) = V_s(r)$. On the other hand, using KS decomposition of the interacting energy functional the energy of the interacting system can be written as:

$$E^{\lambda=1} = T_{\text{KS}}[n] + E_{\text{Hxc}}[n] + \int v_{\text{ext}}(r,\lambda=1)n(r)dr. \tag{3.6}$$

Inserting Eq.(3.5) into Eq.(3.4), and comparing with Eq.(3.6), one can finally write down the expression for Hartree and exchange-correlation energy in the fully interacting systems as:

$$E_{\rm Hxc}[n] = \int_0^1 d\lambda < \varphi^\lambda | \hat{V}_{\rm ee}(r) | \varphi^\lambda >. \tag{3.7}$$

Since we do not have an explicit expression for $\{\varphi^\lambda\}$, the expansion in Eq.(3.7) will be connected to the response function of the system. We first note that the operator $\hat{V}_{\rm ee}$ of electron-electron integration can be written as

$$\hat{V}_{\rm ee} = \frac{1}{2}\int dr \int dr' \frac{1}{|r-r'|}\{\hat{n}(r)\hat{n}(r) - \hat{n}(r)\delta(r-r')\} \tag{3.8}$$

where, the density operator is $\hat{n}(r) = \sum_i \delta(r-r_i)$, whose expectation value is $n(r) = \sum_i |\varphi_i(r)|^2$. Therefore, Eq.(3.7) can be re-expressed as:

$$E_{\rm Hxc}[n] = \frac{1}{2}\int_0^1 d\lambda \int dr \int dr' \frac{1}{|r-r'|}\{< \varphi^\lambda | \hat{n}(r)\hat{n}(r) | \varphi^\lambda > - n(r)\delta(r-r')\}. \tag{3.9}$$

Using the density fluctuation operator defined by

$$\delta\hat{n}(r) = \hat{n}(r) - n(r) \tag{3.10}$$

and applying Fluctuation-Dissipation theorem [137], the connection between $< \varphi^\lambda | \hat{n}(r)\hat{n}(r) | \varphi^\lambda >$ and the density-density response function at interaction strength λ, $\chi_\lambda(r, r', iu)$, can be established as:

$$< \varphi^\lambda | \hat{n}(r)\hat{n}(r) | \varphi^\lambda >= n(r)n(r) - \int_0^\infty \frac{du}{\pi}\chi_\lambda(r, r', iu). \tag{3.11}$$

Inserting the expression in Eq.(3.11) into Eq.(3.9), one obtains:

$$\begin{aligned} E_{\rm Hxc}[n] = &-\frac{1}{2}\int_0^1 d\lambda \int dr dr' \frac{1}{|r-r'|}\{\int_0^\infty \frac{du}{\pi}\chi_\lambda(r, r', iu) + n(r)\delta(r-r')\} \\ &+ \frac{1}{2}\int_0^1 d\lambda \int dr dr' \frac{n(r)n(r')}{|r-r'|}, \end{aligned} \tag{3.12}$$

while the later term in the above formula is the Hartree energy one, the former represents the exchange-correlation energy.

$$\begin{aligned} E_{\rm xc}[n] =& E_{\rm x}[n] + E_{\rm c}[n] \\ =& -\frac{1}{2}\int_0^1 d\lambda \int dr dr' \frac{1}{|r-r'|}\{\int_0^\infty \frac{du}{\pi}\chi_\lambda(r, r', iu) + n(r)\delta(r-r')\}. \end{aligned} \tag{3.13}$$

By adding and subtracting the density-density response function $\chi_0(r, r', iu)$ of the non-interacting KS system into Eq.(3.13), the exchange energy can be obtained:

$$E_{\rm x} = -\frac{1}{2}\int_0^1 d\lambda \int dr dr' \frac{1}{|r-r'|}\{\frac{1}{\pi}\int_0^\infty \chi_0(r, r'; iu)du + \delta(r-r')n(r)\}, \tag{3.14}$$

while the correlation energy is expressed as:

$$E_{\rm c} = -\frac{1}{2\pi}\int_0^1 d\lambda \int dr dr' \frac{1}{|r-r'|}\{\int_0^\infty \big(\chi_\lambda(r,r';iu) - \chi_0(r,r';iu)\big)du\}. \quad (3.15)$$

Using the known expression for the density-density non-interacting response function, the frequency integration in Eq.(3.14) can be done explicitly and the exchange energy can be shown to have the usual Hartree-Fock expression evaluated with the K-S orbitals.

$$E_{\rm x} = -\frac{e^2}{2}\int dr dr' \frac{|\sum_i^{occ}\varphi_i^*(r)\varphi_i(r')|^2}{|r-r'|}. \quad (3.16)$$

The correlation energy, Eq.(3.15), can be written in a more compact form assuming a matrix notation for the response functions and the coulomb interaction $v_{\rm c} = \frac{e^2}{|r-r'|}$, and spatial integrals are replaced by matrix multiplication and trace operation:

$$E_{\rm c} = -\frac{1}{2\pi}\int_0^1 d\lambda \int_0^\infty du {\rm Tr}\{v_{\rm c}[\chi_\lambda(iu) - \chi_0(iu)]\}. \quad (3.17)$$

From Eq.(3.17), one can see that the formula for the correlation energy within ACFD theory are estimated through the traces of $v_{\rm c}\chi_0$ and $v_{\rm c}\chi_\lambda$, which can be evaluated simply by summing up their eigenvalues. Moreover, based on the framework of time-dependent density functional theory, the relation between χ_λ and χ_0 can be established by the Dyson-like equation,

$$\chi_\lambda(r,r',iu) = \chi_0(r,r';iu) + \int \chi_0(r,r_1;iu)\big[\lambda v_{\rm c}(r_1,r_2) + f_{\rm xc}^\lambda(r_1,r_2;iu)\big]\chi_\lambda(r_2,r',iu)dr_1dr_2, \quad (3.18)$$

or in matrix form

$$\chi_\lambda = \chi_0 + \chi_0(\lambda v_{\rm c} + f_{\rm xc}^\lambda)\chi_\lambda, \quad (3.19)$$

where the exchange-correlation kernel $f_{\rm xc}^\lambda = \frac{\delta v_{\rm xc}^\lambda(r)}{\delta n(r')}$ usually is approximated, and within RPA, $f_{\rm xc}^\lambda(iu) = 0$.

3.2.2 RPA Correlation Energies: an iterative diagonalization of dielectric function approach

From the explicit expression for xc energy, one can see that while the evaluation of the Exact Exchange energy in Eq.(3.16) can be calculated easily as long as the KS orbitals are known, calculation of RPA correlation energy in Eq.(3.17) needs more effort since the eigenvalue spectra of the response functions at finite λ and $\lambda = 0$, χ_λ and χ_0, have to be evaluated. In the existing implementation for RPA correlation energy, the eigenvalue problems are usually treated by applying standard diagonalization methods to the explicit χ_0 expression.

$$\chi_0(r, r', iu) = 2\sum_{i,j}(f_i - f_j)\frac{\varphi_i^*(r)\varphi_j(r)\varphi_j^*(r')\varphi_i^*(r')}{\varepsilon_i - \varepsilon_j + iu}, \tag{3.20}$$

where one needs to calculate all occupied and unoccupied KS orbitals, $\{\varphi_i(r)\}$, and eigenvalues, ε_i, and then to solve the Dyson equation in order to obtain the solutions for $\chi_\lambda(iu)$. This approach shows several shortcomings in PW pseudopotential DFT calculations since it requires the consideration of a large number of unoccupied states in order to reach convergence. Here we review another approach proposed recently by Huy-Viet Nguyen at SISSA [154] and other [155, 156], which is based on an efficient iterative diagonalization of the response function based on Density Functional Perturbation Theory (DFPT), whose applications only involves occupied KS orbitals. The method can be introduced by considering the following generalized eigenvalue problems for χ_0 and χ_λ:

$$\chi_0|\omega_\alpha >= a_\alpha v_c^{-1}|\omega_\alpha >, \tag{3.21}$$

and

$$\chi_\lambda|z_\alpha^\lambda >= b_\alpha^\lambda v_c^{-1}|z_\alpha^\lambda >, \tag{3.22}$$

where $\{\omega_\alpha\}$,$\{a_\alpha\}$ and $\{z_\alpha^\lambda\}$,$\{b_\alpha^\lambda\}$ are eigenpairs of the generalized eigenvalue problems (all the quantities depend implicitly on the imaginary frequency iu). The correlation energy at a given interacting coupling strength λ can be defined through the sets of eigenvalues $\{a_\alpha\}$ and $\{b_\alpha^\lambda\}$ as:

$$E_c^\lambda = -\frac{1}{2\pi}\int_0^1 d\lambda \int_0^\infty du \sum_\alpha \{b_\alpha^\lambda(iu) - a_\alpha(iu)\}. \tag{3.23}$$

On the other hand, at the RPA level, the Dyson-like equation defining χ_λ can be rewritten as:

$$\chi_\lambda = \chi_0 + \lambda\chi_0 v_c \chi_\lambda. \tag{3.24}$$

The response functions and Coulomb operators are well defined since they are symmetric and positive (v_c) or negative (χ_0, χ_λ) definite, they are, therefore, invertible. The Dyson equation can be recast in the form

$$\chi_0^{-1} = \chi_\lambda^{-1} + \lambda v_c. \tag{3.25}$$

A similar eigenvalue problem for the inverted response functions, χ_0^{-1} and χ_λ^{-1}, can be defined as:

$$\chi_0^{-1}|\widetilde{\omega}_\alpha>=\frac{1}{a_\alpha}v_c|\widetilde{\omega}_\alpha>, \tag{3.26}$$

and

$$\chi_\lambda^{-1}|\widetilde{z}_\alpha^\lambda>=\frac{1}{b_\alpha^\lambda}v_c|\widetilde{z}_\alpha^\lambda>. \tag{3.27}$$

Using the relation in Eq.(3.25), between χ_0 and χ_λ, and coupling with Eqs.(3.26 and 3.27), one can deduce the relation between the eigenvalues of χ_0 and χ_λ, which reads:

$$b_\alpha^\lambda=\frac{a_\alpha}{1-\lambda a_\alpha}. \tag{3.28}$$

This simple relation allows to perform the λ coupling-constant integration in Eq.(3.23) analytically, which leads to the final expression for RPA correlation energy,

$$E_c=-\frac{1}{2\pi}\int_0^\infty du\sum_\alpha\{a_\alpha(iu)+\ln[1-a_\alpha(iu)]\}. \tag{3.29}$$

The spectrum of the eigenvalue in Eq.(3.21) is negative. The eigenvalues are closely related to those of the RPA dielectric matrix, $\varepsilon^{\mathrm{RPA}}=1-v_c\chi_0$, which have been considered in the past in the so-called dielectric band structure [157]. Inspection of the spectra of dielectric band structures shows that only a small fraction of the eigenvalues $\{\varepsilon_\alpha^{\mathrm{RPA}}\}$ is significantly different from 1 while the large majority is ~ 1, which means that RPA correlation energy in Eq.(3.29) will be dominated by a relative small number of eigenvalues of $v_c\chi_0$ significantly different from zero. This allows to calculate only these lowest-lying eigenvalues in Eq.(3.21), and in our approach, instead of constructing a full matrix to be diagonalized by standard techniques, a very efficient iterative diagonalization technique is employed.

It is convenient to manipulate the generalized eigenvalue problem in Eq.(3.21) so that it is transformed in an ordinary eigenvalue problem of an Hermitian operator $\tilde{\chi}_0$ simply related to $v_c\chi_0$ by:

$$\tilde{\chi}_0=v_c^{1/2}\chi_0 v_c^{1/2}, \tag{3.30}$$

which has the same eigenvalue $\{a_\alpha\}$ as those of $v_c\chi_0$, but different eigenvectors, $\{\gamma_\alpha\}$ instead of $\{\omega_\alpha\}$. This transformation has been widely used in previous literature about RPA dielectric function [158, 157, 159]. Eq.(3.21) finally is rewritten as,

$$\tilde{\chi}_0|\gamma_\alpha>=a_\alpha|\gamma_\alpha>. \tag{3.31}$$

In order to compute the lowest-lying eigenvalues $a_\alpha(iu)$ of the eigenvalue problems derived in Eq.(3.31), we employ Davidson iterative diagonalization algorithm starting from a set of random trial eigenpotentials much in the same way as it is done in the iterative diagonalization of KS-equations. In this algorithm, the first order variation of the KS density, Δn_α, induced by a perturbing trial potential, ΔV_α, through the non-interacting response function, χ_0, is computed via the Density Functional Perturbation Theory (DFPT) procedure. In this way, the matrix

elements on the right hand side of Eq.(3.31), $\tilde{\chi}_0^{\alpha\beta}$, are constructed. Diagonalizing this matrix results in a new set of approximate eigenpotentials that is used to generate correction vectors for the next iterative cycle. The threshold for convergence in this diagonalization procedure is chosen smaller than $10^{-6}au$ for the lowest-lying eigenvalues.

We give now some details for the approach for time-dependence DFPT that is used to find the density response induced by the dynamic perturbing potential, $\Delta V(r,t)$, which is employed in the iterative diagonalization. Let's consider the KS time-dependent Hamiltonian $\hat{H}(r,t)$, and the general time-dependent KS equations,

$$i\hbar\frac{\partial\psi_{k,v}^0(r,t)}{\partial t} = \hat{H}(r,t)\psi_{k,v}^0(r,t) \tag{3.32}$$

where, the Hamiltonian is a functional of the density. In the unperturbed, stationary, case, the time dependent wave functions $\{\psi_{k,v}^0(r,t)\}$ can be obtained by multiplication between a phase factor and the static KS wave functions $\varphi_{k,v}^0(r)$ that are known as the solution of the static KS equations in Eq.(1.14),

$$\psi_{k,v}^0(r,t) = \varphi_{k,v}^0(r)e^{-i\varepsilon_{k,v}t}. \tag{3.33}$$

Let's consider now a perturbing potential, $\Delta V(r;t)$, that can be chosen to have a well defined spatial- and time-dependence, in which q and iu are wave vectors and imaginary frequency, respectively. The explicit formula for this dynamical potential reads,

$$\Delta V(r;t) = [\Delta V(r)e^{iqr} + \Delta V^*(r)e^{-iqr}]e^{ut}, \tag{3.34}$$

with $\Delta V(r)$ being a lattice-periodic potential. With this definition, the perturbing potential is at any time real-valued and the KS Hamiltonian in Eq.(3.32) is hermitian. Adding this potential to the KS system, the wave functions change from the ground state $\psi_{k,v}^0(r,t)$ to the perturbed $\psi_{k,v}(r,t)$ which are given by the ground state contribution and a first-order correction,

$$\psi_{k,v}(r;t) = \psi_{k,v}^0(r;t) + \Delta\psi_{k,v}(r;t), \tag{3.35}$$

where $\Delta\psi_{k,v}(r;t)$ can be written in the following form where the phase factors of the perturbing potentials are explicitly accounted for:

$$\Delta\psi_{k,v}(r;t) = [\Delta\varphi_{k,v}^+(r)e^{iqr} + \Delta\varphi_{k,v}^-(r)e^{-iqr}]e^{-i\varepsilon_{k,v}t}e^{ut}. \tag{3.36}$$

In order to obtain information on the non-interacting response function, χ_0, we need to calculate the density variation induced by $\Delta V(r;iu)$,

$$\Delta n(r;iu) = \int \chi_0(r,r';iu)\Delta V(r';iu)dr'. \tag{3.37}$$

This density variation can be obtained from the first-order variation of the KS

wave functions $\Delta\psi_{k,v}(r;t)$ presented in Eq.(3.36):

$$\begin{aligned}\Delta n(r;t) &= \sum_{k,v} \psi^{0*}_{k,v}(r;t)\Delta\psi_{k,v}(r;t) + \Delta\psi^{*}_{k,v}(r;t)\psi^{0}_{k,v}(r;t) \\ &= \sum_{k,v} \big[\varphi^{0*}_{k,v}(r)\Delta\varphi^{+}_{k,v}(r)e^{iqr} + \varphi^{0*}_{k,v}(r)\Delta\varphi^{-}_{k,v}(r)e^{-iqr} \\ &\quad + \Delta\varphi^{+*}_{k,v}(r)\varphi^{0}_{k,v}(r)e^{-iqr} + \Delta\varphi^{-*}_{k,v}(r)\varphi^{0}_{k,v}(r)e^{iqr}\big]e^{ut}.\end{aligned} \tag{3.38}$$

Grouping terms having the same time- and space-phase factors, one obtains the following expression for the density response,

$$\begin{aligned}\Delta n(r;t) = \sum_{k,v}\Big[&\big[\varphi^{0*}_{k,v}(r)\Delta\varphi^{+}_{k,v}(r) + \varphi^{0}_{k,v}(r)\Delta\varphi^{-*}_{k,v}(r)\big]e^{iqr} \\ &+ \big[\varphi^{0}_{k,v}(r)\Delta\varphi^{+*}_{k,v}(r) + \varphi^{0}_{k,v}(r)\Delta\varphi^{-}_{k,v}(r)\big]e^{-iqr}\Big]e^{ut},\end{aligned} \tag{3.39}$$

which can be set in the compact expression:

$$\Delta n(r;iu) = \Delta n(r)e^{iqr} + \Delta n^{*}(r)e^{-iqr}, \tag{3.40}$$

where

$$\Delta n(r) = \sum_{k,v} \varphi^{0*}_{k,v}(r)\Delta\varphi^{+}_{k,v}(r) + \varphi^{0}_{k,v}(r)\Delta\varphi^{-*}_{k,v}(r) \tag{3.41}$$

and

$$\Delta n^{*}(r) = \sum_{k,v} \varphi^{0}_{k,v}(r)\Delta\varphi^{+*}_{k,v}(r) + \varphi^{0*}_{k,v}(r)\Delta\varphi^{-}_{k,v}(r). \tag{3.42}$$

The first-order variation of wave functions, $\Delta\varphi^{+}_{k,v}(r)$ and $\Delta\varphi^{-}_{k,v}(r)$ can be obtained from Time-Dependent Perturbation Theory. Starting from the perturbed time-dependent Schrödinger equations:

$$\big[\hat{H}_{\mathrm{KS}}(r) + \Delta V(r;t)\big]\psi_{kv}(r;t) = i\frac{\partial}{\partial t}\psi_{kv}(r;t). \tag{3.43}$$

The wave function correction is introduced

$$\big[\hat{H}_{\mathrm{KS}}(r) + \Delta V(r;t)\big](\psi^{0}_{kv}(r;t) + \Delta\psi_{kv}(r;t)) = i\frac{\partial}{\partial t}(\psi^{0}_{kv}(r;t) + \Delta\psi_{kv}(r;t)). \tag{3.44}$$

By substituting the definitions of Eqs.(3.34 and 3.36) into Eq.(3.44), and keeping only the linear-order terms, one ends up with the following two equations for $\Delta\varphi^{+}_{k,v}(r)$ and $\Delta\varphi^{-}_{k,v}(r)$,

$$[\hat{H}_{\mathrm{KS}}(r) - (\varepsilon_{k,v} + iu)]\Delta\varphi^{+}_{k,v}(r) = -\Delta V(r)\varphi^{0}_{k,v}(r) \tag{3.45}$$

and

$$[\hat{H}_{\mathrm{KS}}(r) - (\varepsilon_{k,v} + iu)]\Delta\varphi^{-}_{k,v}(r) = -\Delta V^{*}(r)\varphi^{0}_{k,v}(r). \tag{3.46}$$

The presence of a finite value for the imaginary frequency iu prevents these equations to become singular. In the practical implementation, a projector P_c on the unoccupied manifold is introduced which ensures that the linear systems are non-singular even in the limit for $iu \to 0$:

$$[\hat{H}_{\rm KS}(r) + \alpha P_{\rm v} - (\varepsilon_{k,v} + iu)]\Delta\varphi^{+}_{k,v}(r) = -P_{\rm c}\Delta V(r)\varphi^{0}_{k,v}(r), \tag{3.47}$$

and

$$[\hat{H}_{\rm KS}(r) + \alpha P_{\rm v} - (\varepsilon_{k,v} + iu)]\Delta\varphi^{-}_{k,v}(r) = -P_{\rm c}\Delta V^{*}(r)\varphi^{0}_{k,v}(r). \tag{3.48}$$

Although these equations are similar to the ones of static DFPT [18], $iu = 0$, in which solutions of the linear equations can be obtained directly by iterative methods such as conjugate gradient, at finite iu the right hand sides of Eqs.(3.47 and 3.48) are non-Hermitian operators, thus a more general algorithm such as bi-conjugate gradient must be used. In our implementation, we choose the efficient bi-CGSTAB algorithm [160], that is stable and shows fast convergence.

We finally discuss the calculation of the eigenvalues of Eq.(3.31) once the iterative diagonalization is converged, that is at the last step of the iterative diagonalization with $\Delta V(r, iu) \to \Delta V_\alpha(r, iu)$. In practice, the trial potentials, $\Delta V(r)$, is chosen as the orthonormal basis set during the iterative procedure, therefore at convergence the $\widetilde{\chi}_0(iu)$ matrix is diagonal. The diagonal elements in this case are identical to the eigenvalues, and are evaluated by,

$$a_\alpha(iu) = \widetilde{\chi}_{\alpha\alpha}(iu) =< \Delta V_\alpha|\chi_0(iu)|\Delta V_\alpha > . \tag{3.49}$$

By comparing the results with the definitions in Eqs.(3.30 and 3.31), one has $|\Delta V_\alpha >= v_{\rm c}^{1/2}|\gamma_\alpha >$. The density variation in Eq.(3.41) induced by this potential is:

$$|\Delta n_\alpha >= \chi_0(iu)|\Delta V_\alpha >, \tag{3.50}$$

which can be obtained from the DFPT procedure introduced above. Therefore, the eigenvalues $\{a_\alpha\}$ can be represented in the form:

$$a_\alpha(iu) = \widetilde{\chi}_{\alpha\alpha}(iu) =< \Delta V_\alpha|\Delta n_\alpha >= \sum_{k,v,\sigma} < \Delta\varphi^{\sigma}_{v}|\Delta V^{*}_{\alpha}|\varphi_v >; \quad \sigma = \pm. \tag{3.51}$$

This formulation will turn to be useful in the definition of the functional derivative of $\{a_\alpha\}$ needed for the calculation of the correlation potential.

3.3 Exact Exchange and RPA Correlation Potentials: An Optimized Effective Potential Approach

In chapter 1, we described how to optimize the total energy of the KS system, $E_{\rm KS}$, dealing with well known approximations for exchange and correlation energy, $E_{\rm xc}[n(r)]$, such as LDA and GGA. However, in cases where $E_{\rm xc}[\{\varphi_i\}]$ depends explicitly on the KS orbitals such as for the Exact Exchange and RPA correlation energy, the optimization of $E_{\rm KS}$ turns into a more involved problem, which is termed Optimized Effective Potentials (OEP). In this problem, one tries to find an effective local-potential, $V_{\rm OEP}$ that is able to minimize the $E_{\rm KS}$. Mathematically, it is equivalent to two minimization conditions. First, the $E_{\rm KS}$ that is solved by the general KS equations, Eqs.(1.14-1.17), at the ground state should be stationary with respect to this effective potential, or:

$$\frac{\delta E_{\rm KS}[n(r),\varphi_i(r)]}{\delta V_s(r)}|_{V_s=V_{\rm OEP}}=0. \tag{3.52}$$

Here, $n(r)=\sum_i|\varphi_i(r)|^2$ is the ground state density of the KS systems. By using the chain rule for functional derivative, this condition is found equivalent to the H-K variational principle, introduced in section 1.2.2,

$$0=\frac{\delta E_{\rm KS}}{\delta V_s}=\int\frac{\delta E_{\rm KS}}{\delta n(r')}\frac{\delta n(r')}{\delta V_s(r)}dr'^3, \tag{3.53}$$

where for simplicity, we employ a short notation $E_{\rm KS}$ rather than $E_{\rm KS}[n(r),\varphi_i(r)]$.

Secondly, the set of KS orbitals $\{\varphi_i(r)\}$ employed above are the solutions of the KS equations for the non-interacting electrons moving in the effective potential $V_{\rm OEP}(r)$:

$$[-\frac{\hbar^2}{2m}\nabla^2+V_{\rm OEP}(r)]\varphi_i(r)=\varepsilon_i\varphi_i(r). \tag{3.54}$$

Similar to the expansion for KS formulation proposed in section 1.2.2, one can obtain the local effective potential in Eq.(3.54) at convergence through the relation:

$$V_{\rm OEP}(r)=v_{\rm ext}(r)+\int\frac{n(r')}{|r-r'|}dr'+\frac{\delta E_{\rm xc}}{\delta n(r)}. \tag{3.55}$$

In this equation, the first two terms are well known as external (ion-e) potential and Hartree potential, respectively. The last term, known as exchange-correlation potential, however, depends on the type of approximations for $E_{\rm xc}$. If $E_{\rm xc}$ is a functional of density such as LDA or GGA, the potential can be obtained directly by numerical or analytical functional derivation. In the case of EXX/RPA correlation energy, $E_{\rm xc}$ is explicitly expanded through KS orbitals instead of density, thus its functional derivative with respect to density can not be calculated. The aim of OEP procedure is to look for an efficient method to compute $v_{\rm xc}=\delta E_{\rm xc}/\delta n(r)$ as accurately as possible, and once $v_{\rm xc}$ is known, the OEP procedure can optimize $E_{\rm KS}$ of the systems [17]. The approach for this problem in our work will be generalized

in two steps: the first one that deals with the functional derivative of $E_{\rm xc}$ energy with respect to the KS variational potential, then, in the second one, this derivative is used to construct the approximate $v_{\rm xc}(r)$, and $V_{\rm OEP}(r)$ potentials. These two steps are performed in the self-consistent procedure so that the updated potentials in the next cycle can be optimized with respect to the previous ones, and the total energy, E, is minimized. The detailed expressions of these steps are presented in the follows.

3.3.1 A Derivation for Exact exchange and RPA correlation potentials

As presented in Eq.(3.16) and in section 3.2.2, the explicit expression for exact exchange, $E_{\rm x}^{\rm EXX}$, and RPA correlation, $E_{\rm c}^{\rm RPA}$, energies have been established. The potentials associated with these energies are defined by the functional derivative of the energies with respect to the density $n(r)$,

$$v_{\rm xc}(r) = \frac{\delta E_{\rm xc}[\{\varphi_i\}]}{\delta n(r)} = \frac{\delta E_{\rm x}^{\rm EXX}}{\delta n(r)} + \frac{\delta E_{\rm c}^{\rm RPA}}{\delta n(r)}. \tag{3.56}$$

Applying the chain rule for functional derivatives, we obtain the expression:

$$v_{\rm xc}(r) = \int \{\frac{\delta E_{\rm x}^{\rm EXX}}{\delta V_s(r')} + \frac{\delta E_{\rm c}^{\rm RPA}}{\delta V_s(r')}\}\frac{\delta V_s(r')}{\delta n(r)}dr' = \int \{\delta n_{\rm c}(r') + \delta n_{\rm x}(r')\}\frac{\delta V_s(r')}{\delta n(r)}dr', \tag{3.57}$$

which allows to calculate the potentials by estimating the variation of the exchange-correlation energy contributions with respect to the perturbing KS potential. Where we defined two notations $\delta n_{\rm x}(r)$ and $\delta n_{\rm c}(r)$ to represent for $\delta E_{\rm x}^{\rm EXX}/\delta V_s(r)$ and $\delta E_{\rm c}^{\rm RPA}/\delta V_s(r')$, respectively. The last term, $\frac{\delta V_s(r')}{\delta n(r)} = \chi_0^{-1}(r,r')$, is the inverse of the density-density response function. Evaluation for this quantity is very difficult since one often needs for $\chi_0(r,r')$ a very large matrix. In section 3.3.2 of this thesis, we will discuss how to compute it efficiently and accurately. Meanwhile, in this section we present the derivation for the functional derivatives, $\delta E_{\rm x}^{\rm EXX}/\delta V_s(r)$ and $\delta E_{\rm c}^{\rm RPA}/\delta V_s(r)$.

3.3.1.1 Functional derivative of exact exchange energy

The exact exchange energy can be written in terms of the KS orbitals as:

$$E_{\rm x}[\{\varphi_v\}] = -\frac{e^2}{2}\sum_{vv'}^{occ}\int\int drdr'\frac{\varphi_v^*(r)\varphi_v(r')\varphi_{v'}^*(r')\varphi_{v'}(r)}{|r-r'|}. \tag{3.58}$$

Its functional derivative with respect to V_s can be determined explicitly as:

$$\delta n_{\rm x}(r) = \frac{\delta E_{\rm x}[\{\varphi_v\}]}{\delta V_s(r)} = \sum_{v}^{occ}\int dr'[\frac{\delta E_{\rm x}[\{\varphi_v\}]}{\delta\varphi_v(r')}.\frac{\delta\varphi_v(r')}{\delta V_s(r)} + cc\ldots]. \tag{3.59}$$

Where we have:

$$\frac{\delta E_{\mathrm{x}}[\{\varphi_v\}]}{\delta\varphi_v(r)} = -e^2 \sum_{v'}^{occ} \int dr' \frac{\varphi_v^*(r)\varphi_{v'}(r')\varphi_{v'}^*(r')}{|r-r'|}. \tag{3.60}$$

The functional derivative of KS orbital with respect to variation of KS potential, δV_s, can be obtained from first-order perturbation theory,

$$\frac{\delta\varphi_v(r)}{\delta V_s(r')} = \sum_{n\neq v}^{\infty} \varphi_n(r) \frac{\varphi_n^*(r')\varphi_v(r')}{\varepsilon_v - \varepsilon_n}. \tag{3.61}$$

Here, n index stands for conduction or valence bands. On the other hand, in the sum over all the occupied orbitals in $\delta n_{\mathrm{x}}(r)$, Eq.(3.59), the valence contribution vanishes. We, therefore, get the final formulation of $\delta n_{\mathrm{x}}(r)$ as:

$$\delta n_{\mathrm{x}}(r) = -e^2 \sum_{v,v',c} \int dr' dr'' \frac{\varphi_v^*(r')\varphi_{v'}(r')\varphi_{v'}^*(r'')\varphi_c(r'')}{|r'-r''|} \frac{\varphi_c^*(r)\varphi_v(r)}{\varepsilon_v - \varepsilon_c}. \tag{3.62}$$

The Hartree-Fock exchange operator built with KS orbitals in real space is an integral operator with the kernel:

$$V_{\mathrm{x}}^{\mathrm{NL}}(r,r') = -e^2 \sum_{v}^{occ} \frac{\varphi_v(r)\varphi_v^*(r')}{|r-r'|}. \tag{3.63}$$

Substituting Eq.(3.63) into Eq.(3.62), one can get:

$$\delta n_{\mathrm{x}}(r) = \sum_{v,c} < \varphi_v | V_{\mathrm{x}}^{\mathrm{NL}} | \varphi_c > \frac{\varphi_c^*(r)\varphi_v(r)}{\varepsilon_v - \varepsilon_c}, \tag{3.64}$$

where $< r|\varphi_c >= \varphi_c(r)$ represent the unoccupied conduction-band KS orbitals.

This expansion can be represented in the simple form:

$$\delta n_{\mathrm{x}}(r) = \sum_{v}^{occ} \varphi_v^*(r)\Delta\varphi_v(r) \tag{3.65}$$

in which, the first-order variation of KS wave function,$\Delta\varphi_v(r)$, is calculated by solving the linear DFPT equation [18]:

$$[\hat{H}_{\mathrm{KS}} + \alpha P_{\mathrm{v}} - \varepsilon_v]\Delta\varphi_v(r) = -(1-P_{\mathrm{v}})V_{\mathrm{x}}^{\mathrm{NL}}\varphi_v(r). \tag{3.66}$$

3.3.1.2 Functional derivative of RPA correlation energy

The RPA-correlation energy expression is given in section 3.2.2 as:

$$E_{\mathrm{c}}^{\mathrm{RPA}} = -\frac{1}{2\pi}\int_0^{\infty} du \sum_{\alpha} a_\alpha(iu) + \ln(1-a_\alpha(iu)). \tag{3.67}$$

Similar to the case of $E_{\rm x}^{\rm EXX}$, the variation of $E_{\rm c}^{\rm RPA}$ with respect to the perturbing KS potential, δV_s, is defined by,

$$\delta n_{\rm c}(r) = \frac{\delta E_{\rm c}^{\rm RPA}}{\delta V_s(r)} = \frac{1}{2\pi}\int du \sum_\alpha \frac{a_\alpha}{1-a_\alpha}\frac{\delta a_\alpha}{\delta V_s(r)} \tag{3.68}$$

where, $\{a_\alpha\}$ are solutions in the generalized eigenvalues problem, Eq.(3.31). This derivation shows that the functional derivative of $E_{\rm c}^{\rm RPA}$ requires the calculation of the functional derivative of the eigenvalues a_α with respect to δV_s. Taking the expression for the eigenvalues with respect to the converged eigenvectors in Eq.(3.49), one can obtain $\delta a_\alpha/\delta V_s(r)$,

$$\frac{\delta a_\alpha}{\delta V_s(r)} =< \Delta V_\alpha|\frac{\delta\chi_0(iu)}{\delta V_s(r)}|\Delta V_\alpha >=< \Delta V_\alpha|\frac{\delta\Delta n_\alpha(r',iu)}{\delta V_s(r)} > \tag{3.69}$$

where, $\Delta n_\alpha(r;iu) = \int \chi_0(r,r';iu)\Delta V_\alpha(r';iu)dr'^3$. Comparing to the explicit formula of $\{a_\alpha\}$ in Eq.(3.51), the variation of a_α can be obtained as

$$\delta a_\alpha = \sum_v < \delta\varphi_v|\Delta V_\alpha^*|\Delta\varphi_v^\pm > + < \varphi_v|\Delta V_\alpha^*|\delta\Delta\varphi_v^\pm >. \tag{3.70}$$

In this formula, $|\delta\varphi_v(r) >$ is the first-order variation of KS orbitals induced by the static perturbing potential, $\delta V_s(r)$, which is obtained by solving the first-order perturbation equations,

$$[H_{\rm KS} - \varepsilon_v]|\delta\varphi_v > +[\delta V_s - \delta\varepsilon_v]|\varphi_v >= 0, \tag{3.71}$$

where, the first-order correction of KS eigenvalues are given by,

$$\delta\varepsilon_v =< \varphi_v|\delta V_s|\varphi_v >, \tag{3.72}$$

and the conduction-band projected wave function correction is obtained by solving:

$$[H_{\rm KS} + \alpha P_{\rm v} - \varepsilon_v]\delta\varphi_v(r) = -P_{\rm c}\delta V_s(r)\varphi_v(r) = 0. \tag{3.73}$$

The expression for vectors $|\delta\Delta\varphi_v^\pm >$ in the second term of Eq.(3.70) needs some more effort, since it can be seen as the second-order variation of KS orbitals induced by applying consecutively to the ground state of KS system a static perturbing KS potential, δV_s, and a dynamic perturbation, $\Delta V_\alpha(iu,r)$. The derivation of these vectors needs, therefore, a second-order expansion in perturbation theory. However, in this work, we propose an alternative derivation that allows representing this term starting from the first-order variations of KS orbitals only.

Firstly, we consider the variation of KS system induced by applying the static perturbing potential, $\delta V_s(r)$. As mentioned above, the KS states will be perturbed so that the eigenstates are $\varphi_v(r) \to \varphi_v(r) + \delta\varphi_v(r)$ while the eigenvalues change as $\varepsilon_v \to \varepsilon_v + \delta\varepsilon_v$. By rewriting the linear equations of time-dependent DFT in Eqs.(3.45 and 3.46) with these new states while still keeping only the linear dependencies for

each perturbing potential, one can obtain the linear equations associated with (+) or (−) signs, respectively:

$$[H_{\rm KS} - (\varepsilon_v \pm iu)]|\delta\Delta\varphi_v^{\pm} > + [\delta V_s - \delta\varepsilon_v]|\Delta\varphi_v^{\pm} > + \Delta V_\alpha|\delta\varphi_v >= 0. \tag{3.74}$$

We then multiply by $< \Delta\varphi_v^{\mp}|$ the left-hand-side of Eq.(3.74), and sum over occupied states, which gives the formula,

$$\begin{aligned}\sum_v < \Delta\varphi_v^{\mp}|[H_{\rm KS} - (\varepsilon_v \pm iu)]|\delta\Delta\varphi_v^{\pm} > + \sum_v < \Delta\varphi_v^{\mp}|[\delta V_s - \delta\varepsilon_v]|\Delta\varphi_v^{\pm} > \\ + \sum_v < \Delta\varphi_v^{\mp}|\Delta V_\alpha|\delta\varphi_v > = 0.\end{aligned} \tag{3.75}$$

Finally taking the complex conjugate of Eqs.(3.45 and 3.46), multiplying by $|\delta\Delta\varphi_{kv}^{\mp} >$ the right-hand-side of the new expression, and summing over all the occupied states, we have:

$$\sum_v < \Delta\varphi_v^{\pm}|[H_{\rm KS} - (\varepsilon_v \mp iu)]|\delta\Delta\varphi_v^{\mp} > + \sum_v < \varphi_v|\Delta V_\alpha^*|\delta\Delta\varphi_v^{\mp} > = 0. \tag{3.76}$$

Combining the two results one obtains an expression linking terms containing $|\delta\Delta\varphi_v^{\mp} >$ to terms only containing first-order variation of the KS orbitals:

$$\sum_v < \varphi_v|[\Delta V_\alpha^*|\delta\Delta\varphi_v^{\mp} > = \sum_v < \Delta\varphi_v^{\pm}|[\delta V_s - \delta\varepsilon_v]|\Delta\varphi_v^{\mp} > + \sum_v < \Delta\varphi_v^{\pm}|\Delta V_\alpha|\delta\varphi_v >. \tag{3.77}$$

Inserting the relation of Eq.(3.72) into Eq.(3.77), and then rewriting Eq.(3.70), we get an expression for the variation of $\{a_\alpha\}$ as function of the first-order variation of KS orbitals:

$$\delta a_\alpha = \sum_{v,\sigma} < \delta\varphi_v|\Delta V_\alpha^*|\Delta\varphi_v^{\sigma} > + \sum_{v,\sigma} < \Delta\varphi_v^{-\sigma}|\delta V_s|\Delta\varphi_v^{\sigma} > - < \Delta\varphi_v^{-\sigma}|\Delta\varphi_v^{\sigma} >< \varphi_v|\delta V_s|\varphi_v >, \tag{3.78}$$

where, $\sigma = \pm$, $-\sigma = \mp$.

It is worth noting that in DFT, all the results must be invariant with respect to unitary transformations of the orbitals, which does not mix the manifold of occupied and unoccupied states. In Eq.(3.78), this invariance is not evident. It is, therefore, useful to recast Eq.(3.78) in a form which requires only the knowledge of the conduction-manifold projection of $\{\Delta\varphi_v^{\pm}\}$ and $\{\delta\varphi_v\}$, and is clearly invariant with respect to unitary transformations within the valence manifold, and which can straightforwardly and efficiently be implemented using non-degenerate first-order perturbation theory [18].

The transformation of Eq.(3.78) starts from the definition of the first order variations of the unperturbed KS states, $\{\Delta\varphi_v^{\pm}\}$ and $\{\delta\varphi_v\}$, separating the projections over the valence- and conduction-state manifolds:

$$\begin{aligned}|\delta\varphi_v > = P_{\rm c}|\delta\varphi_v > + P_{\rm v}|\delta\varphi_v >= \sum_{n\neq v}^{\infty} \frac{|\varphi_n >< \varphi_n|\delta V_s|\varphi_v >}{\varepsilon_v - \varepsilon_n} \\ |\Delta\varphi_v^{\pm} > = P_{\rm c}|\Delta\varphi_v^{\pm} > + P_{\rm v}|\Delta\varphi_v^{\pm} >= \sum_{n}^{\infty} \frac{|\varphi_n >< \varphi_n|\Delta V_\alpha|\varphi_v >}{(\varepsilon_v \pm iu) - \varepsilon_n}\end{aligned} \tag{3.79}$$

where, $P_{\rm v}$ and $P_{\rm c}$ are the projectors over valence and conduction manifolds, respectively. To simplify the formula, we employ hereafter the notations: $|\delta\widetilde{\varphi}_v>= P_{\rm c}|\delta\varphi_v>$ and $|\Delta\widetilde{\varphi}_v^{\pm}>= P_{\rm c}|\Delta\varphi_v^{\pm}>$, and then one can obtain:

$$\begin{aligned} |\delta\varphi_v>&= |\delta\widetilde{\varphi}_v> + \sum_{v'\neq v}^{occ} \frac{|\varphi_{v'}><\varphi_{v'}|\delta V_s|\varphi_v>}{\varepsilon_v-\varepsilon_{v'}} \\ |\Delta\varphi_v^{\pm}>&= |\Delta\widetilde{\varphi}_v^{\pm}> + \sum_{v'}^{occ} \frac{|\varphi_{v'}><\varphi_{v'}|\Delta V_\alpha|\varphi_v>}{(\varepsilon_v \pm iu)-\varepsilon_{v'}}. \end{aligned} \tag{3.80}$$

By means of a detailed manipulation that will be presented in Appendix B, we can recast result of Eq.(3.78) as:

$$\begin{aligned} \delta a_\alpha =& \sum_{v,\sigma}^{occ} <\Delta\widetilde{\varphi}_v^{-\sigma}|\delta V_s|\Delta\widetilde{\varphi}_v^{\sigma}> - \sum_{v,\sigma}^{occ} <\Delta\widetilde{\varphi}_v^{-\sigma}|\Delta\widetilde{\varphi}_v^{\sigma}><\varphi_v|\delta V_s|\varphi_v> \\ &+ \sum_{v,\sigma}^{occ} <\varphi_v|\delta V_s|(1-P_{\rm v})G(r,r',iu=0)|\Delta V_\alpha|\Delta\widetilde{\varphi}_v^{\sigma}> + c.c. \\ &- \sum_{v,v',\sigma}^{occ} <\varphi_v|\delta V_s|(1-P_{\rm v})G(r,r',iu=0)|\Delta\widetilde{\varphi}_{v'}^{\sigma}><\varphi_{v'}|\Delta V_\alpha|\varphi_v> + c.c. \end{aligned} \tag{3.81}$$

where, $\Delta\widetilde{\varphi}_v^{\pm}$ are first-order variation of the KS orbitals, φ_v, that are already projected on conduction states in the solution of Eqs.(3.47 and 3.48). $G(r,r',iu=0)$ denotes the static KS Green's function,

$$G(r,r',iu=0) = \sum_{n\neq v}^{\infty} \frac{\varphi_n(r')\varphi_n^*(r)}{\varepsilon_v-\varepsilon_n}. \tag{3.82}$$

Therefore, the right-hand-side of the last two terms in Eq.(3.81) can be combined and rewritten in a general formula,

$$|\widetilde{\varphi}_v^2>= (1-P_{\rm v})G(r,r',iu=0)|\Big[\sum_{\sigma}\Delta V_\alpha|\Delta\widetilde{\varphi}_v^{\sigma}> - \sum_{v'}^{occ}\Delta\widetilde{\varphi}_{v'}^{\sigma}><\varphi_{v'}|\Delta V_\alpha|\varphi_v>\Big]. \tag{3.83}$$

This expression allows to end up with the formula for the functional derivative of each eigenvalue:

$$\frac{\delta a_\alpha}{\delta V_s(r)} = \sum_{v}^{occ}\varphi_v^*(r)\widetilde{\varphi}_v^2(r) + cc... + \sum_{v,\sigma}^{occ}\Delta\widetilde{\varphi}_v^{-\sigma *}(r)\Delta\widetilde{\varphi}_v^{\sigma}(r) - \sum_{v',v,\sigma}^{occ} <\Delta\widetilde{\varphi}_v^{-\sigma}|\Delta\widetilde{\varphi}_{v'}^{\sigma}>\varphi_{v'}^*(r)\varphi_v(r) \tag{3.84}$$

To verify the expression in Eq.(3.84), we now consider a limit case where the dynamical response function, $\chi_0(r,r',iu)$, in Eq.(3.49) has the imaginary frequency, iu, of zero. The eigenpotentials, $\Delta V_\alpha(iu)$, is thus the static potentials. The calculation of $\delta a_\alpha(iu)/\delta V_s(r)$ at this limit is equivalent to determination of third order derivatives for the total energy with respect to the static perturbing KS potentials,

and this can be determined by using the 2n+1 theorem [18]. Detailed study for this problem was presented in work by Debernardi *et al.* [161]. One can find that the expression in Eq.(3.84) agrees to the formalism obtained by 2n+1 theorem without σ dependence. The agreement at this limit case shows the accuracy of our approach in computing functional derivative of a_α.

On the other hand, we also carried out another way to compute $\delta a_\alpha(iu)/\delta V_s(r)$ by using the numerical derivative calculations. In this approach, first we apply a sufficiently small perturbing potentials, $\pm\delta V_s$ at each point, r, in space of the unit cell. Then, the KS equations are recomputed with respect to these perturbations. a_α is perturbed and transforms to $a'_\alpha(\pm\delta V_s)$ with respect to $\pm\delta V_s$, respectively. The value of the numerical derivative of a_α at point r is given as:

$$\frac{\delta a_\alpha}{\delta V_s(r)} = \lim_{|\delta V_s|\to 0} \frac{a'_\alpha(+\delta V_s) - a'_\alpha(-\delta V_s)}{|2\delta V_s|}. \tag{3.85}$$

Yet, this approach is very computationally expensive, and it is used only to determine $\delta a_\alpha(iu)/\delta V_s(r)$ of some a_α for testing. The calculations verified the analysis expression in Eq.(3.84) compared to the numerical derivative results.

From the final expansion of $\frac{\delta a_\alpha}{\delta V_s(r)}$ in Eq.(3.84), one can see that the calculation only needs the first order variation of KS orbitals induced by the perturbing potential ΔV_α which are the solutions of the generalized eigenvalue problem, Eq.(3.31). It means that instead of calculating E_c^{RPA} and $\frac{\delta E_c^{\mathrm{RPA}}}{\delta V_s(r')}$ independently, an efficient algorithm allows to calculate them at the same time. At any given imaginary frequency iu, after obtaining converged eigenpotentials,$\{\Delta V_\alpha\}$, associated to the lowest-lying eigenvalues $\{a_\alpha\}$ in Eq.(3.31), we apply the time dependent DFPT procedure for these vector potentials to evaluate the first order variation of KS states, which are solutions of the linear equations in Eqs.(3.47 and 3.48).

The Gauss-Legendre algorithm is employed in order to transform the infinite integration with respect to iu to the summation over finite iu values. Overall, one can conclude that computational cost of the calculation for $\frac{\delta E_c^{\mathrm{RPA}}}{\delta V_s(r')}$ is equivalent to the one for E_c^{RPA}.

Another approach to obtain the RPA correlation potential has been discussed in the literature as the result of linearized Sham-Schlüter equations [150]. Detail of this calculation has been presented in works by U. von Barth *et al.* [151, 152, 153].

3.3.2 Optimized effective potential approach

In this section, we present the detailed derivation for the optimized effective potential (OEP) problem, so that the optimized effective potential $\mathrm{V_{OEP}}$, given in Eq.(3.55), can be obtained via a self-consistent field (scf) procedure. Let's start by considering the general KS equations for non-interacting systems,

$$\hat{H}_{\mathrm{KS}}\varphi_i(r) = \varepsilon_i\varphi_i(r) \tag{3.86}$$

where, KS Hamiltonian is $\hat{H}_{\mathrm{KS}} = \hat{T}_{\mathrm{KS}} + V_s$, and ε_i is the eigenvalue of each KS state. The accurate form of the effective local potential $V_s(r)$ will minimize the KS energy. In principle, the KS energy, E_{KS}, can be expressed as a function of $V_s(r)$ as:

$$E_{\mathrm{KS}} = T_{\mathrm{KS}}[n] + \int V_s(r)n(r)dr. \tag{3.87}$$

At the ground state of KS system, the gradient of this energy with respect to $n(r)$ is equal to zero,

$$\frac{\delta E_{\mathrm{KS}}}{\delta n(r)} = \frac{\delta T_{\mathrm{KS}}}{\delta n(r)} + V_s(r) = 0. \tag{3.88}$$

We can calculate the functional derivative of T_{KS} with respect to $V_s(r)$, using the chain rule, as:

$$\frac{\delta T_{\mathrm{KS}}}{\delta V_s(r)} = \frac{\delta T_{\mathrm{KS}}}{\delta n(r')}\frac{\delta n(r')}{\delta V_s(r)} = -V_s(r)\frac{\delta n(r')}{\delta V_s(r)}. \tag{3.89}$$

We now consider the total energy, E, of the interacting systems. According to KS approach, this energy consists of the energy's components:

$$E = T_{\mathrm{KS}}[n] + E_{\mathrm{ext}}[n] + E_{\mathrm{H}}[n] + E_{\mathrm{xc}}[\{\varphi_i\}], \tag{3.90}$$

where E_{xc} is expressed in the formalism of EXX/RPA-correlation energy, $E_{\mathrm{xc}}[\{\varphi_i\}] = E_{\mathrm{x}}^{\mathrm{EXX}} + E_{\mathrm{c}}^{\mathrm{RPA}}$, where $E_{\mathrm{x}}^{\mathrm{EXX}}$ and $E_{\mathrm{c}}^{\mathrm{RPA}}$ are given in Eq.(3.58) and Eq.(3.67), respectively.

We establish the gradient formula of E at the ground state as:

$$\begin{aligned}\frac{\delta E}{\delta V_s(r)} &= \frac{\delta T_{\mathrm{KS}}}{\delta V_s(r)} + \frac{\delta E_{\mathrm{ext}}}{\delta V_s(r)} + \frac{\delta E_{\mathrm{H}}}{\delta V_s(r)} + \frac{\delta E_{\mathrm{xc}}}{\delta V_s(r)} \\ &= \frac{\delta T_{\mathrm{KS}}}{\delta n(r')}\frac{\delta n_(r')}{\delta V_s(r)} + v_{\mathrm{ext}}\frac{\delta n_(r')}{\delta V_s(r)} + v_{\mathrm{H}}\frac{\delta n_(r')}{\delta V_s(r)} + \frac{\delta E_{\mathrm{xc}}}{\delta V_s(r)}.\end{aligned} \tag{3.91}$$

Since at the minimum $\frac{\delta E}{\delta V_s(r)} = 0$, we can write:

$$\frac{\delta T_{\mathrm{KS}}}{\delta n(r')}\frac{\delta n_(r')}{\delta V_s(r)} + v_{\mathrm{ext}}\frac{\delta n_(r')}{\delta V_s(r)} + v_{\mathrm{H}}\frac{\delta n_(r')}{\delta V_s(r)} + \frac{\delta E_{\mathrm{xc}}}{\delta V_s(r)} = 0. \tag{3.92}$$

Comparing Eqs.(3.89 and 3.92), one can obtain:

$$-V_s\frac{\delta n(r')}{\delta V_s(r)} + v_{\mathrm{ext}}\frac{\delta n_(r')}{\delta V_s(r)} + v_{\mathrm{H}}\frac{\delta n_(r')}{\delta V_s(r)} + \frac{\delta E_{\mathrm{xc}}}{\delta V_s(r)} = 0. \tag{3.93}$$

By using the definition of the KS density-density response function, $\chi_0(r',r) = \delta n(r')/\delta V_s(r)$, one can see that the OEP condition in Eq.(3.52) is equivalent to:

$$\chi_0(r,r')(v_{\rm H}(r') + v_{\rm ext}(r') - V_s(r')) + \frac{\delta E_{\rm xc}}{\delta V_s(r)} = 0. \tag{3.94}$$

This relation allows us to estimate the effective potential, $V_{\rm OEP}(r) = V_s(r)$, that yields a ground state density of the KS systems, and the minimum of the total energy within the EXX/RPA expressions for $E_{\rm xc}$:

$$V_s(r) = v_{\rm H}(r) + v_{\rm ext}(r) + \chi_0^{-1}(r,r')\frac{\delta E_{\rm xc}}{\delta V_s(r')}. \tag{3.95}$$

However, because $\chi_0(r,r')$, $v_{\rm H}(r)$, and $E_{\rm xc}$ are functional of density $n(r)$ and $\{\varphi_i\}$ that depend implicitly on $V_s(r)$, Eq.(3.95) is a non-linear equation. In principle, in order to obtain $V_s(r)$, a self-consistency field (scf) algorithm can be used to solve Eq.(3.95). This algorithm can be generalized through three steps: (i) starting from a trial effective potential $V_s(r)$, density and KS orbitals associated with this potential are obtained by solving the KS equations given in Eq.(3.86); (ii) $\chi_0(r,r')$, $v_{\rm H}(r)$, $E_{\rm xc}$, and $\delta E_{\rm xc}/\delta V_s(r)$ are estimated from the solutions in the first step; and (iii) using Eq.(3.94), the output potential, $V_s[out]$, is obtained. $V_s[out]$ will be used to construct the new input potential, $V_s[in]$, in the next scf cycle through the linear mixing method:

$$V_s^{(i+1)}[in] = V_s^{(i)}[in] + \alpha(V_s^{(i)}[out] - V_s^{(i)}[in]), \tag{3.96}$$

or

$$\begin{aligned} V_s^{(i+1)}[in] &= V_s^{(i)}[in] + \alpha\Big[v_{\rm H}(r) + v_{\rm ext}(r) + \chi_0^{-1}(r,r')\frac{\delta E_{\rm xc}}{\delta V_s(r')} - V_s^{(i)}[in]\Big] \\ &= V_s^{(i)}[in] + \alpha\Delta V, \end{aligned} \tag{3.97}$$

where i is index of the $i^{\rm th}$ scf cycle. To improve the efficiency of the scf procedure, we first discuss the mixing coefficient, α. When $V_s^{(i)}$ is not close to the optimized value, $E_{\rm KS}$ is not a quadratic function of the potential $V_s(r)$. In this case, even when exact value of ΔV is employed, a full step of $\alpha = 1$ may not decrease the total energy. This requires to optimize α at each scf cycle. In the literatures, line search method is a well known tool for this kind of problem [162]. Here, we generalize the steps of this method implemented in OEP procedure. On the multidimensional space of $E_{\rm KS}$ as a function of V_s, we first try a full step with $\alpha = 1$, then evaluate $E_{\rm KS}(\alpha = 1)$, and $\delta E/\delta V_s(r)$. If $E_{\rm KS}(\alpha = 1)$ does not decrease efficiently compared to $E_{\rm KS}(\alpha = 0)$, we try with a smaller value of α. Using $\delta E/\delta V_s(r)$ at three values of α allows to determine a cubic interpolation polynomial. The minimum of this cubic polynomial corresponds to the optimized value of α. The cubic polynomial model can be simplified to a quadratic one when $E_{\rm KS}$ is sufficiently close to its minimum values.

We now turn to discuss the efficient method used to estimate ΔV in Eq.(3.97). This update potential is defined as:

$$\Delta V = v_{\mathrm{H}}(r) + v_{\mathrm{ext}}(r) + \chi_0^{-1}(r,r')\frac{\delta E_{\mathrm{xc}}}{\delta V_s(r')} - V_s^{(i)}[in], \tag{3.98}$$

where $v_{\mathrm{H}}(r)$, $v_{\mathrm{ext}}(r)$ are the Hartree and the external potential, respectively. The expression of $\delta E_{\mathrm{xc}}/\delta V_s(r)$ has been established for EXX/RPA-correlation energy in previous section 3.3.1. The most difficult term is the estimation of $\chi_0^{-1}(r,r')$. Before presenting the algorithms used to treat $\chi_0^{-1}(r,r')$ in efficient ways, we discuss some available methods that, in principle, can be implemented for the OEP procedure. The first possible approach is based on traditional minimization methods such as steepest-descent, or conjugate gradient [162]. These methods directly use the information of the first-order derivative $\delta E/\delta V_s$ obtained at each scf cycle, given in Eq.(3.93). However, in practice, they are not commonly employed in OEP problem since their convergence is very slow if there is no efficient preconditioning. The second approach is based on determining an approximate Hessian matrix, $H(r,r') = \frac{\delta E^2}{\delta V_s(r)\delta V_s(r')}$. Efficient methods such as quasi-Newton or BFGS [162] based on the approximation of this matrix can speed up the optimization of the total energy in OEP problem. The implementations of this method are so-called direct-OEP [163], since $H(r,r')$ matrix allows to update directly the effective KS potential, ΔV_s, in each scf cycle:

$$H\Delta V_s = -\nabla E(V), \tag{3.99}$$

where $\nabla E(V)$ represents $\delta E/\delta V_s$. The optimization of the total energy using the direct-OEP has been developed recently for EXX-only problems by Yang and coworker [163, 164]. It has shown as a promising way for solving OEP problem. However, finding an accurate $H(r,r')$ matrix in KS problem is a difficult task since it requires to construct the infinite dimensional $H(r,r')$ matrix. This problem has been discussed in many works related to EXX-only implementations. It has been suggested that $H(r,r')$ matrix can be approximated by a finite dimensional one, and that this does not change much the final results [164, 165].

In the next two subsections, we will present the two different approaches studied in this thesis to estimate the local effective EXX/RPA potential:

$$\tilde{v}_{\mathrm{xc}}(r) = \int \chi_0^{-1}(r,r')\frac{\delta E_{\mathrm{xc}}}{\delta V_s(r')}dr', \tag{3.100}$$

of Eq.(3.98). The first approach, given in section 3.3.2.1, is based on the iterative method, while the second one, given in section 3.3.2.2, is the representation of $\tilde{v}_{\mathrm{xc}}$ by using an auxiliary potential basis sets. The estimation of $\tilde{v}_{\mathrm{xc}}$ using these approaches will be performed at each scf cycles.

3.3.2.1 Iterative Construction of EXX/RPA Effective Potential

The routine of the iterative OEP method reads from input a density vector in the real space, $n_{\mathrm{ref}}(r) = \delta E_{\mathrm{xc}}/\delta V_s(r)$. The output of the routine is the local potential,

$\tilde{v}_{\rm xc}(r)$. Lets start from the trial potential at the $0^{\rm th}$ step, $|v^{(0)}>$, the optimized potential at the $m^{\rm th}$ step, $|\bar{v}^{(m)}>$, is defined as the linear combination of the previous ones in the following form:

$$|\bar{v}^{(m)}>=|v^{(0)}>+\sum_{i=1}^{m}\alpha_i^{(m)}(|v^{(i)}>-|v^{(0)}>). \tag{3.101}$$

Applying the KS density-density response function, χ_0, to both sides of Eq.(3.101), one obtains:

$$\chi_0|\bar{v}^{(m)}>=\chi_0|v^{(0)}>+\sum_{i=1}^{m}\alpha_i^{(m)}(\chi_0|v^{(i)}>-\chi_0|v^{(0)}>). \tag{3.102}$$

According to the definition of χ_0, we obtain the first-order density variation induced by the potentials presented in Eq.(3.102) as:

$$|\bar{n}^{(m)}>=|n^{(0)}>+\sum_{i=1}^{m}\alpha_i^{(m)}(|n^{(i)}>-|n^{(0)}>). \tag{3.103}$$

In order to estimate whether the density induced by the optimized potential at the $m^{\rm th}$ step is close to the reference density $n_{\rm ref}(r)$ or not, we define residue vectors $|F^{(m)}>=|n_{\rm ref}>-|n^{(m)}>$. The Eq.(3.103), therefore, can be rewritten as:

$$(|n_{\rm ref}>-|\bar{n}^{(m)}>)=(|n_{\rm ref}>-|n^{(0)}>)+\sum_{i=1}^{m}\alpha_i^{(m)}[|n^{(i)}>-|n^{(0)}>], \tag{3.104}$$

giving the optimized residue vector at the m^{th} step:

$$|\bar{F}^{(m)}>=|F^{(0)}>+\sum_{i=1}^{m}\alpha_i^{(m)}[|F^{(0)}>-|F^{(i)}>]. \tag{3.105}$$

Minimizing the norm of the optimized residue vector at the $m^{\rm th}$ step, $|<\bar{F}^{(m)}|\bar{F}^{(m)}>|$, with respect to the coefficients $\alpha_i^{(m)}$, lead to the linear equation systems:

$$<F^{(i)}-F^{(0)}|F^{(0)}>=\sum_{j=1}^{m}\alpha_j^{(m)}<F^{(i)}-F^{(0)}|F^{(j)}-F^{(0)}>.\ \ i=1\ldots m \tag{3.106}$$

Solving these linear equations allows us to obtain the optimized coefficients $\alpha_i^{(m)}$. The optimized potential at the $m^{\rm th}$ step is constructed according to these coefficients, following Eq.(3.101). The optimized residue vector density at the $m^{\rm th}$ step is therefore recalculated as:

$$|\bar{F}^{(m)}>=|n_{\rm ref}>-\chi_0|\bar{v}^{(m)}>. \tag{3.107}$$

The potential at the $(m+1)^{\rm th}$ step can be updated by combining $|\bar{v}^{(m)}>$ and $|\bar{F}^{(m)}>$ through the relation:

$$|v^{(m+1)}>=|\bar{v}^{(m)}>+c|\Delta V>, \tag{3.108}$$

and the update density reads

$$|n^{(l+1)}>=\chi_0|v^{(l+1)}>. \tag{3.109}$$

Where c is a coefficient, and $\Delta V(r)=\int dr'\frac{\bar{F}^{(m)}(r')}{|r-r'|}$. Evaluation of $\Delta V(r)$ following this relation guarantees the correct behavior at infinity, $\lim_{r\to\infty}\tilde{v}_{\rm xc}\to 0$. The convergence of this iterative method is evaluated by defining a threshold for the norm of residual vector, $|<\bar{F}^{(m)}|\bar{F}^{(m)}>|\leq e_{\rm thr}$.

According to H-K theorem, at the ground state, the KS effective potential is uniquely defined. Therefore only an accurate evaluation for $\tilde{v}_{\rm xc}$ yields the minimum energy of systems. However, in practice, the iterative method is found to work well for EXX potential, while for RPA-correlation one, this method gives a strongly varying (unphysical) potential with respect to the number of iterative steps. Therefore, in order to find a more stable OEP procedure that can be applied for both EXX and RPA potential, we also consider the other approach that will be presented in the following.

3.3.2.2 Auxiliary basis set representation for EXX/RPA Effective Potential

The other approach for estimating $\tilde{v}_{\rm xc}(r)$ proposed by Görling and coworker has been shown as an efficient way to solve the OEP problem [166, 167, 168]. In this approach, $\tilde{v}_{\rm xc}(r)$ is represented through a linear combination of auxiliary potential basis sets [167]. In its first implementation to calculate a Si cluster, the basis set was chosen as the PW basis sets. However, the use of PW basis sets to represent $\tilde{v}_{\rm xc}(r)$ is problematic to periodic systems, since the cutoff energy of this basis set needs to be balanced with the cutoff energy of PW basis sets used to represent the KS wave functions, otherwise the resulting potential is very oscillatory (unphysical potential) [169]. In order to overcome this problem, Görling *et al.* have proposed to use a different basis sets such as Gaussian or Slater basis sets for representing $\tilde{v}_{\rm xc}(r)$ [168]. The use of Gaussian basis set has been applied to the case of EXX-only, where the local effective EXX potential is evaluated for different atoms, molecules and solid systems [170]. In this thesis, we will implement this approach to estimate the effective EXX/RPA potential, $\tilde{v}_{\rm xc}(r)$. However, instead of using the localized basis sets such as Gaussian or Slater basis sets, we will represent $\tilde{v}_{\rm xc}(r)$ through an auxiliary basis set, $\{f_\alpha(r)\}$, computed from the eigenpotentials of the finite response function matrix, $\chi_0(r,r')$.

Lets start by considering the general definition of $\tilde{v}_{\rm xc}(r)$ via the linear KS density-density response function:

$$\int dr'\chi_0(r,r')\tilde{v}_{\rm xc}(r')=\frac{\delta E_{\rm xc}}{\delta V_s(r)}=\delta n_{\rm xc}(r), \tag{3.110}$$

where $\delta n_{\rm xc}(r)$ is the functional derivative of EXX/RPA correlation energy with respect to KS perturbing potential, given in Eqs.(3.3.1.1 and 3.3.1.2), respectively.

We define the exchange-correlation charge density, $\bar{n}_{\rm xc}(r')$, as the charge distribution whose electrostatic potential is the exchange and correlation potential, $\tilde{v}_{\rm xc}$. According to the Poisson equation, we have a relation as:

$$\bar{n}_{\rm xc}(r) = -\frac{1}{4\pi}\nabla^2 \tilde{v}_{\rm xc}, \tag{3.111}$$

or

$$\tilde{v}_{\rm xc}(r) = \int dr' \frac{\bar{n}_{\rm xc}(r')}{|r-r'|}. \tag{3.112}$$

By substituting Eq.(3.112) in to Eq.(3.110):

$$\int dr' dr'' \frac{\chi_0(r,r')\bar{n}_{\rm xc}(r'')}{|r'-r''|} = \delta n_{\rm xc}(r). \tag{3.113}$$

In principle, $\bar{n}_{\rm xc}(r)$ can be expanded with respect to the auxiliary basis sets, $\{f_\alpha(r)\}$, as

$$\bar{n}_{\rm xc}(r) = \sum_{\alpha}^{\rm N_{aux}} c_\alpha f_\alpha(r), \tag{3.114}$$

where $\rm N_{aux}$ is the number of basis sets considered. Eq.(3.113), therefore, can be expanded with respect to the auxiliary basis sets. By multiplying both sides of Eq.(3.113) by $f_\alpha(r)$ and taking the integration over real space, one can obtain a matrix equation: $\mathbf{X}\ \mathbf{c} = \mathbf{t}$ for the vector $\mathbf{c}$ collecting the expansion coefficients of $\bar{n}_{\rm xc}(r)$. The elements $\chi_0^{\alpha\beta}$ of matrix $\mathbf{X}$ are given by:

$$\chi_0^{\alpha\beta} = \int dr_1 dr_2 dr_3 dr_4 \frac{f_\alpha(r_1)\chi_0(r_2,r_3)f_\beta(r_4)}{|r_1-r_2||r_3-r_4|}, \tag{3.115}$$

and the elements t_α of the vector t are given by:

$$t_\alpha = \int dr_1 dr_2 \frac{f_\alpha(r_1)\delta n_{\rm xc}(r_2)}{|r_1-r_2|}. \tag{3.116}$$

Solving this matrix equation, and obtaining the coefficients, $\{c_\alpha\}$, $\tilde{v}_{\rm xc}(r)$ is therefore defined as:

$$\tilde{v}_{\rm xc}(r) = \sum_{\alpha}^{\rm N_{aux}} c_\alpha \int dr' \frac{f_\alpha(r')}{|r-r'|}. \tag{3.117}$$

Because the exchange-correlation charge density is unique, the matrix equations has a unique solution for the set of $\{c_\alpha\}$ and $\tilde{v}_{\rm xc}$ potential will be defined uniquely.

To this end, we present an efficient way to construct the auxiliary basis set, $\{f_\alpha\}$, based on diagonalization of the finite χ_0 matrix. We consider the eigenvalue equation:

$$\chi_0|\omega_\alpha> = a_\alpha|\omega_\alpha> \tag{3.118}$$

where, $\{\omega_\alpha\}$ and $\{a_\alpha\}$ are eigenvectors and eigenvalues of χ_0, respectively. This equation is solved as for the generalized eigenvalue equation given in Eq.(3.21). Employing an iterative Davidson diagonalization, from a set of trial potential, one can obtain at convergence the solution for the basis sets: $\{f_\alpha\} = \{\omega_\alpha\}$.

3.4 Testing for the Implementation

In order to verify the implementation, in this sections we will carry out the calculations for Be atom and for simple molecules such as Be_2, H_2, H_2Be, and LiH. We will adopt the following notations:

(i) The total energy computed without correlation energy will be noted as:

$$E_{\rm tot}^{\rm EXX} = T_{\rm KS} + E_{\rm ext} + E_{\rm H} + E_{\rm x}^{\rm EXX}[\{\varphi_i\}], \tag{3.119}$$

where $T_{\rm KS}$ is the KS kinetic energy. $E_{\rm ext}$ and $E_{\rm H}$ are the external energy and Hartree energy, respectively. $E_{\rm x}^{\rm EXX}[\{\varphi_i\}]$ is the exchange energy (EXX) computed by HF exchange formalism, but using KS orbitals. In the HF scheme, $E_{\rm tot}^{\rm EXX}$ is the HF total energy, and this energy is labeled as $E_{\rm tot}^{\rm EXX}$@HF through this section.

(ii) The total energy computed with both EXX and RPA-correlation energy will be indicated as:

$$E_{\rm tot}^{\rm EXX/RPA} = T_{\rm KS} + E_{\rm ext} + E_{\rm H} + E_{\rm x}^{\rm EXX}[\{\varphi_i\}] + E_{\rm c}^{\rm RPA}[\{\varphi_i\}], \tag{3.120}$$

where $E_{\rm c}^{\rm RPA}[\{\varphi_i\}$ is RPA-correlation energy that is given in Eq.(3.67).

(iii) The binding energy of the molecules computed with both EXX and RPA-correlation energy will be indicated as:

$$E^{\rm b} = E_{\rm tot}^{\rm EXX/RPA}({\rm molecule}) - 2E_{\rm tot}^{\rm EXX/RPA}({\rm atom}). \tag{3.121}$$

Because $E_{\rm x}^{\rm EXX}[\{\varphi_i\}]$ and $E_{\rm c}^{\rm RPA}[\{\varphi_i\}]$ are post-KS orbitals, the energies can be evaluated by using KS orbitals computed by LDA, GGA, or PBE0,... functionals. A suffix is used to denote different types of the KS orbitals, for example $E_{\rm x}^{\rm EXX}$@LDA or $E_{\rm c}^{\rm RPA}$@LDA. Similarly, for the energies defined in Eq.(3.119), (3.120) and (3.121), they can be defined as $E_{\rm tot}^{\rm EXX}$@LDA, $E_{\rm tot}^{\rm EXX/RPA}$@LDA, and $E^{\rm b}$@LDA, respectively.

Furthermore, in this work we will employ two different scf procedures to minimize the total energy of KS systems. The first one optimizes the local effective KS potential with EXX-only OEP, named as XOEP. In this case, the total energy, that is named as $E_{\rm tot}^{\rm EXX}$@XOEP, will be minimized toward $E_{\rm tot}^{\rm EXX}$@HF. EXX and RPA-correlation energy computed with the density and KS orbitals optimized by the XOEP procedure are denoted as $E_{\rm x}^{\rm EXX}$@XOEP and $E_{\rm c}^{\rm RPA}$@XOEP, respectively. In addition, the energies defined in Eq.(3.120) and (3.121) are denoted as $E_{\rm tot}^{\rm EXX/RPA}$@XOEP and $E^{\rm b}$@XOEP, respectively. The second scf procedure optimizes the local effective KS potential with both EXX and RPA-correlation OEP, named simply as OEP. The energies computed with the KS orbitals and density optimized with OEP procedure are therefore denoted as $E_{\rm x}^{\rm EXX}$@OEP, $E_{\rm c}^{\rm RPA}$@OEP, $E_{\rm tot}^{\rm EXX}$@OEP, $E_{\rm tot}^{\rm EXX/RPA}$@OEP, and $E^{\rm b}$@OEP.

3.4.1 EXX/RPA applied for beryllium dimer

Among many examples of weakly bounded systems, Beryllium dimer, Be_2, has been known as the most difficult challenge for an accurate theoretical description of its

dissociation behaviors, although this simple molecule has only 4 electrons in the valence state. Experiments for Be_2 have shown that this molecule has a zero-bond order, its binding energy (BE) is exceptionally small ($\sim$ 0.1 eV), and the optimal bond length is of 2.45 Å [171]. In computational modeling, with the exception of Configuration Interaction (CI) method [172] that can yield the closest binding energy curve compared to experiment, see in Fig. 3.1, the other high accuracy approaches in quantum chemistry, such as second-order Møller-Plesset perturbation theory (MP2) [173] or coupled-cluster without triple excitations [173], are still poor in performing for this quantity. Quantum Monte Carlo (MC) methods such as variational Monte Carlo (VMC), and diffusion Monte Carlo (DMC) are also employed in the studies of Be_2. In general, the results computed by these approaches have good performance in calculating the dissociation curves compared to experiments, however, the value of the optimal bond length computed by DMC is slightly overestimated compared to the experimental value, ($\sim$ 5 %) [174], shown in Fig. 3.1.

The use of DFT to compute the ground state properties of Be_2 molecules has been known for many years [143]. The local or semi-local exchange correlation functional, such as LDA or GGA, has been applied to these calculations. The studies show that while these functionals can yield the equilibrium bond length of Be_2 in good agreement with experiment, the other quantities such as BE and the ground state vibrational frequency, ω_0, are seriously overestimated, i.e. BE is four times larger than experiment, and ω_0 is overestimated by ~ 100 cm^{-1}. EXX/RPA calculations for Be_2 done for the first time by X. Gonze *et al.* [143], improved the agreement of the equilibrium bond length, BE, and ω_0 with experiment [171].

Recently, Huy-Viet Nguyen *et al.* [14, 154, 16] have performed an extensive calculation for this molecule by using EXX/RPA, computed by methods similar to those presented in this thesis. Previous results have been verified by this approach. In particular, the authors discussed reason of the unphysical maximum problem present in the BE curve of Be_2 in EXX/RPA calculations [16]. This was suggested to originate from the lacking of a scf procedure for EXX/RPA.

In this work, we will apply the scf procedure proposed for EXX/RPA energy functional to study Be_2 dimer. The calculations will be performed at a different q-point, $q = (0, 0, 0)$, for E_c^{RPA} calculations compared to $q = (0, 0.5, 0)$ considered in the works by Huy-Viet Nguyen *et al.* [14, 154, 16]. The two implementations of OEP methods, introduced in section 3.3.2, will be checked for the case of single Be and Be_2. Finally, we will discuss the calculations of total energy of Be_2 as well as the role of scf in the calculations of BE curve of Be_2. In the following, the steps of testing for the convergence of E_c^{RPA} calculations with respect to input parameters will be present.

3.4.1.1 Testing for input parameters

The calculations of Beryllium in this thesis have been performed using a norm-conserving pseudopotential for descripting the interactions between Be nuclei and the valence electrons. This pseudopotential is similar to the one used in Ref. [143]

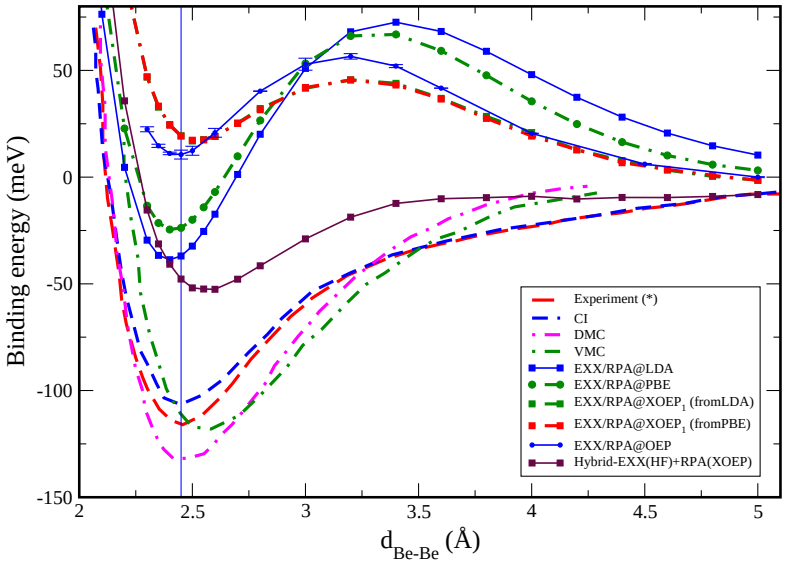

Figure 3.1: Dissociation energy curves of the Be dimer calculated using the EXX/RPA schemes with the different input KS wave functions: LDA (blue squares), GGA (green circles), and with KS orbital optimized by XOEP (red and green squares) and OEP (blue circles) procedures. In XOEP procedure, EXX potential is evaluated by using the iterative method, XOEP_1, which are started from LDA KS orbitals (green squares) or from PBE KS orbitals (red squares). A combination between $E_{\mathrm{tot}}^{\mathrm{EXX}}$@HF and $E_{\mathrm{c}}^{\mathrm{RPA}}$@XOEP is also presented (brown squares). The curve denoted experiment is obtained by fitting an Expanded Morse oscillator function to recent experimental data [171]. Theoretical results from QMC and CI methods are also shown for comparison. The green vertical line is according to the equilibrium bond length found in experiments, $d_{\mathrm{Be\text{-}Be}} = 2.45$ Å.

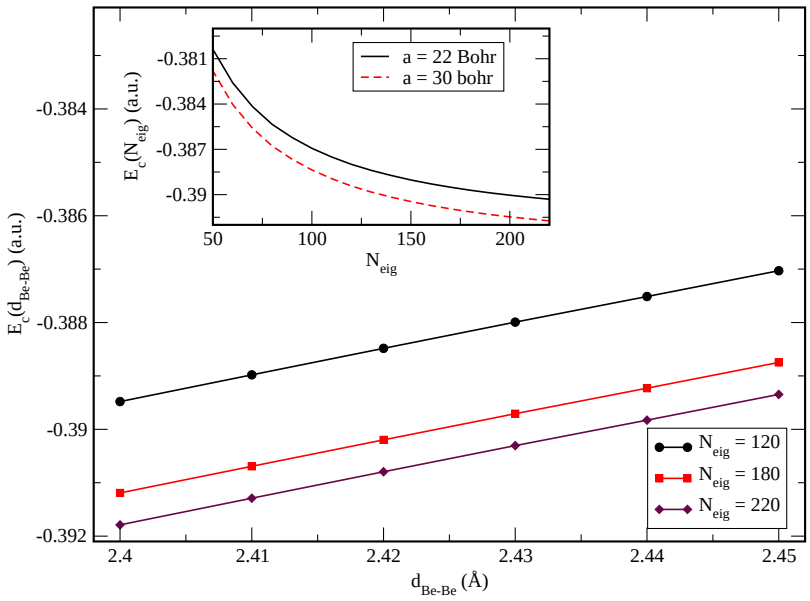

Figure 3.2: RPA correlation energies of Be_2 dimer at different Be-Be distances ($d_{\text{Be-Be}}$). The energies are computed at different number of eigenvalues N_{eig} with respect to Eq.(3.67): $N_{eig} = 120$ (black circles), $N_{eig} = 180$ (red squares), and $N_{eig} = 220$ (brown diamonds). Inset shows the convergence tendency of RPA correlation energies with respect to N_{eig}. The Be_2 molecule with $d_{\text{Be-Be}} = 2.45$ Å is placed in a simple cubic supercell with its size length of 22 Bohr (black solid line) and 30 Bohr (red dashed line).

and in previous works done by Huy-Viet Nguyen *et al.* [14, 16]. Be_2 is simulated as an isolated molecule by using the supercell technique. The E_x^{EXX} dependence on the supercell size (L), and kinetic cutoff energy (E_{cut}) have been studied in detail in previous works [14, 154]. Hence, we will now focus on testing the convergence of E_c^{RPA} computed at $q = (0;0;0)$ with respect to the following parameters: E_{cut}, L, and the number of eigenvalues, N_{eig}, employed in the evaluation of E_c^{RPA}, given in Eq.(3.67).

In order to estimate the initial guess of the input parameters, we carried out an extensive calculation at LDA level. The calculation was performed at a Be-Be distance, $d_{Be\text{-}Be}$, of 2.4 Å, close to the equilibrium bond length found in experiment[171]. Results have shown that a simple cubic supercell with $L > 22$ Bohr can converge BE of Be_2 molecule ≤ 0.05 mRy. Keeping $L = 22$ Bohr, E_{cut} is increased from 20 to 30 Ry, BE of the molecule varies of 0.05 mRy. These tests suggest the following input parameters for EXX/RPA calculations: $L = 22$ Bohr, and $E_{cut} = 25$ Ry. Similarly, we performed tests for E_c^{RPA} calculations. Firstly, the convergence of E_c^{RPA} with respect to E_{cut} is examined. We found that this energy converges very fast with respect to E_{cut}. It changes of < 0.05 mRy, when E_{cut} increases from 25 to 30 Ry. The next test is for E_c^{RPA} convergence with respect to N_{eig}. It shows that E_c^{RPA} changes of ~ 0.003 Ry when N_{eig} increases from 120 to 220. The convergence behavior of E_c^{RPA} is shown in the inset of Fig. 3.2. Because E_c^{RPA} calculation is performed many times with respect to the scf iteration, $N_{eig} = 120$ is chosen as the optimized parameter, and the absolute error for evaluating E_c^{RPA} is larger than 0.003 Ry. Nevertheless, when one considers the relative energy such as $\Delta E_c^{RPA} = E_c^{RPA}(Be_2) - 2E_c^{RPA}(Be)$, the relative error will be smaller than 0.003 Ry. Finally, the inset of Fig. 3.2 also shows the E_c^{RPA} dependence on the supercell size. When L changes from 22 to 30 Bohr, E_c^{RPA} is reduced by 0.0015 Ry, this value is smaller than the error with respect to N_{eig}.

3.4.1.2 OEP procedure within EXX/RPA applied on Be_2 dimer

Convergence of the two OEP approaches. We now turn to verify the implementations of the two OEP approaches proposed in section 3.3.2. It has been well known through several works for the exact exchange only OEP (XOEP) [17] that for systems with only two electrons, such as H_2 molecule or Be atom (considered in the case of using the pseudopotential method), XOEP can minimize E_{tot}^{EXX} toward E_{tot}^{EXX}@HF [175]. Therefore, here we will carry out the XOEP calculation for Be atom in order to verify the efficiency and accuracy of the OEP implementations. In addition, XOEP calculations for Be_2 dimer which has 4 valence electrons will be also discussed.

E_{tot}^{EXX} convergence with respect to the scf steps of Be atom is present in Fig. 3.3. The results show that EXX potential evaluated by the iterative scheme, labeled as OEP_1, can minimize E_{tot}^{EXX} better than OEP_2 that uses the auxiliary basis set to represent the potential. After 3 scf steps, OEP_1 yields energy differences between E_{tot}^{EXX} and E_{tot}^{EXX}@HF of ~ 0.01 meV. In contrast, this energy is higher (by ~ 0.5

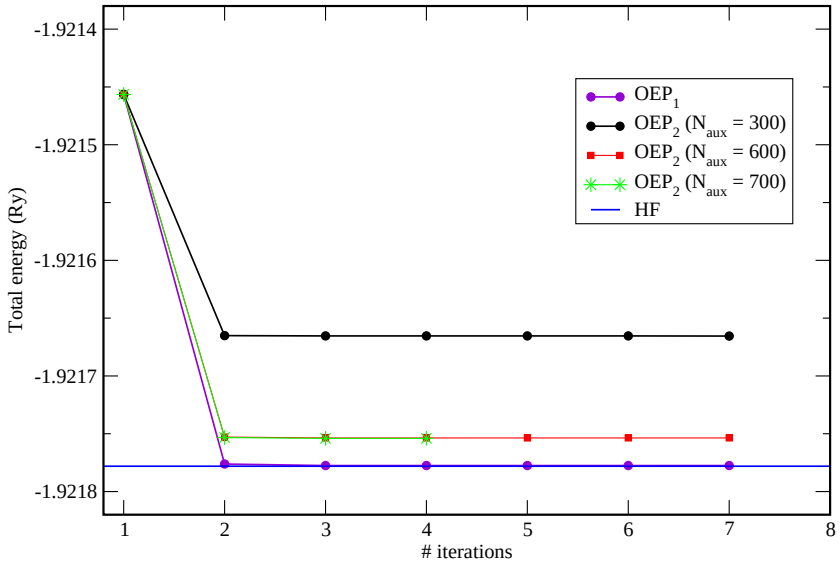

Figure 3.3: The minimization of $E_{\rm tot}^{\rm EXX}$ with respect to scf steps of single Be atoms. The estimation for EXX potential in XOEP procedure is carried out by two different approaches: (i) the EXX potential is represented by using the iterative method (violet circles), (ii) the EXX potential is represented by using the auxiliary basis set. In the second approach, the different number of auxiliary basis sets, $\rm N_{aux}$, are considered: $\rm N_{aux} = 300$ (black circle), $\rm N_{aux} = 600$ (red squares), and $\rm N_{aux} = 700$ (green stars). The minimum energies computed by the different approaches in XOEP procedure are compared to HF total energy, $E_{\rm tot}^{\rm EXX}$@HF.

meV) when $E_{\rm tot}^{\rm EXX}$ is minimized by $\rm OEP_2$, and $\rm N_{aux}$, the number of auxiliary basis sets, used to represent EXX potential is 600. It is also found that minimization of $E_{\rm tot}^{\rm EXX}$ by employing $\rm OEP_2$ strongly depends on $\rm N_{aux}$, for example, with $\rm N_{aux} = 300$, the minimum energy is higher than $E_{\rm tot}^{\rm EXX}$@HF by 2 meV, while increasing $\rm N_{aux}$ to 700 gives a similar energy to $\rm N_{aux} = 600$. Therefore, when $\rm OEP_2$ is used, checking the convergence of $E_{\rm tot}^{\rm EXX}$ with respect to $\rm N_{aux}$ is needed.

The optimization for EXX-potential in the case of $\rm Be_2$ dimer is also examined by using these OEP approaches, see Fig. 3.4(a). $E_{\rm tot}^{\rm EXX}$@XOEP for different bond lengths between the two Be atoms, $d_{\rm Be\text{-}Be}$, is compared to $E_{\rm tot}^{\rm EXX}$@LDA and $E_{\rm tot}^{\rm EXX}$@PBE that are evaluated at the first scf step, and to $E_{\rm tot}^{\rm EXX}$@HF. Here, to make comparison easy, we define a quantity, ΔE, that is computed as the difference between $E_{\rm tot}^{\rm EXX}$ and $E_{\rm tot}^{\rm EXX}$@HF. ΔE is computed for different cases of $E_{\rm tot}^{\rm EXX}$ and is presented in Fig. 3.4(b). We found that the convergence of XOEP depends on $d_{\rm Be\text{-}Be}$. At $d_{\rm Be\text{-}Be} > 4.0$ Å (~ 1.63 times larger than the equilibrium bond length of $\rm Be_2$) where the atoms in $\rm Be_2$ molecule are almost separate, $E_{\rm tot}^{\rm EXX}$@XOEP is minimized toward $E_{\rm tot}^{\rm EXX}$@HF ($\Delta E < 30$ meV). In contrast, at shorter distances ΔE increases significantly, and it has a maximum around $d_{\rm Be\text{-}Be} = 2.75$ Å. This finding means that for Be systems, XOEP works well with the independent Be atoms, while for $\rm Be_2$ dimer which has the 2s-valence electron wave functions of the two atoms overlap, XOEP can not completely minimize $E_{\rm tot}^{\rm EXX}$@XOEP toward $E_{\rm tot}^{\rm EXX}$@HF. Furthermore, we also present in the inset of Fig. 3.4(a) the convergence of $E_{\rm tot}^{\rm EXX}$@XOEP with respect to the scf steps, computed at $d_{\rm Be\text{-}Be} = 2.45$ Å. One can see that after 10 scf step $\rm OEP_1$ gives $E_{\rm tot}^{\rm EXX}$ lower than the energy obtained by $\rm OEP_2$ (~ 20 meV). The use of $\rm OEP_2$ with $\rm N_{aux} = 600$, on the other hand, is not enough for $\rm Be_2$ molecule, although, for the system of single Be atom, $\rm N_{aux} = 600$ can yield $E_{\rm tot}^{\rm EXX}$ equal to $E_{\rm tot}^{\rm EXX}$@HF.

OEP procedure applied for EXX/RPA. In Fig. 3.5, we present the total energy, $E_{\rm tot}^{\rm EXX/RPA}$, evaluated by EXX/RPA-correlation formalisms. The results demonstrate that $E_{\rm tot}^{\rm EXX/RPA}$@OEP is lower than $E_{\rm tot}^{\rm EXX/RPA}$@LDA and $E_{\rm tot}^{\rm EXX/RPA}$@GGA. This shows that the KS orbitals within LDA and GGA functionals are not yet optimized, and minimization of $E_{\rm tot}^{\rm EXX/RPA}$ in this case needs an scf procedure. Nevertheless, comparing the values between $E_{\rm tot}^{\rm EXX/RPA}$@OEP and $E_{\rm tot}^{\rm EXX/RPA}$@LDA(GGA), we found that the energy decrease using OEP method is different for the different $d_{\rm Be\text{-}Be}$, similar to the case of XOEP. At $d_{\rm Be\text{-}Be} = 5$ Å, $E_{\rm tot}^{\rm EXX/RPA}$ decreases of ~ 188.6 meV with respect to $E_{\rm tot}^{\rm EXX/RPA}$@LDA, while the decrease is of ~ 130.7 meV at $d_{\rm Be\text{-}Be} = 2.45$ Å. This difference will be shown later to be the reason why $\rm Be_2$ dimer results to be unbound when using the scf procedure. In addition, we also computed $E_{\rm tot}^{\rm EXX/RPA}$ for the XOEP case. $E_{\rm tot}^{\rm EXX/RPA}$@XOEP is found to be lower than $E_{\rm tot}^{\rm EXX/RPA}$@LDA(or GGA) at $d_{\rm Be\text{-}Be} > 2.8$ Å, but at shorter distances it is higher. This finding agrees with those shown in Fig. 3.4(b), where the at $d_{\rm Be\text{-}Be} < 2.8$ Å, XOEP approach gives a significant difference between $E_{\rm tot}^{\rm EXX}$ and $E_{\rm tot}^{\rm EXX}$@HF compared to the case at larger $d_{\rm Be\text{-}Be}$.

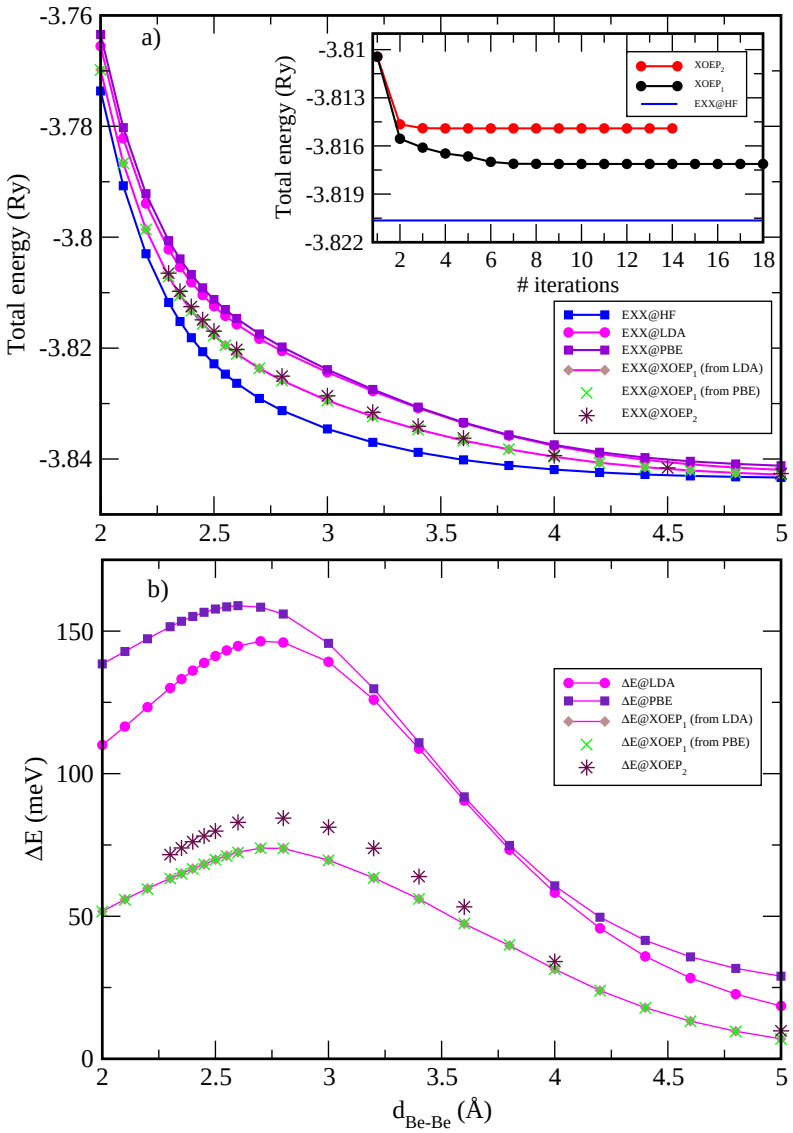

Figure 3.4: a) $E_{\rm tot}^{\rm EXX}$ of Be_2 molecule is computed at different Be-Be distances ($d_{\rm Be\text{-}Be}$). The energies are minimized by using the XOEP procedure. Two different OEP approaches to estimate EXX-only potential are employed. (i) The EXX potential is determined by using the iterative method, $\rm XOEP_1$. This scf procedure can start from LDA-KS orbitals (light brown diamonds) or from PBE KS orbitals (green crosses). (ii) The EXX-only potential is determined by using the auxiliary basis set representation, $\rm XOEP_2$, (brown stars). $E_{\rm tot}^{\rm EXX}$ energies are compared to those computed by using directly LDA and PBE KS orbitals, and to HF energies, $E_{\rm tot}^{\rm EXX}$@HF. In the inset, we present the convergence of $E_{\rm tot}^{\rm EXX}$ with respect to the scf steps, computed by using the two different OEP implementations at $d_{\rm Be\text{-}Be} = 2.45$ Å. b) We present $\Delta E = E_{\rm tot}^{\rm EXX} - E_{\rm tot}^{\rm EXX}$@HF at different $d_{\rm Be\text{-}Be}$.

Table 3.1: Binding energy, bond length, and vibrational frequency of Be_2 calculated in EXX/RPA schemes with different input KS-orbitals.

	LDA	GGA	XOEP	OEP	Exp.[171]
d_{eq}(Å)	2.40	2.42	2.52	2.44	2.45
E^{b}(meV)	-38.69	-24.55	+17.30	+10.09	-115.27
ω_e(cm^{-1})	305.2	293.7	215.0	241.0	275.8

From the total energy curve, we estimate the vibrational frequency, ω_e, and the equilibrium bond length of Be_2. The computed values by the scf procedure, presented in Table 3.1, show good agreement with experiment.

On the other hand, in order to estimate the convergence of OEP procedure, we computed the norm of the energy gradient $|\Delta n| = |\delta E/\delta V_s|$. The expression of $\delta E/\delta V_s$ is given in Eq.(3.91). Fig. 3.6(a) shows the relation between $E_{\rm tot}^{\rm EXX/RPA}$ and $|\Delta n|$ computed with respect to the scf steps. One can see that $|\Delta n|$ decreases significantly after the initial step, where $|\Delta n|$ is evaluated from LDA orbitals, while closer to the minimum the convergence becomes slower. After 4 scf steps, $E_{\rm tot}^{\rm EXX/RPA}$ is found to be linearly related to $|\Delta n|$. In particular, at $d_{\text{Be-Be}} > 4$ Å $E_{\rm tot}^{\rm EXX/RPA}$@OEP energies are almost converged, where the linear relation has zero slope. Comparing to the scf procedures using the density-mixing methods (such as Broyden [176] or Pulay mixing methods [177]) in solving KS equations, where $|\Delta n|$ can exponentially decrease with respect to the convergence of the total energy [177, 176], the convergence in OEP methods is found much slower.

Here, we propose a simple way to estimate how far $E_{\rm tot}^{\rm EXX/RPA}$@OEP is from the converged energy. In Fig. 3.6(a), at the linear regime, we extrapolate a linear relation between $E_{\rm tot}^{\rm EXX/RPA}$@OEP and $|\Delta n|$, $E = a|\Delta n|+b$. The lowest $E_{\rm tot}^{\rm EXX/RPA}$ is evaluated as the value of b, corresponding to $|\Delta n| = 0$. An example at $d_{\text{Be-Be}} = 2.45$ Å is shown in Fig. 3.6(b). According to this method, the error of the calculation of $E_{\rm tot}^{\rm EXX/RPA}$@OEP can be estimated as the difference between the energy obtained by the OEP approach and the lowest extrapolated value, and they are shown in Table 3.2 for different $d_{\text{Be-Be}}$. Here, we found that the absolute values of the errors are much smaller than $E_{\rm tot}^{\rm EXX/RPA}$, and its order is < 2 meV.

In Fig. 3.1, we show BE curves of Be_2 computed by the EXX/RPA schemes, and they are compared to those computed by high accuracy methods such as CI [172], DMC and VMD [174], and the one obtained by experiment [171]. We found that EXX/RPA@XOEP yields a higher value ($\sim$ 5%) for the equilibrium bond length of Be_2 molecule, this is similar to case of EXX/RPA@PBE0 [16]. In contrast, EXX/RPA@OEP gives the bond length in agreement with experiment, see Fig. 3.1. In addition, we found that with EXX/RPA@XOEP and EXX/RPA@OEP the height of the unphysical maximum at intermediate distance $d_{\text{Be-Be}}$ slightly decreases , compared to EXX/RPA@LDA or EXX/RPA@GGA. This shows a role of

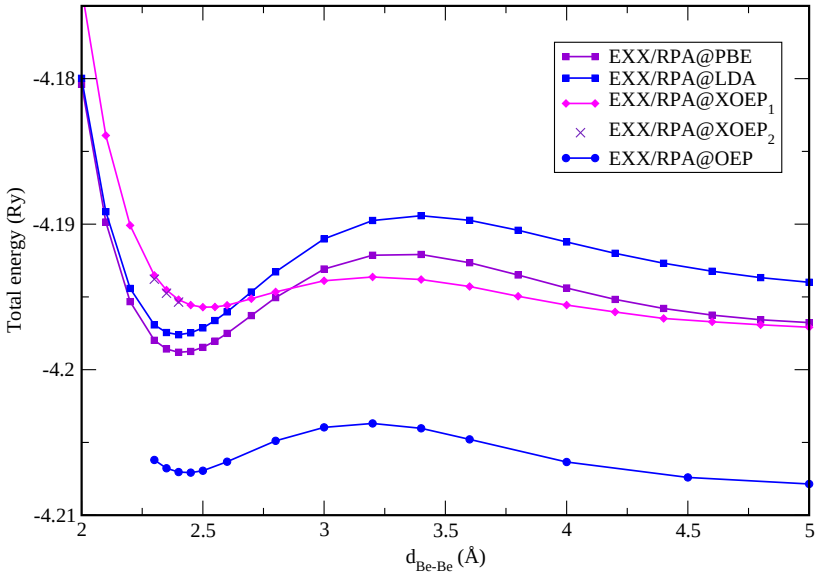

Figure 3.5: The total energy, $E_{\rm tot}^{\rm EXX/RPA}$, of Be_2 molecule is computed at different Be-Be distances ($d_{\rm Be\text{-}Be}$). The energy is minimized by using OEP method for both EXX and RPA-correlation potentials (blue circles), or by using XOEP method for EXX-only potential. The energies are compared to those computed from LDA (blue squares) and PBE (violet square) KS orbitals. In the XOEP procedure, $E_{\rm tot}^{\rm EXX/RPA}$ is computed by using two different implementations, such as $\rm XOEP_1$ (magenta diamonds) and $\rm XOEP_2$ (crosses), to determine EXX-only potential (see in text).

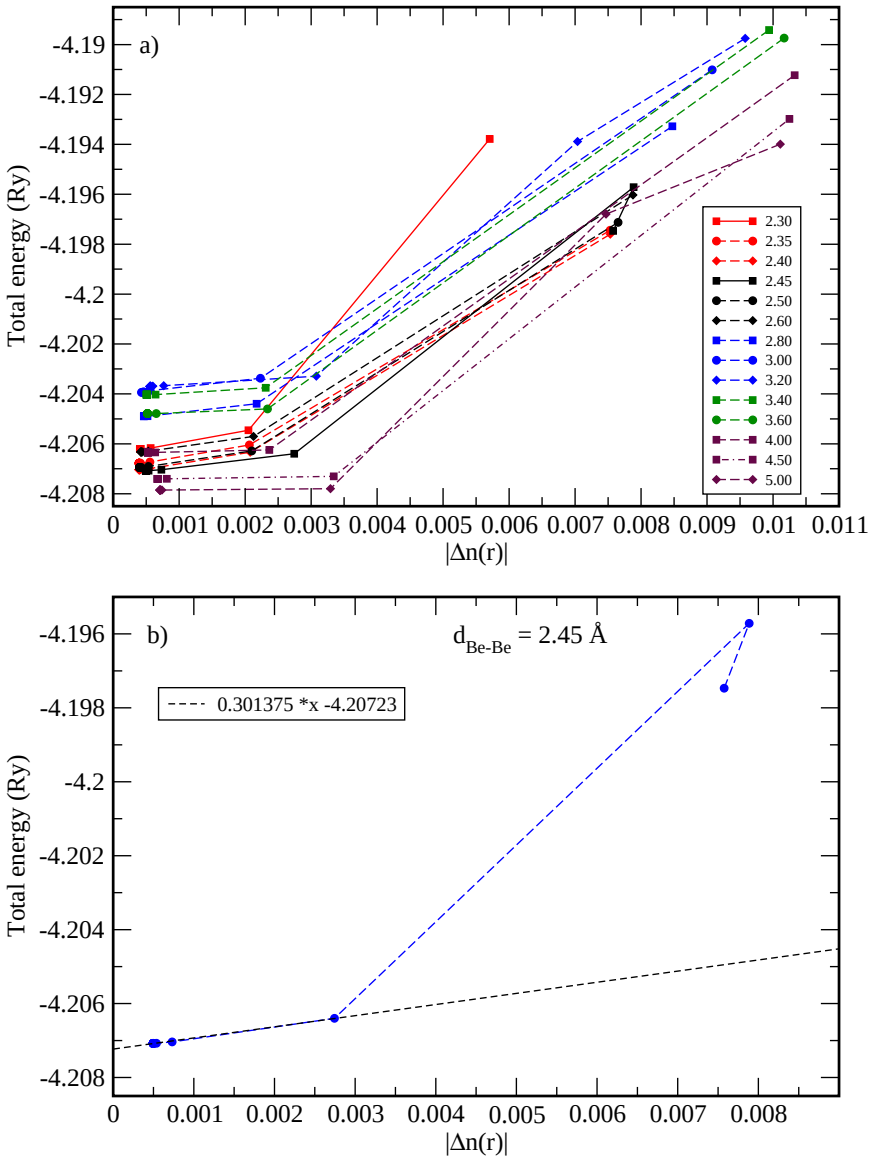

Figure 3.6: a) Relation between $E_{\rm tot}^{\rm EXX/RPA}$ and the norm of the energy gradient is computed at each scf step. This relation is evaluated at the different Be-Be distances ($d_{\text{Be-Be}}$). b) The linear relationship, $y = a|\Delta n| + b$, is extrapolated at $d_{\text{Be-Be}} = 2.45$ Å.

Table 3.2: The lowest energies ($\bar{E}$) of Be_2 dimer at the different Be-Be distances ($d_{\text{Be-Be}}$) are evaluated based on the linear relationship between $E_{\text{tot}}^{\text{EXX/RPA}}$@OEP and the norm of the energy gradient, $E = a|\Delta n| + b$, shown in Fig. 3.6(a). The errors of OEP procedure (ΔE) are estimated as: $\Delta E = E_{\text{tot}}^{\text{EXX/RPA}}\text{@OEP} - \bar{E}$.

$d_{\text{Be-Be}}$ Å	a	$\bar{E} = b$ (Ry)	$E_{\text{tot}}^{\text{EXX/RPA}}$@OEP (Ry)	ΔE (meV)
2.30	0.2142480	-4.2062900	-4.2062044	1.1646473
2.35	0.1507150	-4.2068300	-4.2067751	0.7469525
2.40	0.1057430	-4.2070800	-4.2070374	0.5796025
2.45	0.3013750	-4.2072300	-4.2070766	2.0871132
2.50	0.3899000	-4.2071000	-4.2069457	2.0993583
2.60	0.3658970	-4.2064800	-4.2063271	2.0803104
2.80	0.0135440	-4.2049000	-4.2048923	0.1047638
3.00	0.5363340	-4.2041700	-4.2039641	2.8014120
3.20	0.1615030	-4.2037900	-4.2036953	1.2884591
3.40	0.0922478	-4.2040800	-4.2040292	0.6911692
3.60	0.0046157	-4.2047900	-4.2047882	0.0244902
4.00	0.0003119	-4.2063500	-4.2063454	0.0625862
4.50	0.0398119	-4.2074300	-4.2074060	0.3265366
5.00	0.0211304	-4.2078700	-4.2078528	0.2340179

scf procedure in fixing the problem of EXX/RPA calculation, in agreement with the conclusions of Ref. [16]. However, the bump is still high compared to the correct behavior.

Another problem found in BE curve of EXX/RPA@XOEP and EXX/RPA@OEP is the positive value of BE of Be_2 molecule, corresponding to an unbound system. As discussed above, Fig. 3.4(b) shows that the difference between $E_{\text{tot}}^{\text{EXX}}$@XOEP and $E_{\text{tot}}^{\text{EXX}}$@HF is in the order of the difference between EXX/RPA@OEP and the experiment value (~ 100 meV at the maximum point). Therefore, this unexpected effect of scf can be understood as due to the incomplete convergence of OEP procedure in optimizing the EXX potentials rather than RPA-correlation potential. Here, to provide a strong evidence for this point, we consider the energy $E_{\text{tot}}^{\text{EXX/RPA}}$ which is computed as a combination between $E_{\text{tot}}^{\text{EXX}}$@HF energies and $E_{\text{c}}^{\text{RPA}}$@XOEP,

$$E_{\text{tot}}^{\text{EXX/RPA}}\text{@hybrid} = E_{\text{tot}}^{\text{EXX}}\text{@HF} + E_{\text{c}}^{\text{RPA}}\text{@XOEP}. \tag{3.122}$$

The BE curve (brown squares) computed by $E_{\text{tot}}^{\text{EXX/RPA}}$@hybrid is found not only to overcome the unphysical maximum but also to yield the closest BE with respect to experiment, see in Fig. 3.1

3.4.2 EXX/RPA applied for the other molecules

We now turn to discuss the results computed for covalent bond molecules, such as H_2, LiH, and H_2Be, by employing the EXX/RPA schemes. One of the interesting quantities considered for the H_2 and LiH molecules is the dissociation energy that is defined for H_2 as:

$$E_{\rm dis}(d_{\rm H\text{-}H}) = E_{\rm H_2}(d_{\rm H\text{-}H}) - E_{\rm H_2}(d_{\rm H\text{-}H} \to \infty), \tag{3.123}$$

and for HLi as:

$$E_{\rm dis}(d_{\rm H\text{-}Li}) = E_{\rm HLi}(d_{\rm H\text{-}Li}) - \big[\frac{1}{2}E_{\rm H_2}(d_{\rm H\text{-}H} \to \infty) + \frac{1}{2}E_{\rm Li_2}(d_{\rm Li\text{-}Li} \to \infty)\big], \tag{3.124}$$

where $E_{\rm H_2}(d_{\rm H\text{-}H})$ and $E_{\rm H_2}(d_{\rm H\text{-}H} \to \infty)$ are the total energy of H_2 molecule at finite and infinite distances between two atoms in molecule, respectively. Similarly, $E_{\rm HLi}(d_{\rm H\text{-}Li})$ and $E_{\rm Li_2}(d_{\rm Li\text{-}Li} \to \infty)$ are the total energy of HLi and Li_2 molecule at finite and infinite distances between two atoms in the molecules, respectively. For H_2Be molecule, we consider atomization energy, that is defined as:

$$E_{\rm ato}(d_{\rm Be\text{-}H}) = E_{\rm BeH_2}(d_{\rm Be\text{-}H}) - \big[E_{\rm H_2}(d_{\rm H\text{-}H} \to \infty) + \frac{1}{2}E_{\rm Be_2}(d_{\rm Be\text{-}Be} \to \infty)\big], \tag{3.125}$$

where $E_{\rm BeH_2}(d_{\rm Be\text{-}H})$ is the total energy of BeH_2 molecule a finite Be-H distance, while $E_{\rm Be_2}(d_{\rm Be\text{-}Be} \to \infty)$ is the total energy of Be_2 molecule at infinite distance between the two Be atoms.

The isolated molecules are simulated by using the supercell technique. For H_2 molecule, the calculations are set up with the cubic supercell of $L = 22$ Bohr size length. The kinetic cutoff energy is chosen as $E_{\rm cut} = 40$ Ry. This energy ensures to yield an error of $E_{\rm dis}(d_{\rm H\text{-}H} = 0.77$ Å$) < 0.01$ eV ($\sim 0.25\%$ value of BE found in experiment [178]) when $E_{\rm cut} > 40$ Ry, where $d_{\rm H\text{-}H} = 0.77$ Å is the equilibrium bond length of H_2 found in experiment [178]. The number of eigenvalues, $N_{\rm eig}$, used to evaluate RPA correlation energy is chosen as $N_{\rm eig} = 120$. This value gives a convergence for $E_{\rm c}^{\rm RPA}$ smaller than 0.001 eV. In Fig. 3.7, we present the total energy, $E_{\rm tot}^{\rm EXX/RPA}$ evaluated at the different bond lengths, $d_{\rm H\text{-}H}$, of H_2 molecule. This energy is computed from the different input KS orbitals within LDA or PBE exchange-correlation functional (first-shot). When we apply the scf procedure to optimize the EXX and RPA-correlation potentials, $E_{\rm tot}^{\rm EXX/RPA}$ is minimized with respect to the first-shot energy, see in the inset of Fig. 3.7 shown the total energy around the equilibrium bond length, $d_{\rm eq}$, of H_2 molecule. The values of $d_{\rm eq}$ are estimated with respect to the minimum point of the total energy curves, and they are presented in Table 3.3 for H_2, LiH, and H_2Be molecules. We found that for H_2 molecule the scf procedure does not change the value of $d_{\rm eq}$ compared to the value obtain in the first-shot curves, i.e. in both cases, $d_{\rm eq}$ give by $\sim 2.5\%$ overestimate with respect to experiment [178]. Similarly, the vibrational frequency, ω_e, which is evaluated by expressing the harmonic vibrational mode around $d_{\rm eq}$ [30], is found to be $\sim 5\%$ overestimated, compared to experiment [178]. In addition, comparing $E_{\rm dis}(d_{\rm eq})$,

presented in Table 3.3, computed by EXX/RPA schemes to those computed by HF or KS total energy with LDA or GGA exchange-correlation energy (they are not explicitly shown in Table 3.3, but can be estimated from the Fig. 3.7), one can see that HF and KS with the local and semi-local exchange-correlation functional give serious errors in describing the dissociation limit, i.e $E_{H_2}(d_{H\text{-}H} \to \infty)$ does not converge to the energy of two isolated H atoms. This problem is related to the use of unrestricted HF (or LDA) approximation where the electron on each isolated H atom is equally distributed on both spins so that self-interaction is not completely removed. In contrast, the total energy computed with RPA-correlation energy leads to a correct behavior, compared to calculation by high accuracy quantum chemistry method, i.e. by configuration interaction (CI) method [179].

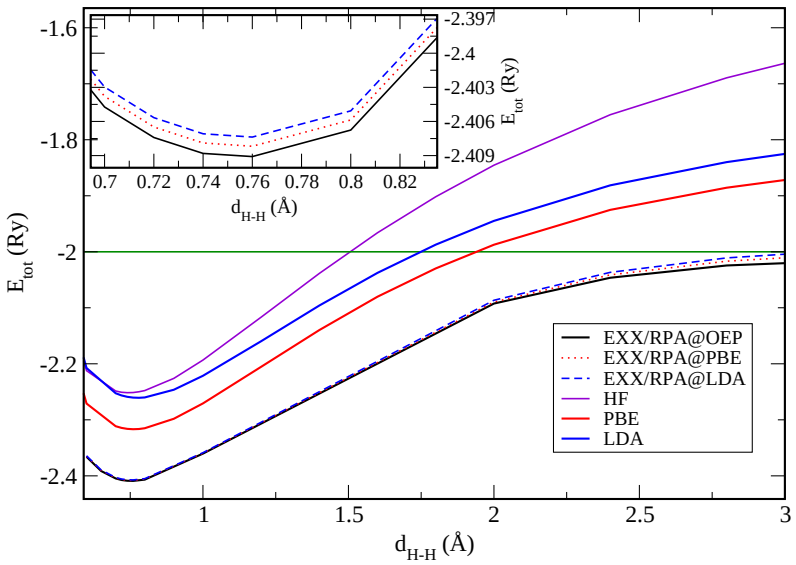

Figure 3.7: The total energy of H_2 molecule, $E_{tot}^{EXX/RPA}$, is computed at different H-H distances ($d_{H\text{-}H}$). The energy is evaluated with the input KS orbitals within LDA (blue dashed line) and PBE (red dotted line) exchange-correlation functionals, and it is also minimized by using the scf procedure (black line). These energies are compared to those computed from KS-LDA (blue line) and KS-PBE (red line), and HF (violet line). The inset shows $E_{tot}^{EXX/RPA}$ computed with $d_{H\text{-}H}$ around the equilibrium bond length.

For HLi and BeH_2 molecules, the computational sets up were checked similarly to H_2 molecule. We found that parameters as $L = 22$ Bohr, and $E_{cut} = 40$ Ry can give an error for E_{dis} of HLi and for atomization energy, E_{ato}, of H_2Be smaller than 0.01 eV. In the evaluation of E_c^{RPA}, N_{eig} in both molecules are chosen equal to 150.

This value allows to converge E_c^{RPA} to errors smaller than 0.05% with respect to energy found in the experiments [180].

In Fig. 3.8, the total energy curves of BeH_2 molecule are shown as function of Be-H distance. According to experimental measurement [181], BeH_2 molecule has been found to have a linear structure where three H-Be-H atoms are on a line and two H atoms bind to both sides of Be. Hence, in this work the Be-H bonds are stretched symmetrically with respect to Be atom. From the curves, the equilibrium bonds length of Be-H bonds are evaluated as 1.33, 1.30, and 1.33 Å for EXX/RPA@LDA, EXX/RPA@XOEP, and EXX/RPA@OEP, respectively. These values are in agreement with the experimental value, i.e. $d_{\mathrm{eq}} = 1.33$ Å. Comparing E_{ato} to the value computed by CI method [182], the EXX/RPA@OEP approach is found to yield an agreement with an error ~ 0.07 eV. Similarly, we also found an agreement in the symmetrical stretching ω_e between EXX/RPA schemes and CI calculations [182].

For the last example, the role of the scf procedure in minimizing the total energy of HLi molecule is studied in Fig 3.9. The results show that EXX/RPA@LDA and EXX/RPA@OEP schemes can give a good agreement for d_{eq}, E_{dis}, and ω_e compared to experiment [180], while the values obtained by EXX/RPA@XOEP are overestimated, see Table 3.3.

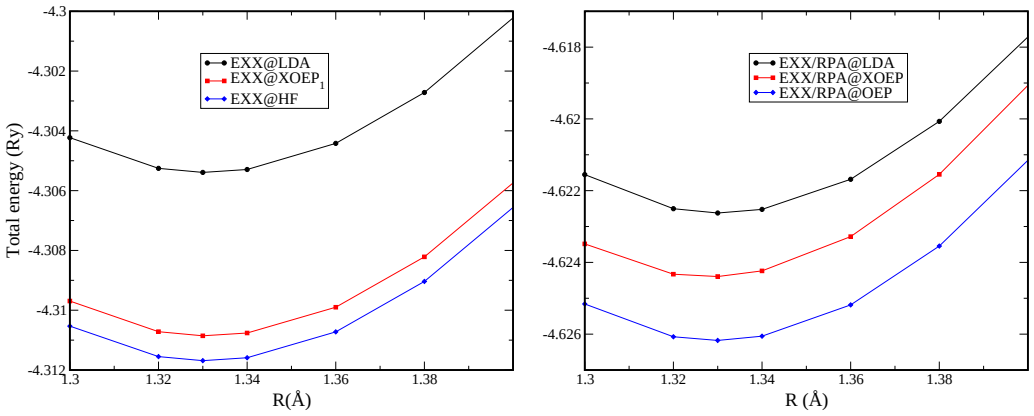

Figure 3.8: a) The total energy of H_2Be molecule without correlation energy, $E_{\mathrm{tot}}^{\mathrm{EXX}}$, is computed at different Be-H distances ($R = d_{\text{Be-H}}$). The energy is computed with the KS orbital within LDA exchange-correlation functional (black circles). The energy is minimized by using $XOEP_1$ method to estimate EXX-only potential (red squares). This energy is compared to HF energy (blue diamonds). b) The total energy of H_2Be molecule, $E_{\mathrm{tot}}^{\mathrm{EXX/RPA}}$, is computed at different Be-H distances ($d_{\text{Be-H}}$). The energy is computed with the KS orbital within LDA exchange-correlation functional (black circles). The energy is minimized by using $XOEP_1$ method to estimate EXX-only potential (red squares). The energy is minimized by using OEP method to estimate EXX and RPA-correlation potential (blue diamonds).

Table 3.3: Dissociation energy ($E_{\rm dis}$), atomization energy ($E_{\rm ato}$), the equilibrium bond length ($d_{\rm eq}$), and vibrational frequency (ω_e) of H_2, H_2Be, and HLi molecules calculated in EXX/RPA schemes with different input KS-orbitals.

		@LDA	@XOEP	@OEP	Exp.
H_2	$d_{\rm eq}$(Å)	0.755	-	0.755	0.771[178]
	$E_{\rm dis}$(eV)	-5.49	-	-5.28	-4.50[183]
	ω_e(cm^{-1})	4353.6	-	4351.3	4135.0[178]
H_2Be	$d_{\rm eq}$(Å)	1.320	1.335	1.310	1.33[181]
	$E_{\rm ato}$(eV)	-3.379	-3.84	-3.244	-3.17 [182]
	ω_e(cm^{-1})	2052.3	2005.0	2128.4	2083.0 [182]
HLi	$d_{\rm eq}$(Å)	1.615	1.620	1.615	1.595[180]
	$E_{\rm dis}$(eV)	-3.051	-3.250	-3.013	-2.5149[180]
	ω_e(cm^{-1})	1404.9	1443.1	1424.2	1405.8[180]

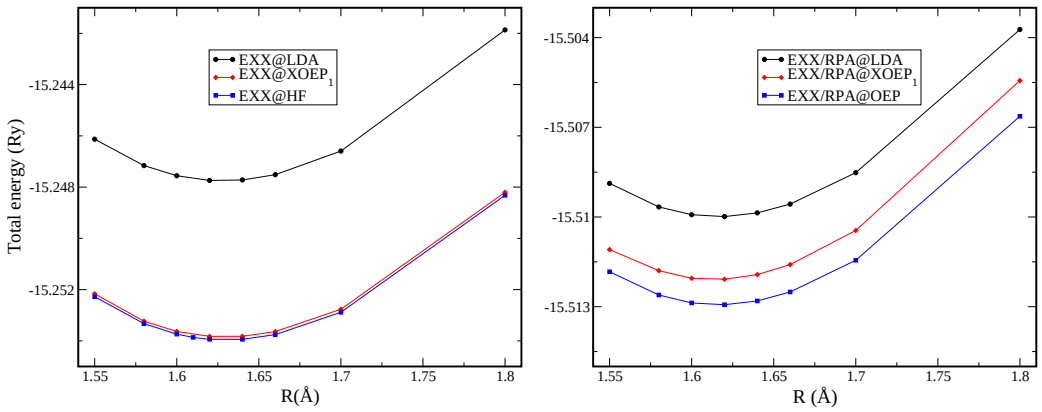

Figure 3.9: a) The total energy of HLi molecule without correlation energy, $E_{\rm tot}^{\rm EXX}$, is computed at different H-Li distances (R = $d_{\rm H\text{-}Li}$). The energy is computed with the KS orbital within LDA exchange-correlation functional (black circles). The energy is minimized by using $XOEP_1$ method to estimate EXX-only potential (red squares). This energy is compared to HF energy (blue diamonds). b) The total energy of HLi molecule, $E_{\rm tot}^{\rm EXX/RPA}$, is computed at different H-Li distances ($d_{\rm H\text{-}Li}$). The energy is computed with the KS orbital within LDA exchange-correlation functional (black circles). The energy is minimized by using $XOEP_1$ method to estimate EXX-only potential (red squares). The energy is minimized by using OEP method to estimate EXX and RPA-correlation potential (blue diamonds).

3.5 Conclusion

Through this chapter, we have proposed a new strategy for solving the self-consistent field (scf) KS equations in which the exchange and correlation energy are approximated as the Exact Exchange (EXX) and RPA-correlation functionals within the formally exact Adiabatic Connection Fluctuation-Dissipation (ACFD) formalism. The local effective EXX and RPA-correlation potentials yielding the minimum KS energy are determined by using the Optimized Effective Potential (OEP) approach. All development are based on the framework of the plane-wave basis set and pseudopotential methods. We have employed this implementation to study some simple examples such as the Be atom, and the H_2, Be_2, H_2Be, and HLi molecules.

In our approach, the calculation of the EXX and RPA-correlation potentials through the OEP method is performed by two main steps: (i) the determination of the functional derivative of the EXX and RPA-correlation energy with respect to the KS effective potential, and (ii) finding efficient approximations for the inverse KS density-density response function to compute the local effective potentials. The functional derivatives of the EXX and RPA-correlation energies are considered independently, and denoted as $\delta E_{\rm x}/\delta V_s(r)$ and $\delta E_{\rm c}/\delta V_s(r)$, respectively. The former is computed in the framework of an Exact Exchange-only OEP problem [17], combined with the very efficient Density Functional Perturbation Theory (DFPT) to compute directly the response density induced by the non-local EXX potential [18]. The calculation of $\delta E_{\rm c}/\delta V_s(r)$ is expressed through evaluating a small number of eigenvalues, $\{a_\alpha\}$, of RPA-dielectric function and its functional derivative with respect to KS potential, $\{\delta a_\alpha/\delta V_s(r)\}$. Where $\{a_\alpha\}$ as well as its eigenpotentials $\{\Delta V_\alpha\}$ are computed by employing an iterative diagonalization procedure. The density response from the trial perturbing potential is computed through the DFPT technique[18]. The analytic formula for $\{\delta a_\alpha/\delta V_s(r)\}$ is constructed in an expression that contains only terms of the ground state KS orbitals, and on their first-order correction induced by the perturbing potentials $\{\Delta V_\alpha\}$. This derivative formalism agrees with the 2n+1 theorem if ΔV_α is a static eigenpotential. In the second step, we constructed an efficient approximation for the inverted density-density response function, $\chi_0^{-1}(r,r')$, using two different approaches either the iterative methods or the auxiliary basis sets representation. The EXX/RPA-correlation potential is thus obtained as:

$$v_{\rm xc}(r) = \int \chi_0^{-1}(r,r')\Big[\frac{\delta E_{\rm x}}{\delta V_s(r')} + \frac{\delta E_{\rm c}}{\delta V_s(r')}\Big]dr', \tag{3.126}$$

which is optimized with respect to the scf steps.

All these procedures have been implemented in the Quantum ESPRESSO package [90] and have been tested for a few examples. We found that EXX and RPA-correlation potentials obtained by the OEP approaches can minimize the total energy of the systems, compared to the energy computed in the first scf step where the EXX and RPA-correlation energy are evaluated with the KS orbitals from LDA or GGA functionals. In particular, the efficiency and accuracy of the OEP approaches proposed in this thesis have been tested carefully for the problem of

EXX-only OEP (XOEP). In this case, the total energy, $E_{\rm tot}^{\rm EXX}$@XOEP, is computed without correlation term, and at the ground state it is compared to Hatree-Fock (HF) energy, $E_{\rm tot}^{\rm EXX}$@HF . We found that $E_{\rm tot}^{\rm EXX}$ is very close to HF energy, i.e. $\Delta E = \left[E_{\rm tot}^{\rm EXX}@{\rm XOEP} - E_{\rm tot}^{\rm EXX}@{\rm HF}\right] < 100$ meV, while for the system with only 2 electrons such as H_2 molecule, or Be atom (considered within a Pseudopotential method), $\Delta E \sim 0$, in agreement to the findings in Ref. [175].

For the Be_2 dimer, we found a significant improvement in estimating dissociation energy curve and vibrational frequency when using EXX/RPA-correlation energy calculations, without scf procedure, better than the standard DFT with a LDA or GGA exchange-correlation functional. Nevertheless, these calculations are found to strongly depend on the input KS orbitals. Employing an scf procedure, on the other hand, has been shown to overcome this problem. Moreover, the determination of quantities such as the equilibrium bond length ($d_{\rm eq}$), and vibrational frequency (ω_e) agrees with experiments, to an even better degree than those obtained by EXX/RPA without scf procedure. However, we found that the scf calculation of EXX/RPA-correlation energy yields unbound results in description binding energy curve of Be_2 dimer. This puzzle is found to be related to the EXX-potential optimization in OEP procedure that is different between Be isolated atom and Be_2 dimer.

For covalent bonded molecules such as H_2 molecule, we found that EXX/RPA calculations (with/without scf performance) can give an accurate behavior in the dissociation limit, while HF or KS with LDA (or GGA) functional gives a large error at large H-H bond distance. The calculations for $d_{\rm eq}$, ω_e, and dissociation energy (or atomization energy) for H_2, HLi and H_2Be molecules are also examined in this works. The results showed that EXX/RPA with OEP schemes can give the values of $d_{\rm eq}$ and ω_e in agreement with experiments and with results computed by high accuracy quantum methods.

Chapter 4

Summary and Outlook

In this thesis we have studied two different aspects of Density Functional Theory (DFT): (i) the application of DFT with the generalized gradient approximation (GGA) functional for exchange-correlation energy in modeling an heterogeneous catalysis problem, and (ii) the development of a new self-consistent field (scf) strategy to solve the Kohn-Sham (KS) equations that allows to improve the accuracy of DFT method with exact exchange (EXX) and RPA correlation energy functionals in the description of weak chemical interactions.

Ethylene epoxidation, one of the largest-scale catalytic processes in the chemical industry, were studied in Chapter 2 of this thesis. The formation of the desired product ethylene oxide (EO) in this reaction is promoted by a Ag-Cu alloy catalyst. In this study, the oxidation of ethylene is considered to occur on the Ag-Cu structures formed by thin copper-oxide layers on an Ag slab. These structures have been determined by theoretical and experimental works to be the favorable structures on the surfaces of Ag-Cu alloys in the high pressure and temperature conditions relevant to experiment. According to the calculations for reaction pathways, we found that the structures of Ag-Cu alloys are selective towards the formation of the EO final product, rather than the undesired product acetaldehyde (Ac) which is readily converted to carbon dioxide. The selectivity of Ag-Cu alloys is found to be higher than pure Ag, in agreement with experimental results. To do this, we carried out a study of the stability of the surface structures in thermodynamic equilibrium conditions (at $T = 600$ K and $p_{O_2} = 1$ atm), and we have shown that the higher selectivities relate to the formation of copper-oxide layers on the Ag slab. Moreover, our theoretical results show that the high selectivity of a copper-oxide layer is maintained even when the thickness of the oxide is increased to two layers. In particular, we have found that a very high selectivity could be obtained by structure containing 1.25 ML of Cu and 0.25 ML of sub-surface oxygen. Another important result is the finding of a selectivity indicator that allows to determine the selectivity of the pure metals and alloy catalysts even with the thin oxide structures in ethylene epoxidation reaction. In further works, this indicator could be applied to predict the selectivity of other Ag-based alloys such as Ag-Pd, Ag-Pt, etc. These alloys were found experimentally to be selective catalysts towards the formation of EO.

In spite of the great success of DFT when employing the well-known approximations such as LDA or GGA exchange-correlation functionals, the standard DFT approaches exhibit several serious shortcomings, and one of them is the poor or even wrong evaluation of long-range dispersion interactions (i.e., van der Waals interac-

tions). Calculations with the EXX/RPA-correlation energy within the adiabatic connection fluctuation-dissipation theorem (ACFDT) formalism have shown as a promising approach that can give the correct description not only of weak bonds but also of systems with covalent bonds. In Chapter 3, we developed the complete scf procedure that enables the optimization of KS systems whose total energy is computed with the EXX/RPA-correlation energy functionals. The implementation has been applied to the study of some simple molecules. In future work, EXX/RPA calculations could be applied to heterogeneous catalysis systems, where the role of van der Waals interactions is still largely unknown. Moreover, improvement of the accuracy of EXX/RPA calculations is also needed. According to ACFDT, one can go beyond the RPA formalism by taking into account higher-level approximations of the exchange-correlation kernel in the Dyson equation such as the time-dependent EXX kernel.

Appendix A

Computational details in studying Ethylene Epoxidation on Ag-Cu alloys

In this appendix, we present the details of the input parameters for the calculations based on Density Functional Theory (DFT), using the PWscf code integrated in the Quantum-ESPRESSO distribution [90], for studying ethylene epoxidation, presented in Chapter 2 of this thesis.

We employ the Generalized Gradient Approximation (GGA) of Perdew-Burke-Ernzerhof (PBE) [31] for the exchange and correlation functional. To describe the electron-ion interactions, ultrasolft pseudopotentials [25, 26], including scalar relativistic effects, is used. The Kohn-Sham wave functions are expanded in plane waves basis sets up to a kinetic energy cutoff of 30 Ry (300 Ry for the charge-density cutoff). This value is tested to give the adsoption energy for our test system converged within 8 meV. Brillouin-zone integrations have been performed with the special-point technique [184], smearing the Fermi surface through the Marzari-Vanderbilt cold-smearing technique [185], using a smearing parameter of 0.03 Ry (0.41 eV), this choice give adsorption energy of oxygen in our test system converged within 1 meV. The largest surface unit cell we considered is (4×4) on (111) surface, while most of the structures investigated have a (2×2) unit cell, see in Fig. A.1. The Brillouin-zone integrations are performed with a 6×6×1 Monkhort-Pack [184] grid for the (111) and (100) surfaces, and with a 6×4×1 grid for the (110) surface, while on the (111) with (4×4) unit cell, a 3×3×1 grid is used. The slabs are 5 layers thick (4 Ag layers and 1 layer for the Cu/O adsorbates) and the bottom 2 layers of the slab are kept fixed in their bulk positions. A 12 Å vacuum layer is used, which is found to be sufficient to ensure negligible coupling between periodic replicas of the slab.

For the calculation of the reaction pathways and the transition state along the minimum energy path (MEP), we adopt the climbing-image nudged-elastic band (CI-NEB) method [186]. Relaxation during NEB minimization is done for all atoms, except the bottom two layers that were kept fixed, until the forces are less than 0.02 eV/Å.

In practice, in order to reduce the computational cost in NEB calculations, the relaxation during NEB minimization is done with only 4 slabs (one bottom layer is removed), and also number of k-point is reduced from 6×6×1 to 4×4×1. When the CI-NEB run is converged, TS image is re-run with the full k-point grid and the full

number of atoms (5 slabs) by self-consistency field (SCF) only. The energy barrier is thus recalculated by taking the difference between the new energy of TS and the IS one that was done by Broyden-Fletcher-Goldfard-Shanno (BFGS) relaxation algorithms.

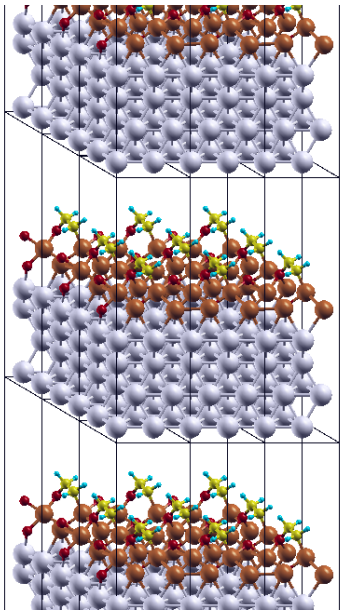

Figure A.1: Example of periodically repeated slab of OMC chemisorbed on CuO/Ag(111) surface, modeled with five layer slabs (4 Ag layers + 1CuO layer).

Appendix B

Derivation for functional derivative

In this appendix, we present how to recast the expression for the first-order variation of $\{a_\alpha\}$, the eigenvalue of generalized eigenvalue problem in Eq.(3.21), section 3.2.2. Let us start from the definition of the first order variation of KS states induced by a static perturbing potential δV, and a dynamic one, ΔV_α.

$$\begin{aligned}
|\delta\varphi_v> &= \sum_{m\neq v}^{\infty} \frac{|\varphi_{km}><\varphi_{km}|\delta V|\varphi_v>}{\varepsilon_v - \varepsilon_{km}} \\
|\Delta\varphi_v^+> &= \sum_{m}^{\infty} \frac{|\varphi_{km}><\varphi_{km}|\Delta V_\alpha|\varphi_v>}{(\varepsilon_v + iu) - \varepsilon_{km}} \\
|\Delta\varphi_v^-> &= \sum_{m}^{\infty} \frac{|\varphi_{km}><\varphi_{km}|\Delta V_\alpha|\varphi_v>}{(\varepsilon_v - iu) - \varepsilon_{km}}
\end{aligned} \tag{B.1}$$

where, the v index runs on the valence KS states, while m index runs over valence and conduction ones. These expressions can be separated in conduction- and valence-state manifolds contributions:

$$\begin{aligned}
|\delta\varphi_v> &= |\delta\widetilde{\varphi}_v> + \sum_{v'\neq v} \frac{|\varphi_{v'}><\varphi_{v'}|\delta V|\varphi_v>}{\varepsilon_v - \varepsilon_{v'}}, \\
|\Delta\varphi_v^+> &= |\Delta\widetilde{\varphi}_v^+> + \sum_{v'} \frac{|\varphi_{v'}><\varphi_{v'}|\Delta V_\alpha|\varphi_v>}{(\varepsilon_v + iu) - \varepsilon_{v'}}, \\
|\Delta\varphi_v^-> &= |\Delta\widetilde{\varphi}_v^-> + \sum_{v'} \frac{|\varphi_{v'}><\varphi_{v'}|\Delta V_\alpha|\varphi_v>}{(\varepsilon_v - iu) - \varepsilon_{v'}},
\end{aligned} \tag{B.2}$$

in which,

$$\begin{aligned}
|\delta\widetilde{\varphi}_v> &= P_c\delta\varphi_v = \sum_{c} \frac{|\varphi_{kc}><\varphi_{kc}|\delta V|\varphi_v>}{\varepsilon_v - \varepsilon_{kc}} \\
|\Delta\widetilde{\varphi}_v^+> &= P_c\Delta\varphi_v^+ = \sum_{c} \frac{|\varphi_{kc}><\varphi_{kc}|\Delta V|\varphi_v>}{(\varepsilon_v + iu) - \varepsilon_{kc}} \\
|\Delta\widetilde{\varphi}_v^-> &= P_c\Delta\varphi_v^- = \sum_{c} \frac{|\varphi_{kc}><\varphi_{kc}|\Delta V|\varphi_v>}{(\varepsilon_v - iu) - \varepsilon_{kc}}
\end{aligned} \tag{B.3}$$

where, c index runs on conduction states only.

The expression for the first-order variation of the eigenvalue $\{a_\alpha\}$ can be rewritten as:

$$\begin{aligned}\delta a_\alpha = \sum_v \big[&< \delta\varphi_v|\Delta V_\alpha^*|\Delta\varphi_v^+ > + < \delta\varphi_v|\Delta V_\alpha^*|\Delta\varphi_v^- > \\ &+ < \Delta\varphi_v^+|\Delta V_\alpha|\delta\varphi_v > + < \Delta\varphi_v^-|\Delta V_\alpha|\delta\varphi_v > \big] \\ + \sum_v \big[&< \Delta\varphi_v^+|\delta V|\Delta\varphi_v^- > - < \Delta\varphi_v^+|\Delta\varphi_v^- >< \varphi_v|\delta V|\varphi_v > \\ &+ < \Delta\varphi_v^-|\delta V|\Delta\varphi_v^+ > - < \Delta\varphi_v^-|\Delta\varphi_v^+ >< \varphi_v|\delta V|\varphi_v > \big].\end{aligned} \tag{B.4}$$

Substituting these definitions in Eq.(B.2) into the first term in the right-hand side of Eq.(B.4), one obtains a combination of four terms, which can denote by $P_\mathrm{c}P_\mathrm{c}$, $P_\mathrm{v}P_\mathrm{c}$, $P_\mathrm{c}P_\mathrm{v}$, and $P_\mathrm{v}P_\mathrm{v}$, depending on the pair of projectors appearing inside the matrix elements. The term:

$$\begin{aligned}\sum_v \big[&< \delta\varphi_v|\Delta V_\alpha^*|\Delta\varphi_v^+ > + < \delta\varphi_v|\Delta V_\alpha^*|\Delta\varphi_v^- > \\ &+ < \Delta\varphi_v^+|\Delta V_\alpha|\delta\varphi_v > + < \Delta\varphi_v^-|\Delta V_\alpha|\delta\varphi_v > \big]\end{aligned} \tag{B.5}$$

can therefore be decomposed in:

$P_\mathrm{c}P_\mathrm{c}$

$$= \sum_v < \delta\widetilde{\varphi}_v|\Delta V_\alpha^*|\Delta\widetilde{\varphi}_v^+ > + < \delta\widetilde{\varphi}_v|\Delta V_\alpha^*|\Delta\widetilde{\varphi}_v^- > + < \Delta\widetilde{\varphi}_v^+|\Delta V_\alpha|\delta\widetilde{\varphi}_v > + < \Delta\widetilde{\varphi}_v^-|\Delta V_\alpha|\delta\widetilde{\varphi}_v > \tag{B.6}$$

$P_\mathrm{v}P_\mathrm{c}$

$$= \sum_{v,v'\neq v} \frac{< \varphi_v|\delta V|\varphi_{v'} >}{\varepsilon_v - \varepsilon_{v'}} < \varphi_{v'}|\Delta V_\alpha^*|\Delta\widetilde{\varphi}_v^+ > + \sum_{v,v'\neq v} \frac{< \varphi_v|\delta V|\varphi_{v'} >}{\varepsilon_v - \varepsilon_{v'}} < \varphi_{v'}|\Delta V_\alpha^*|\Delta\widetilde{\varphi}_v^- > \tag{B.7}$$

$$+ \sum_{v,v'} \frac{< \varphi_v|\Delta V_\alpha^*|\varphi_{v'} >}{(\varepsilon_v - iu) - \varepsilon_{v'}} < \varphi_{v'}|\Delta V_\alpha|\delta\widetilde{\varphi}_v > + \sum_{v,v'} \frac{< \varphi_v|\Delta V_\alpha^*|\varphi_{v'} >}{(\varepsilon_v + iu) - \varepsilon_{v'}} < \varphi_{v'}|\Delta V_\alpha|\delta\widetilde{\varphi}_v > \tag{B.8}$$

$P_\mathrm{c}P_\mathrm{v}$

$$= \sum_{v,v'} < \delta\widetilde{\varphi}_v|\Delta V_\alpha^*|\varphi_{v'} > \frac{< \varphi_{v'}|\Delta V_\alpha|\varphi_v >}{(\varepsilon_v + iu) - \varepsilon_{v'}} + \sum_{v,v'} < \delta\widetilde{\varphi}_v|\Delta V_\alpha^*|\varphi_{v''} > \frac{< \varphi_{v''}|\Delta V_\alpha|\varphi_v >}{(\varepsilon_v - iu) - \varepsilon_{v''}} \tag{B.9}$$

$$+ \sum_{v,v'\neq v} < \Delta\widetilde{\varphi}_v^+|\Delta V_\alpha|\varphi_{v'} > \frac{< \varphi_{v'}|\delta V|\varphi_v >}{\varepsilon_v - \varepsilon_{v'}} + \sum_{v,v'\neq v} < \Delta\widetilde{\varphi}_v^-|\Delta V_\alpha|\varphi_{v'} > \frac{< \varphi_{v'}|\delta V|\varphi_v >}{\varepsilon_v - \varepsilon_{v'}} \tag{B.10}$$

$P_{\rm v}P_{\rm v}$

$$
\begin{aligned}
&= \sum_{v,v'\neq v,v''} \frac{<\varphi_v|\delta V|\varphi_{v'}>}{\varepsilon_v-\varepsilon_{v'}} <\varphi_{v'}|\Delta V_\alpha^*|\varphi_{v''}> \frac{<\varphi_{v''}|\Delta V_\alpha|\varphi_v>}{(\varepsilon_v+iu)-\varepsilon_{v''}} \\
&+ \sum_{v,v'\neq v,v''} \frac{<\varphi_v|\delta V|\varphi_{v'}>}{\varepsilon_v-\varepsilon_{v'}} <\varphi_{v'}|\Delta V_\alpha^*|\varphi_{v''}> \frac{<\varphi_{v''}|\Delta V_\alpha|\varphi_v>}{(\varepsilon_v-iu)-\varepsilon_{v''}} \\
&+ \sum_{v,v'\neq v,v''} \frac{<\varphi_v|\Delta V_\alpha^*|\varphi_{v''}>}{(\varepsilon_v-iu)-\varepsilon_{v''}} <\varphi_{v''}|\Delta V_\alpha|\varphi_{v'}> \frac{<\varphi_{v'}|\delta V|\varphi_v>}{\varepsilon_v-\varepsilon_{v'}} \\
&+ \sum_{v,v'\neq v,v''} \frac{<\varphi_v|\Delta V_\alpha^*|\varphi_{v''}>}{(\varepsilon_v+iu)-\varepsilon_{v''}} <\varphi_{v''}|\Delta V_\alpha|\varphi_{v'}> \frac{<\varphi_{v'}|\delta V|\varphi_v>}{\varepsilon_v-\varepsilon_{v'}}
\end{aligned}
\tag{B.11}
$$

Similarly, for the second term in the right-hand side of Eq.(B.4),

$$
\begin{aligned}
\sum_v \big[&<\Delta\varphi_v^+|\delta V|\Delta\varphi_v^-> - <\Delta\varphi_v^+|\Delta\varphi_v^-><\varphi_v|\delta V|\varphi_v> \\
&+ <\Delta\varphi_v^-|\delta V|\Delta\varphi_v^+> - <\Delta\varphi_v^-|\Delta\varphi_v^+><\varphi_v|\delta V|\varphi_v> \big].
\end{aligned}
\tag{B.12}
$$

We have:

$P_{\rm c}P_{\rm c}$

$$
\begin{aligned}
&= \sum_v <\Delta\widetilde{\varphi}_v^+|\delta V|\Delta\widetilde{\varphi}_v^-> - <\Delta\widetilde{\varphi}_v^+|\Delta\widetilde{\varphi}_v^-><\varphi_v|\delta V|\varphi_v> \\
&+ \sum_v <\Delta\widetilde{\varphi}_v^-|\delta V|\Delta\widetilde{\varphi}_v^+> - <\Delta\widetilde{\varphi}_v^-|\Delta\widetilde{\varphi}_v^+><\varphi_v|\delta V|\varphi_v>
\end{aligned}
\tag{B.13}
$$

$P_{\rm v}P_{\rm c}$

$$
= \sum_{v,v'} \frac{<\varphi_v|\Delta V_\alpha^*|\varphi_{v'}>}{(\varepsilon_v-iu)-\varepsilon_{v'}} <\varphi_{v'}|\delta V|\Delta\widetilde{\varphi}_v^-> + \sum_{v,v'} \frac{<\varphi_v|\Delta V_\alpha^*|\varphi_{v'}>}{(\varepsilon_v+iu)-\varepsilon_{v'}} <\varphi_{v''}|\delta V|\Delta\widetilde{\varphi}_v^+>
\tag{B.14}
$$

$P_{\rm c}P_{\rm v}$

$$
= \sum_{v,v'} <\Delta\widetilde{\varphi}_v^+|\delta V|\varphi_{v'}> \frac{<\varphi_{v'}|\Delta V_\alpha|\varphi_v>}{(\varepsilon_v-iu)-\varepsilon_{v'}} + \sum_{v,v'} <\Delta\widetilde{\varphi}_v^-|\delta V|\varphi_{v'}> \frac{<\varphi_{v'}|\Delta V_\alpha|\varphi_v>}{(\varepsilon_v+iu)-\varepsilon_{v'}}
\tag{B.15}
$$

$P_{\rm v}P_{\rm v}$

$$
\begin{aligned}
&= \sum_{v,v',v''} \frac{<\varphi_v|\Delta V_\alpha^*|\varphi_{v'}>}{(\varepsilon_v-iu)-\varepsilon_{v'}} <\varphi_{v'}|\delta V|\varphi_{v''}> \frac{<\varphi_{v''}|\Delta V_\alpha|\varphi_v>}{(\varepsilon_v-iu)-\varepsilon_{v''}} \\
&+ \sum_{v,v',v''} \frac{<\varphi_v|\Delta V_\alpha^*|\varphi_{v'}>}{(\varepsilon_v+iu)-\varepsilon_{v'}} <\varphi_{v'}|\delta V|\varphi_{v''}> \frac{<\varphi_{v''}|\Delta V_\alpha|\varphi_v>}{(\varepsilon_v+iu)-\varepsilon_{v''}}
\end{aligned}
\tag{B.16}
$$

$$
\begin{aligned}
&- \sum_{v,v'} \frac{<\varphi_v|\Delta V_\alpha^*|\varphi_{v'}><\varphi_{v'}|\Delta V_\alpha|\varphi_v>}{[(\varepsilon_v-iu)-\varepsilon_{v'}]^2} <\varphi_v|\delta V|\varphi_v> \\
&- \sum_{v,v'} \frac{<\varphi_v|\Delta V_\alpha^*|\varphi_{v'}><\varphi_{v'}|\Delta V_\alpha|\varphi_v>}{[(\varepsilon_v+iu)-\varepsilon_{v'}]^2} <\varphi_v|\delta V|\varphi_v>
\end{aligned}
\tag{B.17}
$$

Now, we can employ a few algebraic manipulations into each term of the above expansion. Grouping Eqs.(B.6 and B.13), we get:

$$\begin{aligned}
&\sum_{v} < \Delta\widetilde{\varphi}_{v}^{-}|\delta V|\Delta\widetilde{\varphi}_{v}^{+} > - \sum_{v} < \Delta\widetilde{\varphi}_{v}^{+}|\Delta\widetilde{\varphi}_{v}^{-} >< \varphi_{v}|\delta V|\varphi_{v} > \\
&+ \sum_{v} < \Delta\widetilde{\varphi}_{v}^{+}|\delta V|\Delta\widetilde{\varphi}_{v}^{-} > - \sum_{v} < \Delta\widetilde{\varphi}_{v}^{-}|\Delta\widetilde{\varphi}_{v}^{+} >< \varphi_{v}|\delta V|\varphi_{v} >
\end{aligned} \tag{B.18}$$

$$\begin{aligned}
&+ \sum_{v} < \delta\widetilde{\varphi}_{v}|\Delta V_{\alpha}^{*}|\Delta\widetilde{\varphi}_{v}^{+} > + < \delta\widetilde{\varphi}_{v}|\Delta V_{\alpha}^{*}|\Delta\widetilde{\varphi}_{v}^{-} > \\
&+ \sum_{v} < \Delta\widetilde{\varphi}_{v}^{+}|\Delta V_{\alpha}|\delta\widetilde{\varphi}_{v} > + < \Delta\widetilde{\varphi}_{v}^{-}|\Delta V_{\alpha}|\delta\widetilde{\varphi}_{v} >.
\end{aligned} \tag{B.19}$$

And grouping Eqs.(B.7 and B.10), we get:

$$\begin{aligned}
&+ \sum_{v,v' \neq v,c} \frac{< \varphi_{v}|\delta V|\varphi_{v'} >}{\varepsilon_{v} - \varepsilon_{v'}} < \varphi_{v'}|\Delta V_{\alpha}^{*}|\varphi_{c} > \frac{< \varphi_{c}|\Delta V_{\alpha}|\varphi_{v} >}{(\varepsilon_{v} + iu) - \varepsilon_{c}} \\
&+ \sum_{v,v' \neq v,c} \frac{< \varphi_{v}|\delta V|\varphi_{v'} >}{\varepsilon_{v} - \varepsilon_{v'}} < \varphi_{v'}|\Delta V_{\alpha}^{*}|\varphi_{c} > \frac{< \varphi_{c}|\Delta V_{\alpha}|\varphi_{v} >}{(\varepsilon_{v} - iu) - \varepsilon_{c}} \\
&+ \sum_{v,v' \neq v,c} \frac{< \varphi_{v}|\Delta V_{\alpha}^{*}|\varphi_{c} >}{(\varepsilon_{v} - iu) - \varepsilon_{c}} < \varphi_{c}|\Delta V_{\alpha}|\varphi_{v'} > \frac{< \varphi_{v'}|\delta V|\varphi_{v} >}{\varepsilon_{v} - \varepsilon_{v'}} \\
&+ \sum_{v,v' \neq v,c} \frac{< \varphi_{v}|\Delta V_{\alpha}^{*}|\varphi_{c} >}{(\varepsilon_{v} + iu) - \varepsilon_{c}} < \varphi_{c}|\Delta V_{\alpha}|\varphi_{v'} > \frac{< \varphi_{v'}|\delta V|\varphi_{v} >}{\varepsilon_{v} - \varepsilon_{v'}}
\end{aligned} \tag{B.20}$$

where, an expansion for $|\Delta\widetilde{\varphi}_{v}^{\pm} >$ projected over conduction state manifolds has been used.

Similarly, grouping Eqs.(B.9 and B.15), we get:

$$\begin{aligned}
&+ \sum_{v,v',c} \frac{< \varphi_{v}|\delta V|\varphi_{c} >}{\varepsilon_{v} - \varepsilon_{c}} < \varphi_{c}|\Delta V_{\alpha}^{*}|\varphi_{v'} > \frac{< \varphi_{v'}|\Delta V_{\alpha}|\varphi_{v} >}{(\varepsilon_{v} + iu) - \varepsilon_{v'}} \\
&+ \sum_{v,v',c} \frac{< \varphi_{v}|\delta V|\varphi_{c} >}{\varepsilon_{v} - \varepsilon_{c}} < \varphi_{c}|\Delta V_{\alpha}^{*}|\varphi_{v'} > \frac{< \varphi_{v'}|\Delta V_{\alpha}|\varphi_{v} >}{(\varepsilon_{v} - iu) - \varepsilon_{v'}} \\
&+ \sum_{v,v',c} \frac{< \varphi_{v}|\Delta V_{\alpha}^{*}|\varphi_{c} >}{(\varepsilon_{v} - iu) - \varepsilon_{c}} < \varphi_{c}|\delta V|\varphi_{v'} > \frac{< \varphi_{v'}|\Delta V_{\alpha}|\varphi_{v} >}{(\varepsilon_{v} - iu) - \varepsilon_{v'}} \\
&+ \sum_{v,v',c} \frac{< \varphi_{v}|\Delta V_{\alpha}^{*}|\varphi_{c} >}{(\varepsilon_{v} + iu) - \varepsilon_{c}} < \varphi_{c}|\delta V|\varphi_{v'} > \frac{< \varphi_{v'}|\Delta V_{\alpha}|\varphi_{v} >}{(\varepsilon_{v} + iu) - \varepsilon_{v'}},
\end{aligned} \tag{B.21}$$

and grouping Eqs.(B.8 and B.14), we get:

$$
\begin{aligned}
&+\sum_{v,v',c}\frac{<\varphi_v|\Delta V_\alpha^*|\varphi_{v'}>}{(\varepsilon_v-iu)-\varepsilon_{v'}}<\varphi_{v'}|\Delta V_\alpha|\varphi_c>\frac{<\varphi_c|\delta V|\varphi_v>}{\varepsilon_v-\varepsilon_c}\\
&+\sum_{v,v',c}\frac{<\varphi_v|\Delta V_\alpha^*|\varphi_{v'}>}{(\varepsilon_v+iu)-\varepsilon_{v'}}<\varphi_{v'}|\Delta V_\alpha|\varphi_c>\frac{<\varphi_c|\delta V|\varphi_v>}{\varepsilon_v-\varepsilon_c}\\
&+\sum_{v,v',c}\frac{<\varphi_v|\Delta V_\alpha^*|\varphi_{v'}>}{(\varepsilon_v-iu)-\varepsilon_{v'}}<\varphi_{v'}|\delta V|\varphi_c>\frac{<\varphi_c|\Delta V_\alpha|\varphi_v>}{(\varepsilon_v-iu)-\varepsilon_c}\\
&+\sum_{v,v',c}\frac{<\varphi_v|\Delta V_\alpha^*|\varphi_{v'}>}{(\varepsilon_v+iu)-\varepsilon_{v'}}<\varphi_{v'}|\delta V|\varphi_c>\frac{<\varphi_c|\Delta V_\alpha|\varphi_v>}{(\varepsilon_v+iu)-\varepsilon_c}
\end{aligned}
\tag{B.22}
$$

where, similarly, an expansion for $|\delta\widetilde{\varphi}_v>$ projected over conduction state manifolds has been used.

Part (B.20) is rewritten as:

$$
\begin{aligned}
&\sum_{v,v'\neq v,c}<\varphi_v|\delta V|\varphi_{v'}><\varphi_{v'}|\Delta V_\alpha^*|\varphi_c><\varphi_c|\Delta V_\alpha|\varphi_v>\\
&[\frac{1}{\varepsilon_v-\varepsilon_{v'}}(\frac{1}{(\varepsilon_v+iu)-\varepsilon_c}-\frac{1}{(\varepsilon_{v'}+iu)-\varepsilon_c})]+[\frac{1}{\varepsilon_v-\varepsilon_{v'}}(\frac{1}{(\varepsilon_v-iu)-\varepsilon_c}-\frac{1}{(\varepsilon_{v'}-iu)-\varepsilon_c})]\\
&=-\sum_{v,v'\neq v,c}\frac{<\varphi_v|\delta V|\varphi_{v'}><\varphi_{v'}|\Delta V_\alpha^*|\varphi_c><\varphi_c|\Delta V_\alpha|\varphi_v>}{[(\varepsilon_{v'}+iu)-\varepsilon_c][(\varepsilon_v+iu)-\varepsilon_c]}\\
&\quad-\sum_{v,v'\neq v,c}\frac{<\varphi_v|\delta V|\varphi_{v'}><\varphi_{v'}|\Delta V_\alpha^*|\varphi_c><\varphi_c|\Delta V_\alpha|\varphi_v>}{[(\varepsilon_{v'}-iu)-\varepsilon_c][(\varepsilon_v-iu)-\varepsilon_c]}\\
&=-\sum_{v,v'\neq v}<\Delta\widetilde{\varphi}_v^-|\Delta\widetilde{\varphi}_{v'}^+><\varphi_{v'}|\delta V|\varphi_v>-\sum_{v,v'\neq v}<\Delta\widetilde{\varphi}_v^+|\Delta\widetilde{\varphi}_{v'}^-><\varphi_{v'}|\delta V|\varphi_v>.
\end{aligned}
\tag{B.23}
$$

Part (B.21) is rewritten as:

$$
\begin{aligned}
&\sum_{v,v',c}<\varphi_v|\delta V|\varphi_c><\varphi_c|\Delta V_\alpha|\varphi_{v'}><\varphi_{v'}|\Delta V_\alpha^*|\varphi_v>\\
&[\frac{1}{\varepsilon_v-\varepsilon_c}(\frac{1}{(\varepsilon_v+iu)-\varepsilon_{v'}}+\frac{1}{(\varepsilon_v-iu)-\varepsilon_{v'}})\\
&+\frac{1}{(\varepsilon_{v'}+iu)-\varepsilon_c}\frac{1}{(\varepsilon_{v'}+iu)-\varepsilon_v}+\frac{1}{(\varepsilon_{v'}-iu)-\varepsilon_c}\frac{1}{(\varepsilon_{v'}-iu)-\varepsilon_v}]\\
&=-\sum_{v,v',c}\frac{<\varphi_v|\delta V|\varphi_c>}{\varepsilon_v-\varepsilon_c}\frac{<\varphi_c|\Delta V_\alpha|\varphi_{v'}>}{(\varepsilon_{v'}+iu)-\varepsilon_c}<\varphi_{v'}|\Delta V_\alpha|\varphi_v>\\
&\quad-\sum_{v,v',c}\frac{<\varphi_v|\delta V|\varphi_c>}{\varepsilon_v-\varepsilon_c}\frac{<\varphi_c|\Delta V_\alpha|\varphi_{v'}>}{(\varepsilon_{v'}-iu)-\varepsilon_c}<\varphi_{v'}|\Delta V_\alpha|\varphi_v>\\
&=-\sum_{v,v'}<\varphi_v|\delta V|(-P_c)G(\varepsilon_v,iu=0)|\Delta\widetilde{\varphi}_{v'}^+><\varphi_{v'}|\Delta V_\alpha|\varphi_v>\\
&\quad-\sum_{v,v'}<\varphi_v|\delta V|(-P_c)G(\varepsilon_v,iu=0)|\Delta\widetilde{\varphi}_{v'}^-><\varphi_{v'}|\Delta V_\alpha|\varphi_v>.
\end{aligned}
\tag{B.24}
$$

Part (B.22) is rewritten as:

$$
\begin{aligned}
&\sum_{v,v',c} < \varphi_c|\delta V|\varphi_v >< \varphi_v|\Delta V_\alpha|\varphi_{v'} >< \varphi_{v'}|\Delta V_\alpha^*|\varphi_c > \\
&[\frac{1}{\varepsilon_v - \varepsilon_c}(\frac{1}{(\varepsilon_v + iu) - \varepsilon_{v'}} + \frac{1}{(\varepsilon_v - iu) - \varepsilon_{v'}}) \\
&+ \frac{1}{(\varepsilon_{v'} + iu) - \varepsilon_c}\frac{1}{(\varepsilon_{v'} + iu) - \varepsilon_v} + \frac{1}{(\varepsilon_{v'} - iu) - \varepsilon_c}\frac{1}{(\varepsilon_{v'} - iu) - \varepsilon_v}] \\
=&-\sum_{v,v',c} \frac{< \varphi_c|\delta V|\varphi_v >}{\varepsilon_v - \varepsilon_c}\frac{< \varphi_c|\Delta V_\alpha|\varphi_{v'} >}{(\varepsilon_{v'} - iu) - \varepsilon_c} < \varphi_{v'}|\Delta V_\alpha|\varphi_v > \\
&-\sum_{v,v',c} \frac{< \varphi_c|\delta V|\varphi_v >}{\varepsilon_v - \varepsilon_c}\frac{< \varphi_c|\Delta V_\alpha|\varphi_{v'} >}{(\varepsilon_{v'} + iu) - \varepsilon_c} < \varphi_{v'}|\Delta V_\alpha|\varphi_v > \\
=&[-\sum_{v,v'} < \varphi_v|\delta V|(-P_c)G(\varepsilon_v, iu = 0)|\Delta\widetilde{\varphi}_{v'}^{+} >< \varphi_{v'}|\Delta V_\alpha^*|\varphi_v >]^* \\
&[-\sum_{v,v'} < \varphi_v|\delta V|(-P_c)G(\varepsilon_v, iu = 0)|\Delta\widetilde{\varphi}_{v'}^{-} >< \varphi_{v'}|\Delta V_\alpha^*|\varphi_v >]^*.
\end{aligned}
\tag{B.25}
$$

Part (B.16) can be spitted in two terms, depending on whether $v' = v$ or $v' \neq v$,

$$
\begin{aligned}
&\sum_{v,v'=v,v''} \frac{< \varphi_v|\Delta V_\alpha^*|\varphi_{v'} >}{(\varepsilon_v - iu) - \varepsilon_{v'}} < \varphi_{v'}|\delta V|\varphi_{v''} > \frac{< \varphi_{v''}|\Delta V_\alpha|\varphi_v >}{(\varepsilon_v - iu) - \varepsilon_{v''}} \\
&+ \sum_{v,v'=v,v''} \frac{< \varphi_v|\Delta V_\alpha^*|\varphi_{v'} >}{(\varepsilon_v + iu) - \varepsilon_{v'}} < \varphi_{v'}|\delta V|\varphi_{v''} > \frac{< \varphi_{v''}|\Delta V_\alpha|\varphi_v >}{(\varepsilon_v + iu) - \varepsilon_{v''}} \\
&+ \sum_{,v,v'\neq v,v''} \frac{< \varphi_v|\Delta V_\alpha^*|\varphi_{v'} >}{(\varepsilon_v - iu) - \varepsilon_{v'}} < \varphi_{v'}|\delta V|\varphi_{v''} > \frac{< \varphi_{v''}|\Delta V_\alpha|\varphi_v >}{(\varepsilon_v - iu) - \varepsilon_{v''}} \\
&+ \sum_{v,v'\neq v,v''} \frac{< \varphi_v|\Delta V_\alpha^*|\varphi_{v'} >}{(\varepsilon_v + iu) - \varepsilon_{v'}} < \varphi_{v'}|\delta V|\varphi_{v''} > \frac{< \varphi_{v''}|\Delta V_\alpha|\varphi_v >}{(\varepsilon_v + iu) - \varepsilon_{v''}}
\end{aligned}
\tag{B.26}
$$

where, the first two terms are rewritten as:

$$
\begin{aligned}
&\sum_{v,v'=v,v''} \frac{< \varphi_v|\Delta V_\alpha^*|\varphi_{v'} >}{(\varepsilon_v - iu) - \varepsilon_{v'}} < \varphi_{v'}|\delta V|\varphi_{v''} > \frac{< \varphi_{v''}|\Delta V_\alpha|\varphi_v >}{(\varepsilon_v - iu) - \varepsilon_{v''}} \\
&+ \sum_{v,v'=v,v''} \frac{< \varphi_v|\Delta V_\alpha^*|\varphi_{v'} >}{(\varepsilon_v + iu) - \varepsilon_{v'}} < \varphi_{v'}|\delta V|\varphi_{v''} > \frac{< \varphi_{v''}|\Delta V_\alpha|\varphi_v >}{(\varepsilon_v + iu) - \varepsilon_{v''}} \\
&= \sum_{v,v'=v,v''} < \varphi_v|\delta V|\varphi_v >< \varphi_v|\Delta V_\alpha^*|\varphi_{v''} >< \varphi_{v''}|\Delta V_\alpha|\varphi_v > \\
&[\frac{1}{[(\varepsilon_{v''} - iu) - \varepsilon_v]^2} + \frac{1}{[(\varepsilon_{v''} + iu) - \varepsilon_v]^2}].
\end{aligned}
\tag{B.27}
$$

Combining (B.27) with (B.17), we get

$$\begin{aligned}
&\sum_{v,v''} < \varphi_v|\delta V|\varphi_v >< \varphi_v|\Delta V_\alpha^*|\varphi_{v''} >< \varphi_{v''}|\Delta V_\alpha|\varphi_v > [\frac{1}{[(\varepsilon_{v''} - iu) - \varepsilon_v]^2} + \frac{1}{[(\varepsilon_{v''} + iu) - \varepsilon_v]^2}] \\
&-\sum_{v,v'} \frac{< \varphi_v|\Delta V_\alpha^*|\varphi_{v'} >< \varphi_{v'}|\Delta V_\alpha|\varphi_v >}{[(\varepsilon_v - iu) - \varepsilon_{v'}]^2} < \varphi_v|\delta V|\varphi_v > \\
&-\sum_{v,v'} \frac{< \varphi_v|\Delta V_\alpha^*|\varphi_{v'} >< \varphi_{v'}|\Delta V_\alpha|\varphi_v >}{[(\varepsilon_v - iu) - \varepsilon_{v'}]^2} < \varphi_v|\delta V|\varphi_v > = 0.
\end{aligned} \tag{B.28}$$

Combining the last two terms in (B.26) with (B.11), we get

$$\begin{aligned}
&\sum_{v,v' \neq v,v''} < \varphi_v|\delta V|\varphi_{v'} >< \varphi_{v'}|\Delta V_\alpha^*|\varphi_{v''} >< \varphi_{v''}|\Delta V_\alpha|\varphi_v > \\
&[\frac{1}{\varepsilon_v - \varepsilon_{v'}}(\frac{1}{(\varepsilon_v + iu) - \varepsilon_{v''}} + \frac{1}{(\varepsilon_v - iu) - \varepsilon_{v''}}) \\
&+ \frac{1}{\varepsilon_{v'} - \varepsilon_v}(\frac{1}{(\varepsilon_{v'} + iu) - \varepsilon_{v''}} + \frac{1}{(\varepsilon_{v'} - iu) - \varepsilon_{v''}}) \\
&+ \frac{1}{(\varepsilon_{v''} - iu) - \varepsilon_v}\frac{1}{(\varepsilon_{v''} - iu) - \varepsilon_{v'}} + \frac{1}{(\varepsilon_{v''} + iu) - \varepsilon_v}\frac{1}{(\varepsilon_{v''} + iu) - \varepsilon_{v'}}] = 0.
\end{aligned} \tag{B.29}$$

Overall, the results represented in the equations from (B.6) to (B.17) allow us to derive a final expansion for δa_α, which is written in form:

$$\begin{aligned}
&\delta a_\alpha = \\
&\sum_v < \Delta\widetilde{\varphi}_v^-|\delta V|\Delta\widetilde{\varphi}_v^+ > - \sum_{v,v'} < \Delta\widetilde{\varphi}_v^+|\Delta\widetilde{\varphi}_{v'}^- >< \varphi_{v'}|\delta V|\varphi_v > + cc \\
&+\sum_v < \varphi_v|\delta V|G(\varepsilon_v, iu = 0)(-P_c)|\Delta V_\alpha^*|\Delta\widetilde{\varphi}_v^- > + \sum_v \varphi_v|\delta V|G(\varepsilon_v, iu = 0)(-P_c)|\Delta V_\alpha^*|\Delta\widetilde{\varphi}_v^+ > + cc \\
&-\sum_{v,v'} < \varphi_v|\delta V|(-P_c)G(\varepsilon_v, iu = 0)|\Delta\widetilde{\varphi}_{v'}^+ >< \varphi_{v'}|\Delta V_\alpha^*|\varphi_v > + cc \\
&-\sum_{v,v'} < \varphi_v|\delta V|(-P_c)G(\varepsilon_v, iu = 0)|\Delta\widetilde{\varphi}_{v'}^- >< \varphi_{v'}|\Delta V_\alpha^*|\varphi_v > + cc.
\end{aligned} \tag{B.30}$$

Bibliography

[1] I. Chorkendorff and J. W. Niemantsverdriet. *Concepts of Modern Catalysis and Kinetics*. Wesley-VCH, Weinheim, 2003. (Cited on pages 1, 33 and 34.)

[2] J. P. Dever, K. F. George, W. C. Hoffman, and H. Soo. *Ethylene oxide, in: Kirk-Othmer Encyclopedia of Chemical Technology*. John Wiley and Sons, New York, 2001. (Cited on pages 1 and 18.)

[3] G. A. Somorjai. *Introduction to Surface Chemistry and Catalysis*. Wiley, New York, 1994. (Cited on pages 1, 33, 37 and 56.)

[4] G. Ertl. *Angew. Chem. Int. Ed.*, 47:3524, 2008. (Cited on page 1.)

[5] K. Reuter, C. Stampfl, and M. Scheffler. *Handbook of Materials Modeling, Part A Methods*. Springer, Berlin, Germany, 2005. (Cited on pages 2, 17, 28, 29 and 37.)

[6] K. Reuter. *Modeling Heterogeneous Catalytic Reactions: From the Molecular Process to the Technical System*. Wiley-VCH, Weinberg, 2009. (Cited on pages 2, 28, 29 and 30.)

[7] F. Tao and M. Salmeron. *Science*, 331:171, 2011. (Cited on page 2.)

[8] P. Hohenberg and W. Kohn. *Phys. Rev.*, 136:B846, 1964. (Cited on pages 2 and 7.)

[9] W. Kohn and L. J. Sham. *Phys. Rev. A*, 140:1133, 1965. (Cited on pages 2, 8 and 14.)

[10] J. K. Nørskov, T. Bligaard, J. Rossmeisl, and C. Christensen. *Nat. Chem.*, 1:37, 2009. (Cited on page 2.)

[11] J. F. Dobson and T. Gould. *J. Phys. Condens. Matter*, 24:073201, 2012. (Cited on pages 3, 16, 75, 76 and 77.)

[12] S. Grimme. *J. Comput. Chem.*, 25:1463, 2004. (Cited on pages 3 and 75.)

[13] D. C. Langreth and J.P. Perdew. *Sol. State. Comm.*, 17:1425, 1975. (Cited on pages 3, 76 and 79.)

[14] H-V. Nguyen and S. de Gironcoli. *Phys. Rev. B*, 79:205114, 2009. (Cited on pages 3, 76, 77, 101 and 104.)

[15] F. Furche. *J. Chem. Phys.*, 129:114105, 2008. (Cited on pages 3 and 77.)

[16] H-V. Nguyen and G. Galli. *J. Chem. Phys.*, 132:04419, 2010. (Cited on pages 3, 76, 77, 78, 101, 104, 108 and 111.)

[17] S. Kümmel and L. Kronik. *Rev. Mod. Phys.*, 80:3, 2008. (Cited on pages 3, 87, 104 and 116.)

[18] S. Baroni, S. de Gironcoli, A. Dacoso, and P. Giannozzi. *Rev. Mod. Phys.*, 70:515, 2001. (Cited on pages 3, 86, 89, 91, 93 and 116.)

[19] L. Schimka, J. Harl, A. Stroppa, A. Grüneis, M. Marsman, F. Mittendorfer, and G. Kresse. *Nat. Mater.*, 9:741, 2010. (Cited on pages 4, 16 and 76.)

[20] X. Ren, P. Rinke, and M. Scheffler. *Phys. Rev. Lett.*, 80:045402, 2009. (Cited on pages 4, 16 and 76.)

[21] M. Levy. *Pro. Natl. Acad. Sci.*, 76:6062, 1979. (Cited on page 7.)

[22] M. Levy. *Phys. Rev. A*, 1208:26, 1982. (Cited on page 7.)

[23] M. C. Payne, M. P. Teter, D. C. Allan, T. A. Arias, and J. D. Joannopoulos. *Rev. Mod. Phys.*, 64:1045, 1992. (Cited on page 12.)

[24] L. Kleinman and D. M. Bylander. *Phys. Rev. Lett.*, 48:1425, 1982. (Cited on page 13.)

[25] D. Vanderbilt. *Phys. Rev. B*, 41:7892, 1990. (Cited on pages 13 and 121.)

[26] The ultrasolft and norm-conserving pseudopotentials for atoms used in this Thesis such as Ag, Cu, O, C, H, Be, ... were taken from QUANTUM-ESPRESSO pseudopotential download page: http://www.quantum-espresso.org/pseudo.php (files: Ag.pbe-d-rrkjus.UPF, Cu.pbe-d-rrkjus.UPF,O.pbe-rrkjus.UPF, C.pbe-rrkjus.UPF, and H.pbe-rrkjus.UPF, ...). (Cited on pages 13 and 121.)

[27] J. P. Perdew, A. Ruzsinszky, J. Tao, V. N. Staroverov, G. E. Scuseria, and O. A. Vydrov. *J. Chem. Phys.*, 123:062201, 2005. (Cited on page 14.)

[28] O. Gunnarsson and B. I. Lundqvist. *Phys. Rev. B*, 13:4274, 1976. (Cited on pages 14 and 79.)

[29] J. P. Perdew and Y. Wang. *Phys. Rev. B*, 45:13244, 1992. (Cited on page 15.)

[30] R. M. Martin. *Electronic structure Basic Theory and Practical Methods*. Cambridge, New York, USA, 2004. (Cited on pages 15 and 112.)

[31] J. P. Perdew, K. Burke, and M. Ernzerhof. *Phys. Rev. Lett.*, 77:3865, 1996. (Cited on pages 15 and 121.)

[32] R. Miotto, G. P. Srivastava, and A. C. Ferraz. *Phys. Rev. B*, 59:3008, 1999. (Cited on page 15.)

[33] J. Tao, J. P. Perdew, A. Ruzsinszky, G. E. Scuseria, G. I. Csonka, and V. N. Staroverov. *Phil. Mag.*, 87:1071, 2007. (Cited on page 15.)

[34] S. H. Vosko, L. Wilk, and M. Nusair. *Can. J. Phys*, 58:1200, 1980. (Cited on page 15.)

[35] A. D. Becke. *Phys. Rev. A*, 38:3098, 1988. (Cited on page 15.)

[36] C. Lee, W. Yang, and R. G. Parr. *Phys. Rev. B*, 37:785, 1988. (Cited on page 15.)

[37] L. A. Curtiss, K. Raghavachari, P. C. Redfern, and J. A. Pople. *J. Chem. Phys.*, 106:1063, 1997. (Cited on page 15.)

[38] Y. Zhang, X. Xua, and W. A. Goddard. *Pro. Natl. Acad. Sci.*, 106:4963, 2009. (Cited on page 15.)

[39] M. Rohlfing and T. Bredow. *Phys. Rev. Lett.*, 101:266106, 2008. (Cited on pages 16 and 76.)

[40] J. Lacson. *Ethylene oxide, in Chemical Economics Handbook.* SRI International, Menlo Park, CA, 2003. (Cited on page 18.)

[41] J. G. Serafin, A. C. Liu, and S. R. Seyedmonir. *Mol. Catal. A: Chem.*, 131:157, 1998. (Cited on pages 18 and 56.)

[42] J. K. Nørskov, T. Bligaard, A. Logadottir, S. Bahn, L. B. Hansen, M. Bollinger, H. Bengaard, B. Hammer, Z. Sljivancanin, M. Mavrikakis, Y. Xu, S. Dahl, and C. J. H. Jacobsen. *J. Catal.*, 209:275, 2002. (Cited on pages 18, 26 and 52.)

[43] M. Mavrikakis, D. J. Doren, and M. A. Barteau. *J. Phys. Chem. B*, 102:394, 1998. (Cited on page 18.)

[44] R. A. van Stanten. *Handbook of Heterogeneous Catalysis*, volume 5. Wesley-VCH, Weinheim, 1997. (Cited on pages 18, 19, 21 and 33.)

[45] F. Ullman. *Encyclopedia of Industrial Chemistry.* VCH, Deerfield Beach, FL, USA, 5th edn. edition, 1985. (Cited on page 19.)

[46] S. Linic and M. A. Barteau. *J. Am. Chem. Soc.*, 124:310, 2002. (Cited on pages 19 and 20.)

[47] R. J. Madix. *Adv. Catal.*, 29:1, 1980. (Cited on page 19.)

[48] J. T. Roberts and R. J. Madix. *J. Am. Chem. Soc.*, 110:8540, 1988. (Cited on page 19.)

[49] X. Xu and C. M. Friend. *J. Am. Chem. Soc.*, 112:6779, 1991. (Cited on page 19.)

[50] N. W. Cant and W. K. Hall. *J. Catal.*, 52:81, 1978. (Cited on page 20.)

[51] S. Linic and M. A. Barteau. *Angew. Chem. Int. Ed.*, 43:2918, 2004. (Cited on page 20.)

[52] M. L. Bocquet, A. Michaelides, D. Loffreda, P. Sautet, A. Alavi, and D. A. King. *J. Am. Chem. Soc.*, 125:5620, 2003. (Cited on page 20.)

[53] A. Kokalj, P. Gava, S. de Gironcoli, and S. Baroni. *J. Catal.*, 254:304, 2008. (Cited on pages 20, 27, 38, 41, 51, 52, 53, 56, 64, 65, 66, 67, 72 and 73.)

[54] A. Kokalj, P. Gava, S. de Gironcoli, and S. Baroni. *J. Phys. Chem. C*, 112:1019–1027, 2008. (Cited on pages 20 and 42.)

[55] P. J. van den Hoek, E. J. Baerends, and R. A. van Santen. *J. Phys. Chem.*, 93:6469, 1989. (Cited on pages 21 and 56.)

[56] W. X. Li, C. Stampfl, and M. Scheffler. *Phys. Rev. B*, 67:045408, 2003. (Cited on pages 21, 30, 59, 68 and 69.)

[57] Y. Xu, J. Greeley, and M. Marvrikakis. *J. Am. Chem. Soc.*, 127:12823, 2005. (Cited on pages 21 and 56.)

[58] J. Greeley and M. Marvrikakis. *J. Phys. Chem. C*, 111:7992, 2007. (Cited on pages 21, 44, 46, 47, 63, 65 and 73.)

[59] S. Linic and M. A. Barteau. *J. Am. Chem. Soc.*, 126:8086, 2004. (Cited on page 21.)

[60] K. L. Yeung, A. Gavriilidis, A. Varma, and M. M. Bhasin. *J. Catal.*, 174:1, 1998. (Cited on page 21.)

[61] C. T. Campbell. *J. Catal.*, 99:28, 1986. (Cited on page 21.)

[62] C. T. Campbell and B. E. Koel. *J. Catal.*, 92:272, 1985. (Cited on page 21.)

[63] S. A. Tan, R. B. Grant, and R. M. Lambert. *J. Catal.*, 100:383, 1986. (Cited on page 21.)

[64] C. T. Campbell and M. T. Paffett. *Appl. Surf. Sci.*, 19:28, 1984. (Cited on page 21.)

[65] N. Toreis, X. E. Verykios, S. M. Khalid, G. Bunker, and Z. R. Korszun. *J. Catal.*, 109:143, 1988. (Cited on pages 21 and 22.)

[66] N. Toreis and X. E. Verykios. *J. Catal.*, 108:161, 1987. (Cited on page 21.)

[67] P. Mehrotra and X. E. Verykios. *J. Catal.*, 88:409, 1984. (Cited on page 21.)

[68] B. K. Bonin and X. E. Verykios. *J. Catal.*, 91:36, 1985. (Cited on page 21.)

[69] J. C. Dellamorte, J. Lauterbach, and M. A. Barteau. *Applied Catalysis A: General*, 391:281, 2011. (Cited on page 22.)

[70] J. C. Dellamorte, J. Lauterbach, and M. A. Barteau. *Ind. Eng. Chem. Res.*, 48:5943, 2009. (Cited on page 22.)

[71] A. B. Mhadeshwar and M. A. Barteau. *Mechanisms in Homogeneous and Heterogeneous Epoxidation Catalysis*. Elsevier, Amsterdam, 2008. (Cited on page 22.)

[72] S. Linic, J. Jankowiaka, and M. A. Barteau. *J. Catal.*, 224:489, 2004. (Cited on pages 22, 23, 24, 38, 48 and 72.)

[73] J. T. Jankowiak and M. A. Barteau. *J. Catal.*, 236:379, 2005. (Cited on page 22.)

[74] J. T. Jankowiak and M. A. Barteau. *J. Catal.*, 236:366, 2005. (Cited on pages 23, 45, 48 and 56.)

[75] M. L. Bocquet, P. Sautet, J. Cerda, C. I. Carlisle, M. J. Webb, and D. A. King. *J. Am. Chem. Soc.*, 125:3119, 2003. (Cited on pages 23, 41, 50 and 69.)

[76] J. C. Dellamorte, J. Lauterbach, and M. A. Barteau. *Ind. Eng. Chem. Res.*, 48:5943, 2009. (Cited on pages 23 and 24.)

[77] S. Piccinin, S. Zafeiratos, C. Stampfl, T. W. Hansen, M. Havecker, D. Teschner, V. I. Bukhtiyarov, F. Girgsdies, A. Knop-Gericke, R. Schlöegl, and M. Scheffler. *Phys. Rev. Lett.*, 104:035503, 2010. (Cited on pages 23, 25, 26, 38, 45, 59 and 72.)

[78] S. Piccinin, C. Stampfl, and M. Scheffler. *Surf. Sci.*, 603:1467, 2009. (Cited on pages 26, 38, 42, 46, 59, 69 and 72.)

[79] S. Piccinin, C. Stampfl, and M. Scheffler. *Phys. Rev. B*, 77:075426, 2008. (Cited on pages 26, 30, 38, 42, 46, 59, 69 and 72.)

[80] N. Brønsted. *Chem. Rev.*, 5:231, 1928. (Cited on pages 26, 44 and 52.)

[81] M. G. Evans and N. P. Polanyi. *Trans. Faraday Soc.*, 34:11, 1938. (Cited on pages 26, 44 and 52.)

[82] C. Stampfl, M. V. Ganduglia-Pirovano, K. Reuter, and M. Scheffler. *Surf. Sci.*, 500:386, 2002. (Cited on page 28.)

[83] K. Reuter and M. Scheffler. *Phys. Rev. B*, 65:035406, 2001. (Cited on pages 29, 30 and 31.)

[84] C. Stampfl. *Catal. Today*, 105:17, 2005. (Cited on page 29.)

[85] J. Rogal and K. Reuter, 2007. *Ab Initio* Atomistic Thermodynamics for Surfaces: A primer. In *Experiment, Modeling and Simulation of Gas Surface Interactions for REactive Flows in Hypersonic Flights* (pp. 2-1-2-18). Educational Notes RTO-EN-AVT-142, Paper 2. Neuilly-surSeine, France: RTO. Available from http://www.rto.nato.int/abstracts.asp. (Cited on pages 29 and 31.)

[86] H. Prophet and D. R. Stull. *JANAF Thermochemical Tables, 2nd Ed.* US National Bureau of Standards, Washington, DC, 1971. (Cited on pages 30, 31 and 32.)

[87] L. Imre and B. Bunsenges. *Phys. Chem.*, 74:220, 1970. (Cited on page 33.)

[88] G. Henkelman and H. Jonsson. *J. Chem. Phys.*, 113:9978, 2000. (Cited on pages 35, 36 and 63.)

[89] H. Jönsson, G. Mills, and K. W. Jacobsen. *Nudged Elastic Band Method for Finding Minimum Energy Paths of Transitions in Classical and Quantum Dynamics in Condensed Phase Simulations.* World Scientific, Singapor, 1998. (Cited on pages 35 and 36.)

[90] P. Giannozzi, S. Baroni, N. Bonini, M. Calandra, R. Car, C. Cavazzoni, D. Ceresoli, G. L. Chiarotti, M. Cococcioni, I. Dabo, and et al. *J. Phys.: Condens. Matter*, 21:395502, 2009. (Cited on pages 36, 116 and 121.)

[91] B. L. M. Hendriksen, S. C. Bobaru, and J. W. M. Frenkel. *Top. Catal.*, 36:43, 2005. (Cited on page 37.)

[92] J. Schnadt, A. Michaelides, J. Knudsen, R. T. Vang, K. Reuter, E. Lægsgaard, M. Scheffler, and F. Besenbacher. *Phys. Rev. Lett.*, volume 96. 2006. (Cited on page 37.)

[93] Paola Gavar. *Modeling the Catalyst Selectivity in the Ethylene Epoxidation Reaction: A First Principles Study.* PhD thesis, SISSA-International School for Advanced Studies, Trieste, Italy, 2007. (Cited on pages 38, 56, 64, 65, 66, 67, 72 and 73.)

[94] S. Linic and M. A. Barteau. *J. Am. Chem. Soc.*, 125:4034, 2003. (Cited on pages 41, 42, 47, 48, 51 and 52.)

[95] A. Kokalj, A. D. Corso, S. de Gironcoli, and S. Baroni. *Surf. Sci.*, 532:191, 2003. (Cited on page 41.)

[96] A. Kokalj, A. D. Corso, S. de Gironcoli, and S. Baroni. *J. Phys. Chem. B*, 106:9839, 2002. (Cited on pages 41 and 50.)

[97] D. Torres, N. Lopez, and F. Illas. *J. Catal.*, 243:404, 2006. (Cited on page 42.)

[98] A. J. Capote and R. J. Madix. *J. Am. Chem. Soc.*, 111:3570, 1989. (Cited on page 44.)

[99] D. A. Bulushev, E. A. Paukshtis, Y.N. Nogin, and B. S. Bal'zhinimaev. *Appl. Catal. A: Chem.*, 123:301, 1995. (Cited on page 44.)

[100] H. Idriss, J. P. Hindermann, R. Kieffer, A. Kiennemann, A. Vallet, C. Chauvin, J. C. Lavalley, and P. Chaumette. *J. Mol. Catal.*, 42:205, 1987. (Cited on page 44.)

[101] J. Kollar (6 Spencer Court, Wyckoff, NJ, 07481), *Process for the industrial production of ethylene oxide and aromatic acid* (1977), United States 4046782, URL http://www.freepatentsonline.com/4046782.html. (Cited on page 46.)

[102] S. Piccinin, N. L. Nguyen, C. Stampfl, and M. Scheffler. *J. Mater. Chem.*, 20:10521, 2010. (Cited on pages 46 and 52.)

[103] A. C. Luskaski and M. A. Barteau. *Catal. Lett.*, 128:9, 2009. (Cited on page 47.)

[104] P. Christopher and S. Linic. *ChemCatChem*, 2:78, 2010. (Cited on page 48.)

[105] Y. Sun and Y. Xia. *Science*, 298:2176, 2002. (Cited on page 48.)

[106] J. Chen, T. Herricks, and Y. Xia. *Angew. Chem.*, 117:2645, 2005. (Cited on page 48.)

[107] Y. Sun, B. Mayers T. Herricks, and Y. Xia. *Nano Lett.*, 3:955, 2003. (Cited on page 48.)

[108] P. Christopher and S. Linic. *J. Am. Chem. Soc.*, 130:11264, 2008. (Cited on page 48.)

[109] D. Torres, N. Lopez, F. Illas, and R. Lambert. *J. Am. Chem. Soc.*, 127:10774, 2005. (Cited on page 51.)

[110] M. L. Bocquet and D. Loffreda. *J. Am. Chem. Soc.*, 127:17207, 2005. (Cited on page 51.)

[111] T. Bligaard, J. K. Nørskov, S. Dahl, J. Matthiesen, C. Christensen, and J. Sehested. *J. Catal.*, 224:206, 2004. (Cited on page 52.)

[112] H. Falsig, B. Hvolbaek, I. S. Kristensen, T. Jiang, T. Bligaard, C. H. Christensen, and J. K. Nørskov. *Angew. Chem., Int. Ed.*, 47:4835, 2008. (Cited on page 52.)

[113] A. J. Nagy, G. Mestl, and R. Schlögl. *J. Catal.*, 188:58, 1999. (Cited on page 56.)

[114] Z. Qu, M. Cheng, W. Huang, and X. Bao. *J. Catal.*, 229:446, 2005. (Cited on page 56.)

[115] R. A. van Santen and H. P. C. Kuipers. *Adv. Catal.*, 35:265, 1987. (Cited on page 56.)

[116] R. B. Grant and R. M. Lambert. *J. Catal.*, 92:364, 1985. (Cited on page 56.)

[117] C. Backx, J. Moolhuysen, P. Geenen, and R. A. van Santen. *J. Catal.*, 72:364, 1981. (Cited on page 56.)

[118] R. A. Van Santen and C. P. M. de Groot. *J. Catal.*, 98:530, 1986. (Cited on page 56.)

[119] C. T. Campbell and M. T. Paffett. *Surf. Sci.*, 139:396, 1984. (Cited on page 56.)

[120] C. T. Campbell. *J. Catal.*, 94:436, 1985. (Cited on page 56.)

[121] M. Atkins, J. Couves, M. Hague, B. H. Sakakini, and K. C. Waugh. *J. Catal.*, 235:103, 2005. (Cited on page 56.)

[122] M. Dean, A. McKee, and M. Bowker. *Surf. Sci.*, 211:1061, 1989. (Cited on page 56.)

[123] A. W. Kleyn, D. A. Butler, and A. Raukema. *Surf. Sci.*, 363:29, 1996. (Cited on page 56.)

[124] X. Bao, M. Muhler, T. S. Niedrig, and R. Schlögl. *Phys. Rev. B*, 543:2249, 1996. (Cited on page 56.)

[125] L. Vitos, A. V. Ruban, H. L. Skriver, and J. Kollar. *Surf. Sci.*, 411:186, 1998. (Cited on page 59.)

[126] A. Y. Lozovoi, A. Alavi, and M. W. Finnis. *Phys. Rev. Lett.*, 85:610, 2000. (Cited on page 69.)

[127] K. Reuter, M. Verónica Ganduglia-Pirovano, C. Stampfl, and M. Scheffler. *Phys. Rev. B*, 65:165403, 2002. (Cited on page 69.)

[128] M. V. Ganduglia-Pirovano, K. Reuter, and M. Scheffler. *Phys. Rev. B*, 65:245426, 2002. (Cited on page 69.)

[129] A. Soon, M. Todorova, B. Delley, and C. Stampfl. *Phys. Rev. B*, 75:125420, 2007. (Cited on page 69.)

[130] J. Y. Kim, J. A. Rodriguez, J. C. Hanson, A. I. Frenkel, and P. Lee. *J. Am. Chem. Soc.*, 125:10684, 2003. (Cited on page 69.)

[131] Y. M. Niquet, M. Fuchs, and X. Gonze. *Phys. Rev. A*, 68:032507, 2003. (Cited on pages 75 and 78.)

[132] A. Heßelmann and G Jansen. *Chem. Phys. Lett.*, 367:778, 2003. (Cited on page 75.)

[133] O. A. Vydrov and T. van Voorhis. *J. Phys. Chem.*, 130:104105, 2009. (Cited on page 76.)

[134] O. A. Vydrov and T. van Voorhis. *Phys. Rev. Lett.*, 103:063004, 2009. (Cited on page 76.)

[135] A. D. Becke. *J. Chem. Phys.*, 98:5648, 1993. (Cited on page 76.)

[136] J. B. Krieger, Y. Li, and G. J. Iafrat. *Phys. Rev. A*, 45:101, 1992. (Cited on page 76.)

[137] D. Pine and P. Nozières. *The Theory of Quantum Liquid*, volume 1. Benjamin, New York, USA, 1966. (Cited on pages 76 and 80.)

[138] F. Furche. *Phys. Rev. B*, 64:195120, 2001. (Cited on pages 76 and 77.)

[139] M. Lein, E. K. U. Gross, and J. P. Perdew. *Phys. Rev. B*, 61:13431, 2000. (Cited on page 76.)

[140] J. F. Dobson and J. Wang. *Phys. Rev. Lett.*, 82:2123, 1999. (Cited on page 76.)

[141] J. M. Pitarke and A. G. Eguiluz. *Phys. Rev. B*, 57:6329, 1998. (Cited on page 76.)

[142] W. Kohn, Y. Meir, and D. E. Makarov. *Phys. Rev. Lett.*, 80:4153, 1998. (Cited on page 76.)

[143] M. Fuchs and X. Gonze. *Phys. Rev. B*, 65:235109, 2002. (Cited on pages 76, 77 and 101.)

[144] B. G. Janesko, T. M. Henderson, and G. E. Scuseria. *J. Chem. Phys.*, 130:081105, 2009. (Cited on page 76.)

[145] J. Toulouse, G. Jansen I. C. Gerber, A. Savin, and J. G. Ángyán. *Phys. Rev. Lett.*, 102:096404, 2009. (Cited on pages 76 and 77.)

[146] J. Harl and G. Kresse. *Phys. Rev. B*, 77:045136, 2008. (Cited on pages 76 and 77.)

[147] P. García-González A. Marini and A. Rubio. *Phys. Rev. Lett.*, 96:136404, 2006. (Cited on page 76.)

[148] J. Harl and G. Kresse. *Phys. Rev. Lett.*, 103:056401, 2009. (Cited on page 76.)

[149] F. Furche. *J. Chem. Phys.*, 122:164106, 2005. (Cited on page 77.)

[150] R. W. Godby, M. Schlüter, and L. J. Sham. *Phys. Rev. B*, 37:10159, 1988. (Cited on pages 78 and 93.)

[151] M. Hellgren and U. von Barth. *Phys. Rev. B*, 76:075107, 2007. (Cited on pages 78 and 93.)

[152] M. Hellgren and U. von Barth. *Phys. Rev. B*, 78:115107, 2008. (Cited on pages 78 and 93.)

[153] M. Hellgren and U. von Barth. *J. Chem. Phys.*, 131:044110, 2009. (Cited on pages 78 and 93.)

[154] H-V. Nguyen. *Efficient calculation of RPA correlation energy in the adiabatic connection fluctuation-dissipation theory.* PhD thesis, SISSA-International School for Advanced Studies, Trieste, Italy, 2008. (Cited on pages 82, 101 and 104.)

[155] H. Wilson, F. Gygi, and G. Galli. *Phys. Rev. B*, 78:113303, 2008. (Cited on page 82.)

[156] H. Wilson, D. Lu, F. Gygi, and G. Galli. *Phys. Rev. B*, 79:245106, 2009. (Cited on page 82.)

[157] R. Car, E. Tosatti, S. Baroni, and S. Leelaprute. *Phys. Rev. B*, 24:985, 1981. (Cited on page 83.)

[158] A. Baldereschi and E. Tosatti. *Phys. Rev. B*, 17:4710, 1978. (Cited on page 83.)

[159] A. Fleszar and R. Resta. *Phys. Rev. B*, 31:5305, 1985. (Cited on page 83.)

[160] H. van der Vorst. *SIAM J. Sci. Stat. Comput.*, 13:631, 1992. (Cited on page 86.)

[161] A. Debernardi. *Anharmonic Properties of Semiconductors from Density Functional Perturbation Theory.* PhD thesis, SISSA-International School for Advanced Studies, Trieste, Italy, 1995. (Cited on page 93.)

[162] W.H. Press, S.A. Teukolsky, W.T. Vetterling, and B.P. Flannery. *Numerical Recipes in FORTRAN; The Art of Scientific Computing.* Cambridge University, New York, NY, US, 2nd edition, 1993. (Cited on pages 95 and 96.)

[163] W. Yang and Q. Wu. *Phys. Rev. Lett.*, 89:143002, 2002. (Cited on page 96.)

[164] Q. Wu and W. Yang. *J. Theor. Comp. Chem.*, 2:626, 2003. (Cited on page 96.)

[165] T. H. Burgess, F. A. Bulat, and W. Yang. *Phys. Rev. Lett.*, 98:256401, 2007. (Cited on page 96.)

[166] A. Görling. *Phys. Rev. B*, 53:7024, 1996. (Cited on page 98.)

[167] M. Städele, M. Moukara, J. A. Majewski, P. Vogl, and A. Görling. *Phys. Rev. B*, 59:10031, 1999. (Cited on page 98.)

[168] A. Görling. *Phys. Rev. Lett.*, 83:5459, 1999. (Cited on page 98.)

[169] A. Görling, A. Heßalmann, M. Jones, and M. Levy. *J. Chem. Phys.*, 128:104104, 2008. (Cited on page 98.)

[170] A. Heßalmann, A. W. Götz, F. D. Salla, and A. Görling. *J. Chem. Phys.*, 127:054102, 2007. (Cited on page 98.)

[171] J. M. Merritt, V. E. Bondybey, and M. C. Heaven. *Science*, 324:1548, 2009. (Cited on pages 101, 102, 104 and 108.)

[172] I. Røeggen and L. Veseth. *Int. J. Quantum. Chem*, 101:201, 2005. (Cited on pages 101 and 108.)

[173] V. F. Lotrich, R. J. Bartlett, and I. Grabowskib. *Chem. Phys. Lett.*, 405:43, 2005. (Cited on page 101.)

[174] M. Casula, C. Filippi, and S. Sorella. *Phys. Rev. Lett.*, 95:100201, 2005. (Cited on pages 101 and 108.)

[175] S. Ivanov and M. Levy. *J. Chem. Phys.*, 119:7087, 2003. (Cited on pages 104 and 117.)

[176] D. D. Johnson. *Phys. Rev. B*, 38:12807, 1988. (Cited on page 108.)

[177] G. Kresse and J. Furthmüller. *Phys. Rev. B*, 54:11169, 1996. (Cited on page 108.)

[178] C. G. Van de Walle. *Phys. Rev. Lett.*, 80:2177, 1998. (Cited on pages 112 and 115.)

[179] N. E. Dahlen, R. van Leeuwen, and U. von Barth. *Phys. Rev. A*, 73:012511, 2006. (Cited on page 113.)

[180] Y. C. Chang, D. H. Harding, W. C. Stwalley, and C. R. Vidal. *J. Chem. Phys.*, 85:2436, 1986. (Cited on pages 114 and 115.)

[181] P. F. Bernath, A. Shayesteh, K. Tereszchuk, and R. Colin. *Science*, 297:1323, 2002. (Cited on pages 114 and 115.)

[182] R. P. Hostenyt and S. A. Hagstrom. *J. Chem. Phys.*, 58:4396, 1973. (Cited on pages 114 and 115.)

[183] A. Balakrishnan, V. Smith, and B. P. Stoicheff. *Phys. Rev. Lett.*, 68:2149, 1992. (Cited on page 115.)

[184] H. J. Monkhorst and J. D. Pack. *Phys. Rev. B*, 13:5188, 1976. (Cited on page 121.)

[185] N. Marzari, D. Vanderbilt, A. D. Vita, and M. C. Payne. *Phys. Rev. Lett.*, 82:3296, 1999. (Cited on page 121.)

[186] G. Henkelman, B. P. Uberuaga, and H. Johnson. *J. Chem. Phys.*, 113:9901, 2000. (Cited on page 121.)

Acknowledgements

I am heartily thankful to my supervisors, Prof. Stefano de Gironcoli and Dr. Simone Piccinin, who encourage, guide and support from the initial to the final level in understanding the subjects in this Thesis.

I would like to thank Dr. Huy-Viet Nguyen, Prof. Andrea Da Coso, Prof. Paolo Giannozzi, and Prof. Giulia Galli for useful discussions and their helps in developing the Quantum ESPRESSO package.

Special thanks go to my friends: Alan Bizjak, Emine Kucukbenli, Manh-Thuong Nguyen, Nicola Colonna, Sara Fortuna, and Simon Binnie who read and help me to correct the English mistakes in this Thesis.

I also thank to my friends at SISSA: Riccardo, Mauro, Pier Paolo, Hongyi, Zhaleh, Fahimeh, Changru, Xian,... for many interesting discussions, as well as life enjoying during my PhD time. Specially, thanks to all my Vietnamese friends in Trieste for having turned this little city into my home for the last four years.

Personally, I wish to thank my family for their support and understanding.